arXiv:1608.04469v1 [astro-ph.GA] 16 Aug 2016

August 17, 2016

Numerical Simulations of Turbulent, Molecular Clouds Regulated by Radiation Feedback Forces I: Star Formation Rate and Efficiency

Sudhir Raskutti, Eve C. Ostriker, and M. Aaron Skinner

Department of Astrophysical Sciences, Princeton University, Princeton, NJ 08544, USA

raskutti@astro.princeton.edu, eco@astro.princeton.edu, askinner@astro.princeton.edu

ABSTRACT

Radiation feedback from stellar clusters is expected to play a key role in setting the rate and efficiency of star formation in giant molecular clouds (GMCs). To investigate how radiation forces influence realistic turbulent systems, we have conducted a series of numerical simulations employing the *Hyperion* radiation hydrodynamics solver, considering the regime that is optically thick to ultraviolet (UV) and optically thin to infrared (IR) radiation. Our model clouds cover initial surface densities between $\Sigma_{\rm cl,0} \sim 10 - 300\ M_\odot\ {\rm pc}^{-2}$, with varying initial turbulence. We follow them through turbulent, self-gravitating collapse, formation of star clusters, and cloud dispersal by stellar radiation. All our models display a lognormal distribution of gas surface density Σ; for an initial virial parameter $\alpha_{\rm vir,0} = 2$, the lognormal standard deviation is $\sigma_{\ln\Sigma} = 1 - 1.5$ and the star formation rate coefficient $\varepsilon_{{\rm ff},\bar{\rho}} = 0.3 - 0.5$, both of which are sensitive to turbulence but not radiation feedback. The net star formation efficiency $\varepsilon_{\rm final}$ increases with $\Sigma_{\rm cl,0}$ and decreases with $\alpha_{\rm vir,0}$. We interpret these results via a simple conceptual framework, whereby steady star formation increases the radiation force, such that local gas patches at successively higher Σ become unbound. Based on this formalism (with fixed $\sigma_{\ln\Sigma}$), we provide an analytic upper bound on $\varepsilon_{\rm final}$, which is in good agreement with our numerical results. The final star formation efficiency depends on the distribution of Eddington ratios in the cloud and is strongly increased by turbulent compression of gas.

Subject headings: hydrodynamics - methods: numerical - radiative transfer - ISM: clouds - stars: formation

1. Introduction

Gravitational collapse within Giant Molecular Clouds (GMCs) leads to star formation, and the radiation force produced by young, hot stars can be dynamically important in regulating this

process. Radiation forces may contribute to driving turbulence within clouds, and if strong enough, can halt global collapse and lead to the overall dispersal of a star forming cloud (O'Dell et al. 1967; Elmegreen 1983; Scoville et al. 2001; Krumholz & Matzner 2009; Fall et al. 2010; Murray et al. 2010; Krumholz & Dekel 2010; Sales et al. 2014; Kim et al. 2016). If radiation forces dominate over other forms of feedback, they may be responsible for setting both the mean star formation rate (SFR) and the net star formation efficiency (SFE) over a cloud's lifetime.

Indications of some form of feedback regulating star formation can be found in direct observations of star-forming Milky Way Clouds, which have low observed SFEs $M_*/M_{\rm gas} \sim 0.002 - 0.20$ (Cohen & Kuhi 1979; Myers et al. 1986; Mooney & Solomon 1988; Williams & McKee 1997; Carpenter 2000; Evans et al. 2009; Lada et al. 2010; Murray 2011; Kennicutt & Evans 2012; García et al. 2014), and clear signatures of disruption by massive stars for clouds at the higher end of the SFE distribution. Assessing the net SFE over the lifetime of a cloud ($\varepsilon_{\rm final} \equiv M_{*,\rm final}/M_{\rm gas,init}$) is observationally challenging, since up to the time of its dissolution, the cloud's stellar population is secularly increasing, while at late stages the observed total mass has dropped below the initial value through gas mass loss. However, observing the instantaneous SFE across a population of clouds still provides constraints, assuming a fair sample across different stages of the cloud lifecycle. If, for example, the SFR is steady and dispersal of gas takes place rapidly compared to the lifetime of a cloud, then the observed instantaneous SFE would uniformly cover the range between zero and $\varepsilon_{\rm final}$, so that the average observed SFE would be roughly half of $\varepsilon_{\rm final}$.

Additional indirect evidence that is cited to explain low SFEs by feedback in GMCs comes from the long molecular depletion times ($t_{\rm dep} \equiv M_{\rm mol}/\dot{M}_* \sim$ Gyr for gas traced by CO) observed in extragalactic studies (Bigiel et al. 2008; Schruba et al. 2011; Saintonge et al. 2011; Rahman et al. 2012; Leroy et al. 2013; Genzel et al. 2015). If molecular gas is concentrated in GMC-like structures with lifetimes of a few tens of Myrs (Leisawitz et al. 1989; Mizuno et al. 2001; Kawamura et al. 2009), then a low lifetime SFE ~ 0.01 would be implied by $t_{\rm dep} \sim$ Gyr, potentially demanding strong feedback. Alternatively, if molecular clouds have long lifetimes, radiation forces and other feedback effects could in principle keep $t_{\rm dep}$ long compared to the gas freefall time $t_{\rm ff}$ (see Zuckerman & Palmer 1974; Krumholz & Tan 2007; Krumholz et al. 2012) if they were able to sustain high turbulence levels without destroying the cloud (Krumholz & McKee 2005; Padoan & Nordlund 2011; Padoan et al. 2012; Federrath & Klessen 2012). Thus, it has been argued that the inefficiency in both GMC SFEs and SFRs can be accounted for by massive stars supporting and then destroying their host GMCs (see reviews of McKee & Ostriker 2007; Padoan et al. 2014; Krumholz 2014).

Although galactic-scale molecular depletion times are often invoked to constrain GMC-scale star formation processes, a complication is that extragalactic observations beyond the Local Group generally do not resolve individual clouds. When using a beam corresponding to kpc or larger scales and integrating CO emission, molecular gas in bound GMCs is not easily distinguished from more diffuse molecular gas. Since the feedback mechanisms that control the dynamics and evolution of diffuse gas (molecular and/or atomic) may be quite different from those that control dynamics and SFEs of bound GMCs, this caveat must be kept in mind. Indeed, well-studied star-forming clouds

in the Gould Belt appear to have molecular $t_{\rm dep}$ much lower – perhaps by an order of magnitude – than values indicated by kpc-scale extragalactic studies (Kennicutt & Evans 2012). This may mean that much of the molecular gas in extragalactic studies is diffuse (and non-star-forming), rather than in bound, star-forming GMCs. Nevertheless, even in local clouds with shorter molecular $t_{\rm dep}$, the corresponding observed SFE is still < 0.1 (Lada et al. 2010).

A number of forms of massive-star feedback have been proposed as dynamical drivers in the interstellar medium (ISM). The dominant feedback mechanism for driving kinetic energy in the ISM as a whole is likely Type II supernovae (SNe) (Mac Low & Klessen 2004; Elmegreen & Scalo 2004). One useful way to characterize star formation feedback is in terms of the momentum injection per total mass in stars formed (averaged over the IMF), and this is likely to be an order of magnitude larger for SNe than for other forms of feedback such as radiation (Ostriker & Shetty 2011; see also Kim & Ostriker 2015; Iffrig & Hennebelle 2015; Walch & Naab 2014; Martizzi et al. 2015 for assessments of momentum injection by SNe). However, the delay of SNe by $3 - 30$ Myr means that depending on how long GMCs survive, this momentum may primarily be deposited in the diffuse (atomic or molecular) ISM rather than in bound, star forming clouds (Matzner 2002; Fall et al. 2010). Furthermore, blast waves from (early) supernovae that explode within GMCs preferentially eject lower-density gas, and may leave higher-density structures behind. Thus, even if other forms of feedback are less intrinsically powerful than SNe, they may be more important to GMC evolution.

Forms of feedback associated with earlier stages of stellar evolution include winds from massive stars, ionizing and non-ionizing radiation, and outflows and jets from low mass protostars. Some of these have been proposed as candidates for driving the dynamics of whole GMCs, while others are expected to have only weak or localized effects (see, e.g., review of Padoan et al. 2014). Protostellar jets and outflows are most important in clouds or cluster-forming clumps that do not contain massive stars (Quillen et al. 2005; Cunningham et al. 2006; Li & Nakamura 2006; Nakamura & Li 2008; Wang et al. 2010; Hansen et al. 2012). Although shocked winds from massive stars were initially expected to be important to cloud evolution (Castor et al. 1975; Weaver et al. 1977), the inhomogeneous structure of turbulent clouds implies that much of the wind energy can escape (Rogers & Pittard 2013). This may explain the low X-ray luminosity of observed systems such as the Carina nebula (Harper-Clark & Murray 2009).

Much of the current work on early feedback instead concentrates on the dynamics of expanding HII regions, as driven by both the warm ionized gas (Whitworth 1979; McKee et al. 1984; Matzner 2002; Krumholz et al. 2006; Dale et al. 2005, 2012, 2013; Vázquez-Semadeni et al. 2010; Colín et al. 2013; Walch et al. 2012), and by radiation – either direct (Krumholz & Matzner 2009; Fall et al. 2010; Murray et al. 2010; Sales et al. 2014) or reprocessed by dust (Murray et al. 2010; Skinner & Ostriker 2015). Reprocessed radiation is expected to increase in importance relative to direct radiation in high surface density clouds that are optically thick to infrared (IR). Overall, radiation forces are expected to exceed those from ionized gas pressure only in more massive, higher surface density clouds (Fall et al. 2010; Kim et al. 2016), and there is some observational support for this (Lopez et al. 2011, 2014; Pellegrini et al. 2007, 2010). Numerical simulations by Dale et al.

(2012, 2013) show that pressure from photoionized gas is capable of disrupting clouds and expelling substantial gas only when the escape speed is low compared to the ionized gas sound speed. Walch et al. (2012) found consistent results for the effects of photoionized gas in their simulations of clouds with varying fractal dimension in the initial density structure.

While analytic and spherically symmetric numerical models predict that radiation feedback effects will become dominant in clouds with high mass and surface density, it is clearly necessary to understand the effects of strongly inhomogeneous density structure, which is the hallmark of turbulent GMCs. Krumholz & Thompson (2012) and Davis et al. (2014) found for turbulent disks that radiation and gas tend to be anticorrelated, which reduces the net force of radiation. A recent analysis by Thompson & Krumholz (2016) suggests that incorporating the full lognormal density distribution imposed by turbulence is crucial to understanding how radiative feedback can drive outflows and limit star formation.

Realistic investigation of radiation effects in suppressing star formation in turbulent, inhomogeneous clouds requires full time-dependent radiation hydrodynamics (RHD) modeling with self-gravity. Recently, Skinner & Ostriker (2015) applied the *Hyperion* RHD code (Skinner & Ostriker 2013) to study the evolution of massive clouds that are optically thick to reprocessed radiation. This work showed that reprocessed radiation only expels significant mass from a turbulent, initially gravitationally-bound cloud when the Eddington ratio at IR $f_{\rm Edd,*} \equiv \kappa_{\rm IR}\Psi/(4\pi Gc)$ exceeds unity, where $\kappa_{\rm IR}$ is the mean IR opacity and Ψ the mean light-to-mass ratio of stars. Even at $f_{\rm Edd,*} \sim 1-3$, however, the SFE is high, with $\sim 50\%$ or more of the original GMC collapsing and accreting on to star particles. Furthermore, the turbulent structure of the gas significantly reduces radiation forces, due to a matter-radiation anti-correlation.

Here, we apply the *Hyperion* code to consider the opposite limit of clouds with lower surface density, in which direct UV dominates over reprocessed radiation. We consider model GMCs with a wide range of sizes, masses, and initial virial parameters. Our chief aim is to understand how self-gravitating, turbulent clouds react dynamically to radiation that emerges from their densest (collapsed) regions. In particular, we wish to quantify any radiation effects on reducing the SFR and/or SFE by limiting local collapse and disrupting clouds.

In the present work, we consider solely the effects of UV radiation forces on cloud dynamics, a question that has not previously been addressed in fully three-dimensional models. For clouds at the lower range of surface density that we model, pressure forces from photoionized gas (which we do not treat here) may in real systems be comparable to direct radiation forces (Krumholz & Matzner 2009; Fall et al. 2010; Lopez et al. 2011; Kim et al. 2016). A more realistic treatment, including the effects of ionization and heating from radiation in addition to radiation forces, is necessary for quantifying the relative importance of these processes but will be deferred to future work. The present study is intended to provide a baseline for future more comprehensive simulations by quantifying how radiation forces (in the single-scattering approximation) by themselves affect the evolution of turbulent, self-gravitating clouds.

We begin in Section 2 by describing the *Hyperion* code and the numerical setup of our turbulent clouds. In Section 3 we present an overview of evolution for a fiducial model, as well as convergence tests. In Section 4 we show our results for SFE and SFR across the full suite of model clouds, and further analyze the effects of the lognormal density distribution on the radiation/gas interaction. We summarize and discuss our conclusions in context of other theoretical work and observations in Section 5. Appendix A presents additional code tests for idealized problems over a range of parameters in the single-scattering regime.

2. Numerical Setup

2.1. Equations and Algorithms

We run three-dimensional radiation hydrodynamic (RHD) simulations on a Cartesian grid using the *Hyperion* (Skinner & Ostriker 2013) extension of the *Athena* code (Stone et al. 2008). For this application, we solve the following simplified mixed-frame equations of RHD:

$$\partial_t \rho + \nabla \cdot (\rho \mathbf{v}) = 0, \tag{1}$$

$$\partial_t (\rho \mathbf{v}) + \nabla \cdot (\rho \mathbf{v}\mathbf{v} + P\mathbb{I}) = -\rho \nabla \Phi + \rho \kappa \frac{\mathbf{F}}{c}, \tag{2}$$

$$\frac{1}{\hat{c}} \partial_t \mathcal{E} + \nabla \cdot \left(\frac{\mathbf{F}}{c} \right) = -\rho \kappa \mathcal{E} + \mathbb{S}, \tag{3}$$

$$\frac{1}{\hat{c}} \partial_t \left(\frac{\mathbf{F}}{c} \right) + \nabla \cdot \mathbb{P} = -\rho \kappa \frac{\mathbf{F}}{c}, \tag{4}$$

where ρ, $\mathbf{v}$, and P are the gas density, velocity, and pressure, and Φ is the gravitational potential, all evaluated in the lab frame. We adopt the simplifying assumption of an isothermal equation of state for the gas with $P = c_s^2 \rho$ (see discussion below). The variables $\mathcal{E}$, $\mathbf{F}$, and $\mathbb{P}$ are the radiation energy density, flux vector, and pressure tensor, respectively, again evaluated in the lab frame, while κ is the frequency-weighted specific material opacity calculated in the gas rest frame.

Hyperion closes the two radiative moment equations above by adopting the M_1 relation (Levermore 1984). This expresses the pressure tensor in terms of $\mathcal{E}$ and $\mathbf{F}$, with $\mathbb{P} \rightarrow (1/3)\mathcal{E}\mathbb{I}$ in the diffusion limit ($|\mathbf{F}|/\mathcal{E}c \ll 1$) and $\mathbb{P} \rightarrow \mathcal{E}\hat{\mathbf{n}}\hat{\mathbf{n}}$ in the streaming limit ($|\mathbf{F}|/\mathcal{E}c \rightarrow 1$), where $\hat{\mathbf{n}} = \mathbf{F}/|\mathbf{F}|$. We omit radiative emission terms from gas and dust in Equation (3), as we are interested in the limit in which the effects from direct stellar radiation dominate over IR emission from the dust. This stellar emission is captured in the term $\mathbb{S}$ in Equation (3), which describes radiative emission from star particles (see below). Finally, $\hat{c} \neq c$ is a reduced radiation propagation speed, adopted within the Reduced Speed of Light Approximation (RSLA) (Gnedin & Abel 2001) to ensure that timesteps updating the radiation field are not unfeasibly short.

Hyperion divides Equations (1)-(4) into gas and radiation subsystems because these variables are transported on very different time scales. We therefore separate the two systems and solve for

the gas subsystem using *Athena*'s unsplit Van Leer (VL) integrator (Stone & Gardiner 2009), a Godunov finite-volume method adapted from the MUSCL-Hancock scheme of Falle (1991). The hydrodynamic timestep is determined using a radiation-modified CFL condition with Courant number of 0.4 (the typical value adopted in VL integration schemes) and a radiation-modified effective sound speed that accounts for the effect of interactions between the gas and radiation fields, $c_{\rm eff} \equiv \sqrt{(\gamma P + 4/9\mathcal{E}(1 - {\rm e}^{-\rho\kappa_0\Delta x}))/\rho}$ (Krumholz et al. 2007).

Hyperion solves the radiation subsystem using an operator-split method that separates the radiation source terms into explicit and implicit terms, with the explicit terms updated together with the update from the divergence of $\mathbf{F}$ and $\mathbb{P}$. Here, both the radiation energy and the flux absorption updates are solved using a standard θ-scheme update with $\theta = 0.51$, very close to second order implicit in time.

The radiation subsytem is similarly solved using a VL scheme, with a Harten-Lax-van Leer (HLL) Riemann solver (González et al. 2007) used to calculate the flux between cells. In this case, the timestep is set by a CFL condition with the radiation signal speed $\hat{c}$. This reduced speed of light is chosen so that radiation timesteps are as long as possible, while still ensuring that the RSLA does not improperly affect the gas dynamics. We may achieve this so long as $\hat{c}$ is sufficiently large that the radiation field approaches equilibrium much faster than characteristic gas time scales. For streaming radiation, a practical condition is $\hat{c} \sim 10 v_{\rm max} \gg v_{\rm max}$ (see Skinner & Ostriker 2013). There are then roughly 10 radiation substeps for each update to the gas subsystem.

In order to avoid unrealistically short timesteps for low density regions accelerated by a strong radiative flux, there is an artificially imposed density floor. Cells whose density falls below a prescribed value at any given timestep are reset to the density floor with zero momentum. This may add mass to the grid over the course of a simulation, but in practice the density floor is chosen such that less than $\sim 0.1\%$ of the initial cloud mass is artificially added over the course of a simulation.

Stars are represented within the code by point-mass sink particles (Gong & Ostriker 2013). Sink particles are formed dynamically when cells exceed a density threshold $\rho_{\rm th} = 8.86\, c_s^2/(\pi G \Delta x^2)$ motivated by the Larson (1969) and Penston (1969) solutions for self-gravitating isothermal collapse. Locations where sink particles form must also be potential minima (Banerjee et al. 2009; Federrath et al. 2010; Vázquez-Semadeni et al. 2011). If a cell satisfies these criteria, a sink particle is created at the center of a control volume of width $3\Delta x$. The sink particle has initial mass and momentum set by the sum over all control volume cells. Subsequently, gas is accreted onto the sink particles based on the HLL flux at the interface between sink control volumes and the rest of the grid. Gas variables within the control volume are set by extrapolating values from the surrounding active zones in the grid.

Sink particles are evolved in time using a leapfrog kick-drift-kick method (Springel 2005), where the particles' positions and momenta are updated alternately. The position is updated using the current velocities, while the momentum is updated based on gravitational potential differences.

The potential itself is computed using particle-mesh methods with a Triangular Shaped Cloud (TSC) kernel applied to map each particle's mass onto the grid (Hockney & Eastwood 1981). The combined particle + gas potential is found using a Fourier transform method on a domain equal to eight times the computational volume in order to implement vacuum boundary conditions for Φ (Hockney & Eastwood 1981). Finally, when the control volumes of two sink particles overlap, they are merged and placed at the center of mass of the two old particles.

Monochromatic radiation from the sink particles is emitted isotropically, representing idealized luminous stellar clusters. The source function $\mathbb{S} = j_*/c$ of each particle of mass M_* takes a Gaussian shape with

$$j_*(r) = \frac{L_*}{(2\pi\sigma_*^2)^{3/2}} \exp\left(-\frac{r^2}{2\sigma_*^2}\right), \tag{5}$$

with (fixed) radius $r_* = \sqrt{2\log 2}\sigma_* = 1$ pc and fixed luminosity per unit mass $\Psi \equiv L_*/M_*$ typical of young, luminous clusters. We adopt a fiducial value of $\Psi = 2000$ erg s^{-1} g^{-1}, characteristic of a fully sampled Kroupa IMF (Dopita et al. 2006).

We note that undersampling of the IMF can lead to both a large stochastic variation (da Silva et al. 2012) and a systematic overestimate in the luminosity per unit mass (Weidner & Kroupa 2006). However, as we discuss in Section 3.2, all of our clouds are close to fully sampled by the time star formation is complete. We further discuss the effects of varying Ψ in Section 4.4.

2.2. Initial Conditions

We consider the evolution of self-gravitating star-forming clouds over a period of ~ 4 initial freefall times. Each cloud is initialized as a uniform density sphere, with $\rho_0 = 3M_{\rm cl,0}/(4\pi r_0^3)$, where r_0 is the initial cloud radius. The clouds are centered inside cubic simulation volumes of length $L = 4r_0$ with outflow boundary conditions, so that we may track the mass expelled from the cloud by radiation forces. The gas surrounding the cloud is initialized at a factor of 10^3 lower than the cloud density, so that the total mass surrounding the cloud is $\sim 0.015\ M_{\rm cl,0}$. The density floor is

Table 1. Fiducial Parameters

Parameter	Value
$\alpha_{\rm vir,0}$	2.0
r_0	15 pc
$M_{\rm cl,0}$	$5 \times 10^4\ M_\odot$
$\Sigma_{\rm cl,0}$	70.74 $M_\odot$ pc^{-2}
$t_{\rm ff,0}$	4.29 Myr
$v_{\rm RMS}$	4.16 km s^{-1}
$v_{\rm esc}$	5.36 km s^{-1}
c_s	0.2 km s^{-1}
$\hat{c}$	250 km s^{-1}
Ψ	2000 erg s^{-1} g^{-1}
κ	1000 cm^2 g^{-1}

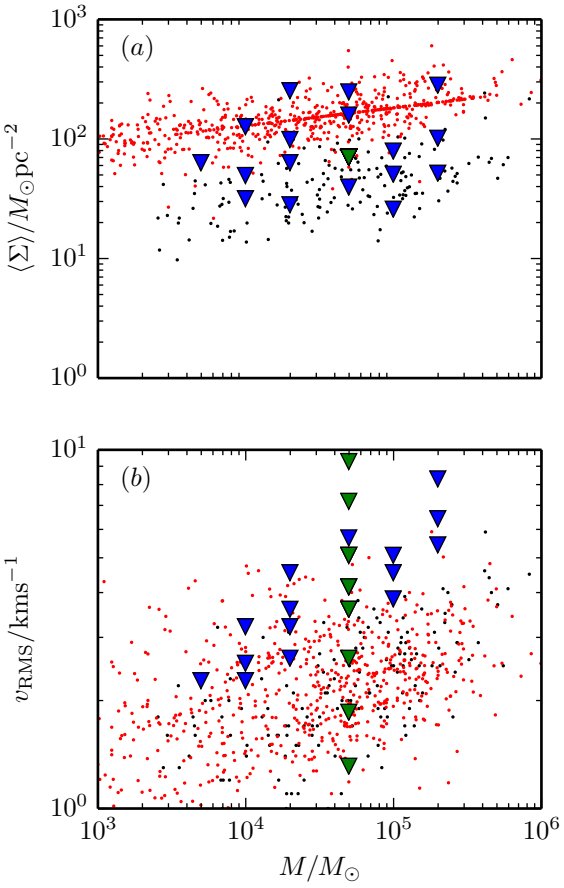

Fig. 1.— Parameter space of (a) cloud mass vs surface density, and (b) cloud mass vs velocity dispersion for our Σ-series (blue triangles) and α-series (green triangles) models. For comparison, we also show corresponding values for Galactic GMCs observed by Heyer et al. (2009) (black) and Roman-Duval et al. (2010a) (red).

lower than this again by a factor of 10, so that only a small amount of mass is added to the cloud over the course of a simulation run.

In order to cover a realistic range in cloud surface density, we adopt a range above and below fiducial values $M_{\rm cl,0} = 5 \times 10^4$ and $r_0 = 15$ pc, which corresponds to a cloud surface density of $\Sigma_{\rm cl,0} \equiv M_{\rm cl,0}/(\pi r_0^2) = 70.7\ M_\odot\ {\rm pc}^{-2}$. Our Σ-series consists of a subset of models with initial cloud masses $M_{\rm cl,0} = 5 \times 10^3, 10^4, 2 \times 10^4, 5 \times 10^4, 10^5, 2 \times 10^5\ M_\odot$ and radii $r_0 = 5, 8, 10, 15, 20, 25, 35$ pc. In Figure 1 we show the masses, surface densities and velocity dispersions of the full set of Σ-series models compared to the same quantities derived for a set of 158 Milky Way GMCs measured by Heyer et al. (2009) and a more extended sample of 580 molecular clouds measured in Roman-Duval et al. (2010a). Similar to Dale et al. (2012), we cover the high-mass end of the observed distribution, with our fiducial model being roughly characteristic of the median observed cloud.

The gas motions in our clouds are initially seeded by a turbulent velocity field, with power spectrum $v^2(k) \propto k^{-4}$ as is observed within GMCs (e.g., Dobbs et al. 2013). The turbulence is initialized as described in Stone et al. (1998); Skinner & Ostriker (2015). Briefly, we generate a Gaussian random field in Fourier space, such that over the range $k \in [2, 64] \times dk$ where $dk = 2\pi/L$, δv_k is chosen from a Gaussian distribution with variance $P(k) \propto k^{-4}$. This field is then transformed back to real space and renormalized in terms of the virial parameter $\alpha_{\rm vir,0} \equiv 2E_K/|E_G|$ so that the variance of the velocity distribution obeys $\sigma^2 = 2E_K/M_{\rm cl,0} = \alpha_{\rm vir,0}E_G/M_{\rm cl,0}$, where $E_K = M_{\rm cl,0}v_{\rm RMS}^2/2$ is the total initial turbulent gas kinetic energy, and $E_G = -3GM_{\rm cl,0}^2/(5r_0)$ is the cloud's initial gravitational binding energy. Finally, the momentum field is forced to have zero mean by subtracting off the initial net momentum of the cloud. The initial turbulent power spectrum is a mixture of solenoidal and compressive modes. We further discuss effects of the specific initialization of turbulence in Sections 4.2.3 and 4.5. For the fiducial model, and other models in the $\Sigma-$series, we set $\alpha_{\rm vir,0} = 2$. We also consider another series of models, the α-series, in which the initial $\alpha_{\rm vir,0}$ is in the range 0.1 to 10.0.

Clouds with $\alpha_{\rm vir} = 2$ are still marginally bound so long as the thermal energy does not contribute significantly to the total kinetic energy i.e., $c_s^2 \ll 3GM_{\rm cl,0}/(5r_0)$. In practice, for the lowest surface density clouds that we consider, this is satisfied provided $c_s \ll 1$ km s^{-1}. We adopt a constant isothermal sound speed $c_s = 0.2$ km s^{-1} for all simulations, consistent with a temperature of $T \sim 10$ K, as is characteristic of most of the mass in observed GMCs (Scoville et al. 1987). Of course, ionizing UV radiation will heat a very small fraction of the gas to a much higher temperature, and non-ionizing radiation can raise the temperature of gas within regions near stellar sources (within $A_V \sim 1$ where it is absorbed). However, given the high (FUV) optical depths of clouds, most of the gas is shielded from both internal and external radiation sources. For the regime of the present study, the optical depth to IR is small, so radiation that is absorbed and reprocessed to IR near sources subsequently escapes from the cloud without significant re-absorption by dust. To the extent that regions near sources can be heated above ~ 10K, the increase in pressure would limit fragmentation, with important consequences for the IMF (Krumholz et al. 2007; Myers et al. 2014). In addition, gas that is heated above the escape speed of the cloud could directly evaporate.

In Table 1, we list simulation inputs for our fiducial model, including the initial cloud mass, radius, and virial parameter, and the parameters $c_s, \hat{c}, \Psi$ and κ. Our standard resolution is 256^3, although we have employed higher and lower resolution grids to test convergence. We also adopt a fixed opacity $\kappa = 1000$ cm^2 g^{-1}, consistent with the radiation pressure cross sections per H derived from the Weingartner & Draine (2001) dust model (Draine 2011).

We extend this in Table 2, to show $M_{\rm cl,0}$, r_0, and $\alpha_{\rm vir,0}$ for all models in our Σ and α-series. For each simulation, we show also the initial surface density $\Sigma_{\rm cl,0} \equiv M_{\rm cl,0}/(\pi r_0^2)$, the initial RMS velocity dispersion $v_{\rm RMS} = [3\alpha_{\rm vir,0} G M_{\rm cl,0}/(5r_0)]^{1/2}$, the escape speed at the edge of the cloud $v_{\rm esc} = (2GM_{\rm cl,0}/r_0)^{1/2}$, the initial gravitational free-fall time $t_{\rm ff,0} = [3\pi/(32G\rho_0)]^{1/2}$ and the initial hydrogen number density $n_0 = \rho_0/(1.4m_p)$, where $\rho_0 = 3M_{\rm cl,0}/(4\pi r_0^3)$ is the initial gas density and we allow for 40% helium by mass. Model Σ-M5E4-R15 (the same as α-A2.0), shown in bold, is the fiducial model.

3. Tests of the Fiducial Model

3.1. Overview of Time Evolution

We begin by considering the overall time evolution of our fiducial model. In Figures 2 and 3 we show evolving column density maps of this cloud in the y-z and x-y planes respectively. We see that turbulence drives the cloud into collapse very rapidly, and that by a little before half a free-fall time, mass has gathered preferentially along two perpendicular filaments, roughly coincident with the x and z-axes. The first star-formation event occurs around this time, as the density peaks in the cloud continue to collapse under self-gravity. The filamentary structure of gas in the cloud and the shape of its density distribution do not however change significantly. By $\sim t_{10}$, where t_x denotes the time at which x % of the stellar mass is assembled, the main difference from earlier is that the density contrast between the filaments and surrounding gas has increased. As star formation progresses, the UV radiation begins to drive gas in even the densest filaments away from the sites of star formation. By the time half the stars have formed, much of the gas, even at higher densities, is already flowing outwards from the center of mass. At late stages, shown for example in the surface density projections at $t = 2\ t_{\rm ff,0}$ in Figure 4, all of the material is streaming away from the center, which has been cleared of gas.

Figure 5 shows the same picture as in Figure 3 but for a single slice through the x-y plane with the evolving radiation field flux directions and energy density overplotted in vectors and contours respectively. Because of the filamentary nature of the cloud, even though stars form near the center of the original GMC, the radiation from these stars very quickly blows a hole in the surrounding gas. Therefore, by t_{10}, as shown in the second snapshot, a significant fraction of the radiation already escapes the cloud through the second quadrant, where the gas density is small.

In detail, the gas structure surrounding the most massive star clusters is far from smooth and

Table 2. Model Parameters

Model	$\Sigma_{\rm cl,0}$ $[M_\odot\ {\rm pc}^{-2}]$	$M_{\rm cl,0}$ $[M_\odot]$	r_0 [pc]	$n_{\rm H,0}$ $[{\rm cm}^{-3}]$	$t_{\rm ff,0}$ [Myr]	$v_{\rm RMS}$ $[{\rm km\ s}^{-1}]$	$v_{\rm esc}$ $[{\rm km\ s}^{-1}]$	$\alpha_{\rm vir,0}$
Σ-M2E4-R25	10.19	2×10^4	25	8.860	14.6	2.04	2.63	2.0
Σ-M5E4-R35	12.99	5×10^4	35	8.072	15.3	2.72	3.51	2.0
Σ-M2E4-R20	15.92	2×10^4	20	17.30	10.5	2.28	2.94	2.0
Σ-M5E4-R25	25.46	5×10^4	25	22.15	9.24	3.22	4.16	2.0
Σ-M1E5-R35	25.98	1×10^5	35	16.14	10.8	3.85	4.97	2.0
Σ-M2E4-R15	28.29	2×10^4	15	41.02	6.79	2.63	3.39	2.0
Σ-M1E4-R10	31.83	1×10^4	10	69.22	5.23	2.28	2.94	2.0
Σ-M5E4-R20	39.79	5×10^4	20	43.26	6.61	3.60	4.65	2.0
Σ-M1E4-R08	49.74	1×10^4	8	135.2	3.74	2.54	3.29	2.0
Σ-M1E5-R25	50.93	1×10^5	25	44.30	6.53	4.55	5.88	2.0
Σ-M2E5-R35	51.97	2×10^5	35	32.29	7.65	5.44	7.02	2.0
Σ-M5E3-R05	63.66	5×10^3	5	276.9	2.61	2.28	2.94	2.0
Σ-M2E4-R10	63.66	2×10^4	10	138.4	3.70	3.22	4.16	2.0
Σ-M5E4-R15	**70.74**	$\mathbf{5 \times 10^4}$	**15**	**102.5**	**4.29**	**4.16**	**5.36**	**2.0**
Σ-M1E5-R20	79.58	1×10^5	20	86.52	4.67	5.09	6.57	2.0
Σ-M2E4-R08	99.47	2×10^4	8	270.4	2.64	3.60	4.65	2.0
Σ-M2E5-R25	101.9	2×10^5	25	88.60	4.62	6.44	8.31	2.0
Σ-M1E4-R05	127.3	1×10^5	5	553.7	1.85	3.22	4.16	2.0
Σ-M5E5-R35	129.9	5×10^5	35	80.72	4.84	8.60	11.11	2.0
Σ-M1E5-R15	141.5	1×10^5	15	205.1	3.04	5.88	7.59	2.0
Σ-M5E4-R10	159.2	5×10^4	10	346.1	2.34	5.09	6.57	2.0
Σ-M2E5-R20	159.2	2×10^5	20	173.0	3.31	7.20	9.29	2.0
Σ-M5E4-R08	248.7	5×10^4	8	676.0	1.67	5.69	7.35	2.0
Σ-M2E4-R05	254.6	2×10^4	5	1107	1.31	4.55	5.88	2.0
Σ-M2E5-R15	282.9	2×10^5	15	410.2	2.15	8.31	10.7	2.0
α-A0.1	70.74	5×10^4	15	102.5	4.29	0.93	5.36	0.1
α-A0.2	70.74	5×10^4	15	102.5	4.29	1.32	5.36	0.2
α-A0.4	70.74	5×10^4	15	102.5	4.29	1.86	5.36	0.4
α-A0.8	70.74	5×10^4	15	102.5	4.29	2.63	5.36	0.8
α-A1.5	70.74	5×10^4	15	102.5	4.29	3.60	5.36	1.5
α-A2.0	**70.74**	$\mathbf{5 \times 10^4}$	**15**	**102.5**	**4.29**	**4.16**	**5.36**	**2.0**
α-A3.0	70.74	5×10^4	15	102.5	4.29	5.09	5.36	3.0
α-A6.0	70.74	5×10^4	15	102.5	4.29	7.21	5.36	6.0
α-A10.0	70.74	5×10^4	15	102.5	4.29	9.30	5.36	10.0

Note. — Columns display the following information (i) model name, (ii) initial cloud surface density, (iii) initial cloud mass, (iv) initial cloud radius, (v) initial cloud hydrogen number density, assuming a mean atomic weight of $\mu = 1.4$, (vi) initial cloud free-fall time, (vi) initial turbulent velocity dispersion, (viii) cloud escape velocity from the initial cloud radius, (ix) initial virial parameter. The fiducial model is shown in bold (Σ-M5E4-R15 and α-A2.0).

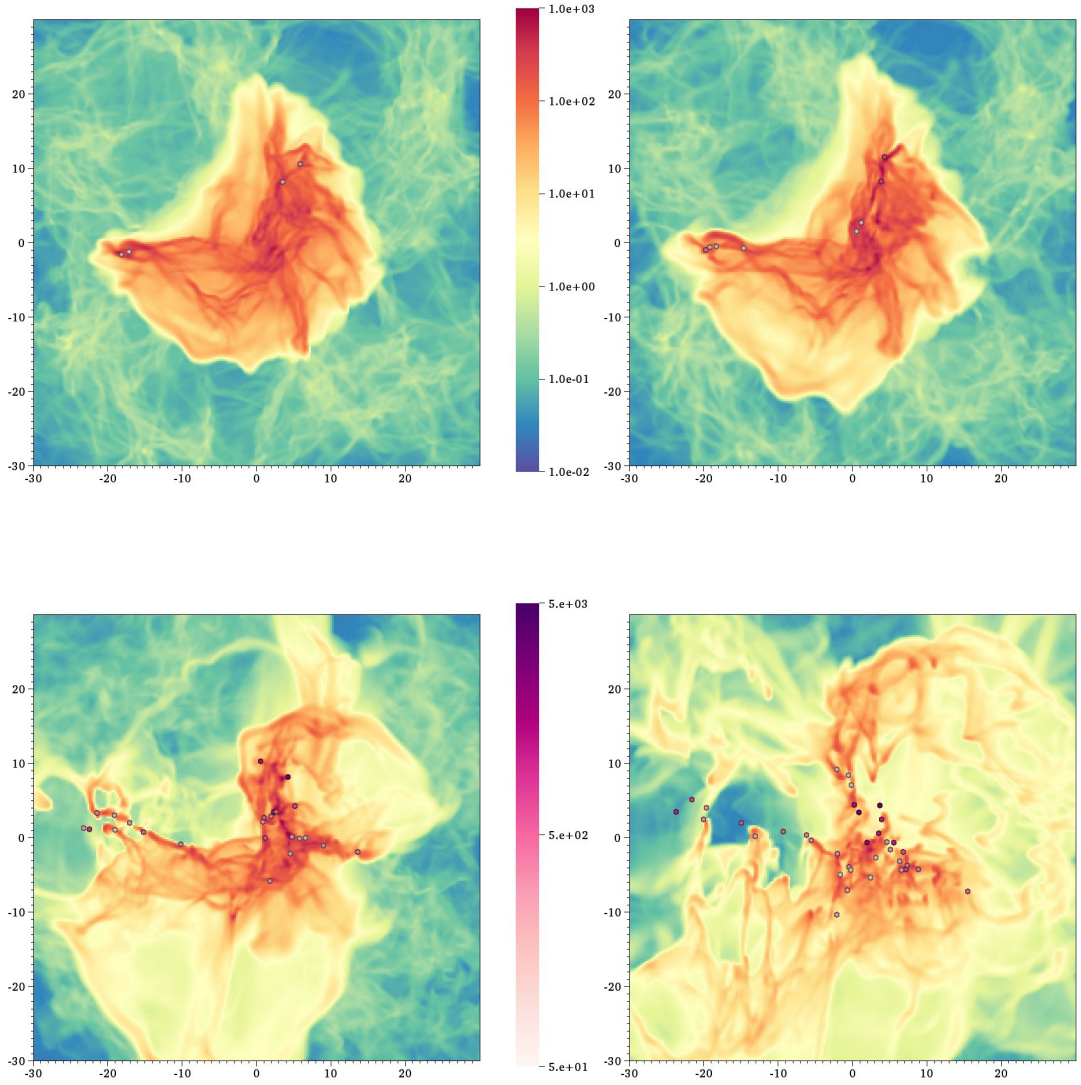

Fig. 2.— Snapshots from the fiducial model evolution. We show column densities in the y-z plane and all star particles projected onto the y-z plane, calculated at times t_2, t_{10}, t_{50} and t_{90}, when the total stellar mass is $2\%, 10\%, 50\%$ and 90% of the final value. This corresponds to $t/t_{\rm ff,0} = 0.43, 0.59, 1.06$ and 1.57 as shown, where $t_{\rm ff,0} = 4.29$ Myr is the initial free-fall time in the cloud. The color scale for the gas column density (top) is in units of $M_\odot$ pc^{-2} and the color scale for the particle mass (bottom) is in units of $M_\odot$. The box size is 60 pc, 4 times the initial cloud radius.

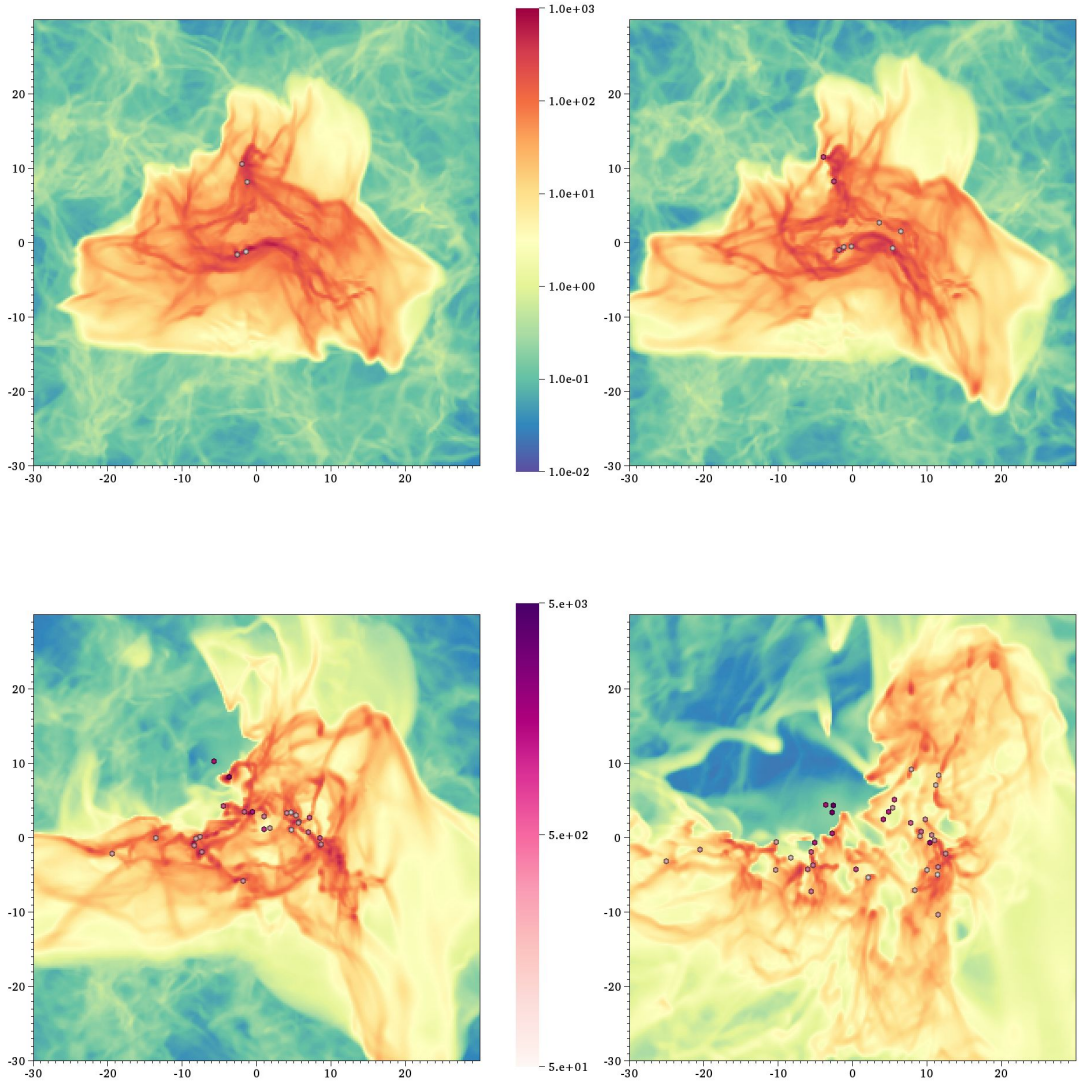

Fig. 3.— Same as Figure 2 except column densities are projected on the x-y plane. The cloud very rapidly develops a filamentary structure with mass preferentially gathered along the x-axis. Star formation then proceeds with the cloud remaining filamentary until a critical mass of stars drives away the remaining gas via radiation forces.

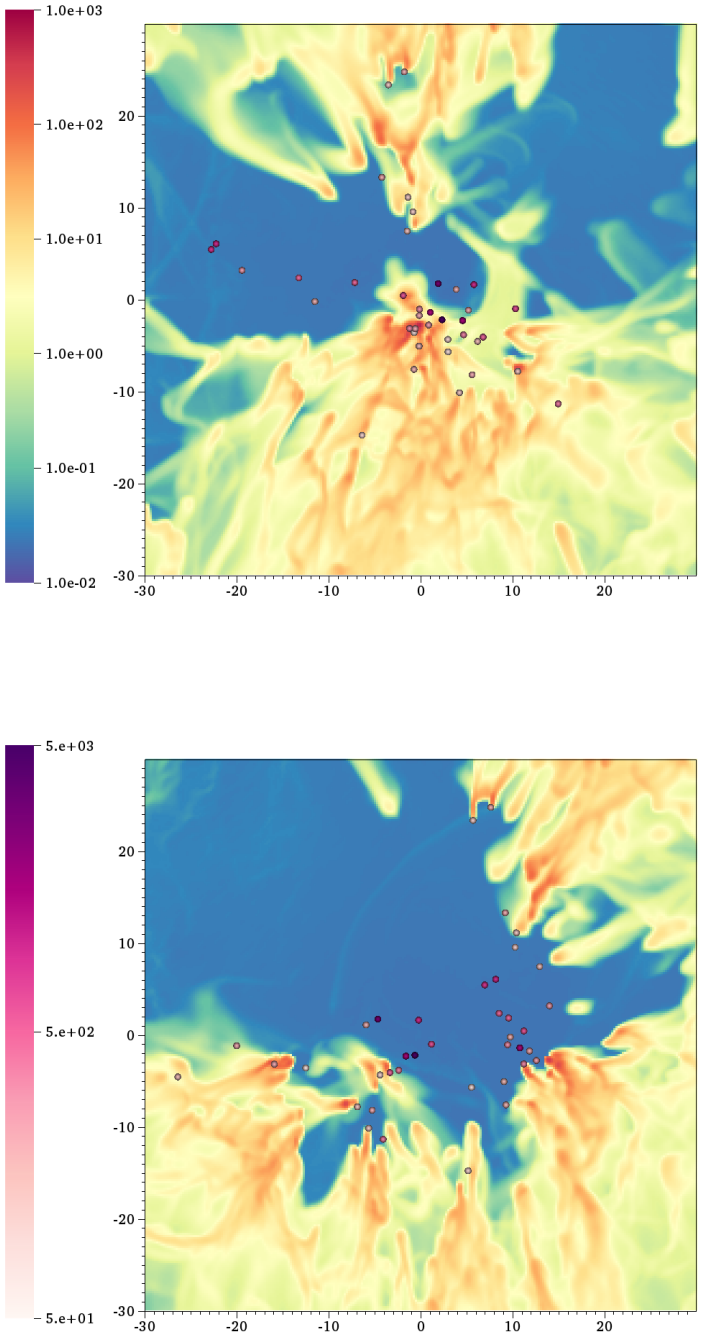

Fig. 4.— As in Figures 2 and 3 we show column densities projected in the y-z (top) and x-z (bottom) planes, both at times $t/t_{\rm ff,0} = 2$. The color scale for the gas column density (top) is in units of $M_\odot$ pc^{-2} and the color scale for the particle mass (bottom) is in units of $M_\odot$.

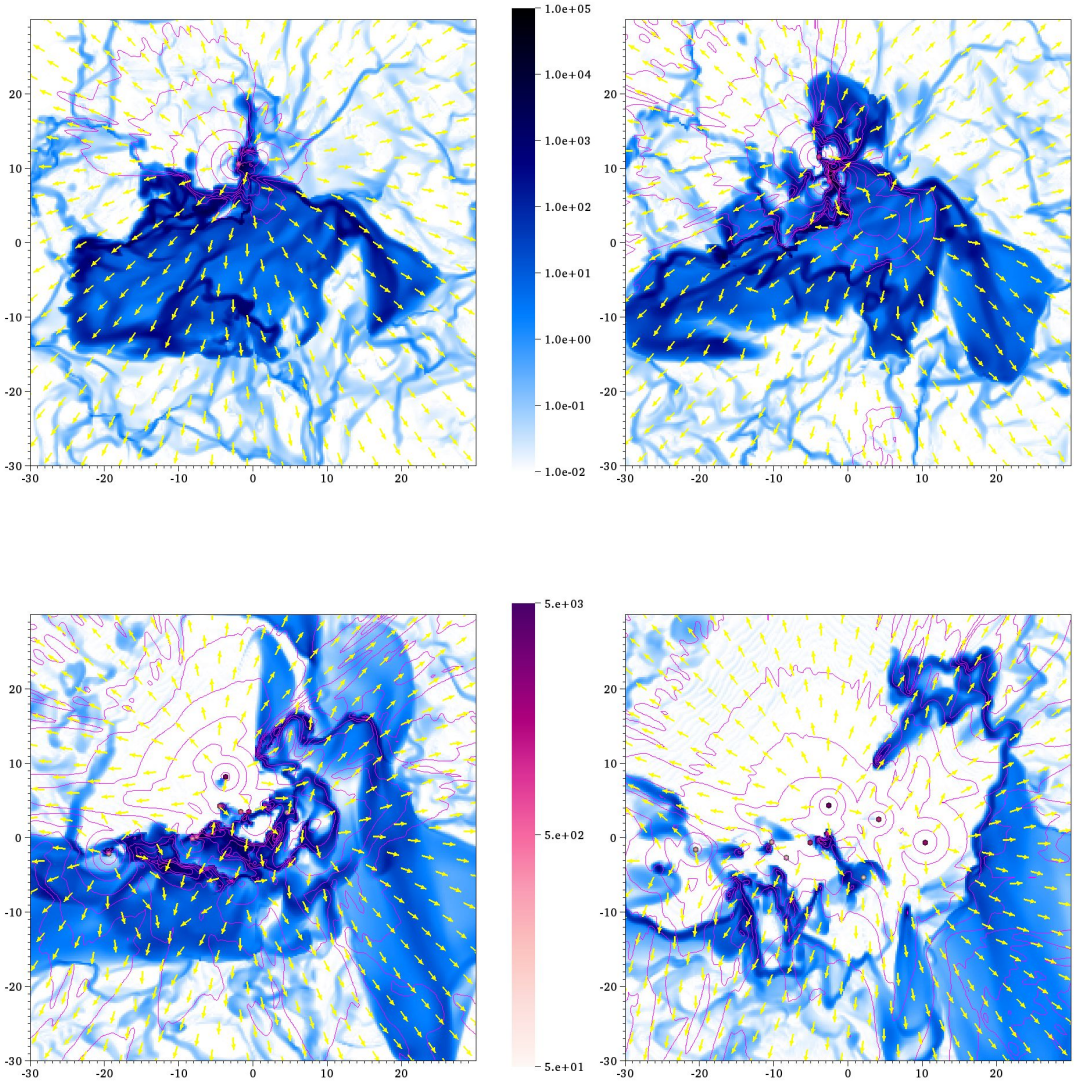

Fig. 5.— Snapshots of the density in our fiducial model. We show slices in the x-y plane passing through the position of the most massive star particle at the same times as for Figure 2. The directions of radiation flux vectors are overlaid in yellow. We also show, in pink contour lines, the radiation energy density at the same times. Contours represent differences of a decade from the peak energy density. Star particles within $\Delta z = \pm 2$ pc of the slice are plotted as circles. The color scale for the gas density n_H (blue, top) is in units of cm^{-3} and the color scale for the particle mass (red, bottom) is in units of $M_\odot$.

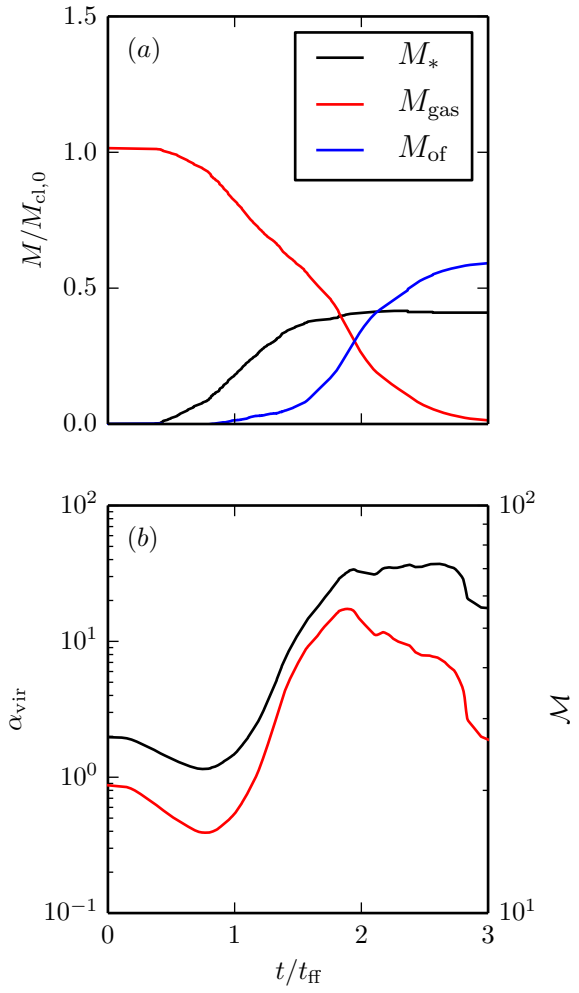

Fig. 6.— Time evolution of key global characteristics in the fiducial model. We show in (a) the mass history, with contributions from gas, stars, and outflows. Evolving cloud structure is seen in (b) with the gas virial parameter, defined as $\alpha_{\rm vir} \equiv 2E_K/|E_G|$ (black) and the Mach number defined as $\mathcal{M} = \sqrt{2E_K/M_{\rm cl,0}}/c_s$ (red).

presents a very different picture from the gas expansion seen in outflows driven by reprocessed radiation (Skinner & Ostriker 2015). At late stages in Figures 2 – 5 we see a central cavity surrounded by prominent high density fingers of gas extending inwards towards the most massive stars. Regions of low column density, as seen by the central sources, are evacuated first once the radiative force on them becomes super-Eddington. However, regions that are shielded by higher density clumps of gas only begin to be driven out at late times, giving rise to the prominent columns of gas.

This picture of filamentary collapse followed by rapid star formation and subsequent gas expulsion can also be seen in the time histories shown in Figure 6. In Figure 6a, we show the evolution of the total mass in stars, gas, and outflows from the simulation volume. While the cloud is initially collapsing there is relatively little star formation, although a small number of stars are formed through the effects of turbulence initiating compression. Meanwhile, the outflows driven by this initial turbulence only start leaving the simulation volume at $\sim 0.8t_{\rm ff,0}$, which is roughly the time taken for gas traveling at ~ 2 times the escape velocity to reach the corner of the box.

At around the same time ($\sim 0.8t_{\rm ff,0}$) there is a break in the stellar mass evolution as stars begin forming more rapidly; the majority of the stellar mass is assembled over the next free-fall time. By $\sim 1.8t_{\rm ff,0}$ the accretion onto star particles is essentially complete, while radiation from these stars continues to accelerate the remaining gas so that it becomes unbound from the central cluster. By $\sim 3t_{\rm ff,0}$ most of the outflowing gas has left the simulation box.

The evolution of the global gas distribution is more difficult to characterize. One simple measure is the global virial parameter, which is a rough proxy for the collapse and expansion of the cloud and is shown in Figure 6b. Initially this decreases from its starting value of $\alpha_{\rm vir} = 2$ as the turbulence decays slightly and the total potential energy increases due to contraction along local filaments. However, as for the stellar mass, there is a break at around $\sim 0.8t_{\rm ff,0}$, where collapse ceases and radiation from the first star particles begins to unbind gas and drive outflows.

The evolution in Mach number parallels that of the virial parameter very closely. In fact, the two are well correlated until at least around $\sim 2\ t_{\rm ff,0}$, with $\mathcal{M} \propto \alpha_{\rm vir}^{0.4}$. This roughly corresponds to the evolution in Mach number for a shell expanding around a fixed central mass M. For a shell of fixed mass $M_{\rm sh}$, expanding with velocity v, the virial parameter is $\alpha_{\rm vir} = v^2 r/GM$, while the mass-weighted Mach number is roughly $\mathcal{M}^2 = (M_{\rm sh}/M)(v^2/c_s^2)$ so that $\mathcal{M}^2 = (GM_{\rm sh}/r)(\alpha_{\rm vir}/c_s^2)$. The evolution we find is slightly different from $\mathcal{M} \propto \alpha_{\rm vir}^{1/2}$ since the radius of the shell expands. In general though, we see that the evolution of both Mach number and virial parameter beyond $\sim 0.8\ t_{\rm ff,0}$ is dominated by the cloud expansion and not turbulence.

It is for this reason that the increase in Mach number has no correlated increase in the width of the lognormal distribution (see below), unlike the case for driven turbulence when the width of the density distribution is entirely set by the Mach number (Padoan & Nordlund 2011; Molina et al. 2012; Hopkins 2013; Krumholz 2014; Thompson & Krumholz 2016). While the lowest density regions, which are expanding away at high velocity, dominate the evolution of the virial parameter

and the Mach number, they have little influence on the density distribution since, until late times, they only represent around 10 to 20 % of the mass. Therefore, the lognormal density distribution, which is fit to the majority of gas remaining in the cloud, shows no significant change over the bulk of star formation.

A measure quantifying the evolution of the gas is the shape of the gas density distribution (PDF). In Figure 7 we show the density distribution at two separate times ($t_{10} = 0.59\ t_{\rm ff,0}$ in black and $t_{50} = 1.06\ t_{\rm ff,0}$ in red). We show only the mass distribution, since the distribution by volume comprises more than 90% empty space. We see that by $\sim 0.6\ t_{\rm ff,0}$, when the virial parameter begins to turn around, the gas density is roughly lognormal in shape, characteristic of supersonic turbulence (Vazquez-Semadeni 1994; Ostriker et al. 2001; Vázquez-Semadeni & García 2001; Federrath et al. 2009). Interestingly, even towards the end of star formation, the shape of the distribution is not significantly different at the high density end. Certainly, there is an excess of low density gas escaping the cloud, but the highest density portion, which represents the star forming regions, remains essentially the same.

Our fiducial simulation displays a number of key stages of evolution. Initially, there is rapid collapse and structure formation driven by turbulent compression and self-gravity, resulting in a filamentary gas distribution within around half a free-fall time. This is followed by on-going collapse under self-gravity, during which the filamentarity remains while collapse around the density peaks begins to form stars at an accelerating rate. Starting at $t \sim 0.8 t_{\rm ff,0}$ there is a transition from collapse dominated by self-gravity to cloud expansion driven by radiative feedback, where the lowest density regions are accelerated out of the cloud first, but where the star forming regions remain largely unaffected. Star formation is largely complete by $\sim 1.5 t_{\rm ff,0}$, and the remnant gas in the cloud is mostly removed by radiation-driven outflows within the next free-fall time.

3.2. Convergence Tests

In numerically simulating turbulent cloud evolution with radiation feedback, we want to ensure that (i) we accurately model the formation of stars driven by turbulence and gravitational collapse and (ii) we accurately model gas dynamics driven by radiative forces.

The first of these is related to the methodology of sink-particle creation, which is necessary because gas collapse becomes unresolved on the numerical grid. To have a sufficiently "fine-grained" representation of star formation, we would like to ensure that a single star particle cannot represent a substantial fraction of the cloud. The minimum sink particle mass is defined in terms of the density

threshold and the cell size $\Delta x = L/N = 4r_0/N$ as

$$M_{\rm sink,min} = \rho_{\rm th}(\Delta x)^3 \quad (6)$$

$$= \frac{8.86 c_s^2 \Delta x}{G\pi} = \frac{35.4 c_s^2 r_0}{G\pi N} \quad (7)$$

$$= 24.5 \ {\rm M}_\odot \left(\frac{c_s}{0.2 \ {\rm km \ s^{-1}}}\right)^2 \left(\frac{r_0}{10 \ {\rm pc}}\right) \left(\frac{256}{N}\right). \quad (8)$$

As a practical limit, we require that this mass is not more than $\sim 0.1\%$ of the initial cloud mass, so that a reasonable number of star particles can be created, even at low efficiencies. This translates to around $\Sigma \gtrsim 10$ M$_\odot$ pc^{-2} for the masses and radii that we consider, though we will examine this limit in more detail below.

We also need to ensure that we can sufficiently resolve the highest density regions, which are converted into star particles. High-resolution simulations of compressible turbulence modeling molecular cloud conditions generally show both a lognormal component around the mean density, characteristic of supersonic turbulence (Vazquez-Semadeni 1994; Ostriker et al. 2001; Vázquez-Semadeni & García 2001; Federrath et al. 2009), and an extended power law tail that arises when self-gravity is included (Klessen et al. 2000; Dib & Burkert 2005; Vázquez-Semadeni et al. 2008; Federrath et al. 2008; Ballesteros-Paredes et al. 2011; Kritsuk et al. 2011; Collins et al. 2012; Federrath & Klessen 2013). There is evidence that the power-law component is specifically associated with dense prestellar cores (see below). High-resolution observations of star forming clouds also generally show power law tails in the surface density whenever there is star formation (Kainulainen et al. 2009; Schneider et al. 2013, 2015), although there is some debate as to whether the power law arises from self-gravity (Brunt 2015) and what is the exact relationship between the surface density and density distributions (Brunt et al. 2010).

By contrast, when we consider the mass-weighted density distribution in our simulations, we find no strong evidence for a power law tail. In other simulations, this tail is associated with self gravity and, in particular, with collapsing cores, which themselves have power-law density profiles (Kritsuk et al. 2011; Lee et al. 2015). Thus, its absence could indicate that we do not capture the details of core collapse. In general, these power law tails are seen to begin at densities ~ 100 times the mean density (Kritsuk et al. 2011; Dib & Burkert 2005; Vázquez-Semadeni et al. 2008; Collins et al. 2012; Federrath & Klessen 2013; Lee et al. 2015). In our fiducial simulation, the threshold for star particle formation is at $\rho \sim 150\rho_0$ (or $n_H \sim 1.5 \times 10^4$ cm^{-3}). With the peak of the lognormal in Figure 7 at $\ln(\rho_{\rm peak}/\rho_0) \sim 2.2$ (or $n_H \sim 10^3$ cm^{-3}) and a variance of $\sigma_{\ln\rho} \sim 2$, the 1σ density will be at $n_H \sim 10^4$ cm^{-3}; hence there is only a limited range of density over which to sample the power law. Effectively, the majority of what would make up the power law core is hidden in these star particles. Nevertheless, tests at higher resolution (see below) appear to indicate that all our models are converged in the SFE.

In order to test how well our code captures the physics of gas expansion, we conducted a number of tests involving a spherical shell of gas surrounding a single central star particle, and the

results of these are shown in Appendix A. These tests suggest that the primary numerical limit in simulating the interaction between radiation and gas with high accuracy is in ensuring that $\tau_{\rm cell} = \rho\kappa\Delta x \lesssim 2$ for the optical depth within individual cells. This corresponds to a maximum density that is resolution dependent:

$$n_{\rm H,max} = 2.8 \times 10^3 \ {\rm cm}^{-3} \left(\frac{\Delta x}{0.1 \ {\rm pc}}\right)^{-1} \left(\frac{\kappa}{1000 \ {\rm cm}^2 \ {\rm g}^{-1}}\right)^{-1} \left(\frac{\tau_{\rm cell,max}}{2}\right). \quad (9)$$

To gain an idea of how the optical depth evolves in the fiducial model, we show in Figure 8 snapshots of the spatial distribution of $\tau_{\rm cell}$ at the same four times as Figures 2-5. We see that even in this model, which has an initial surface density of $\Sigma_{\rm cl,0} = 71 \ {\rm M}_\odot \ {\rm pc}^{-2}$ and $\tau_{\rm cell,init} = 3\Sigma_0\kappa/N = 0.17$, over time the densest regions are enhanced by at least two orders of magnitude and a portion of the cells have optical depth $\tau_{\rm cell} \gtrsim 2$.

Even if some localized regions have large single-cell optical depth and do not resolve the radiation field well, the overall resolution may still be acceptable. In particular, by around a free-fall time, when stars are beginning to drive gas away from the sites of star formation, only very small regions have $\tau_{\rm cell} \gtrsim 2$. While we may underestimate the radiation force applied to a small number of cells, for the bulk of the mass we still follow the physics governing the expulsion of gas and the propagation of the radiation field.

Quantitatively, the distribution of $\tau_{\rm cell}$ has a long tail, such that close to 90% of the mass is found an order of magnitude below the maximum density. In Figure 9a we show the $50^{\rm th}$ percentile, $90^{\rm th}$ percentile, and maximum of the $\tau_{\rm cell}$ distribution as a function of time for the fiducial model. Even though the maximum $\tau_{\rm cell}$ reaches ~ 20 at quite early times, $\tau_{\rm cell,90} \approx 1$ for the majority of the simulation, which is only a factor of 10 higher than the initial optical depth. A similar ratio of $\tau_{\rm cell,90}/\tau_{\rm cell,init}$ appears to hold in higher surface density models. We see in Figure 9b that a model with $\Sigma \approx 280 \ {\rm M}_\odot \ {\rm pc}^{-2}$, reaches $\tau_{\rm cell,90} \approx 8$. This suggests that up to cloud surface densities $\Sigma \approx 100 \ {\rm M}_\odot \ {\rm pc}^{-2}$, $\tau_{\rm cell,90}$ will remain below ~ 2, while for higher surface density clouds $\tau_{\rm cell,90}$ may be higher.

The above considerations suggest that we can satisfactorily simulate clouds over a range of initial surface densities $10 \ {\rm M}_\odot \ {\rm pc}^{-2} \lesssim \Sigma \lesssim 100 \ {\rm M}_\odot \ {\rm pc}^{-2}$. However, in reality we may be able to do better than that, since as discussed in Appendix A, even at higher cell optical depths, we only underestimate the velocity of gas expulsion by around $\sim 10\%$. We are primarily interested in ensuring that we are able to accurately capture the net star formation efficiency and evolution in response to radiation. By looking at how these properties vary as we change the numerical resolution, we may gain a better idea of what range of parameters provide converged results.

Figure 10a shows evolution of the global efficiency of star formation in the fiducial model as a function of time with varying numerical resolution for $N = 128, 256$, and 512. We see that in the $N = 128$ case, the fiducial simulation is clearly not converged. It shows substantial differences from the higher resolution models, including "stair-stepping" in the stellar mass history. This makes sense, since the minimum sink mass for this simulation is around $M_{\rm sink} \approx 80 \ {\rm M}_\odot$, which is close

to 0.2% of the global cloud mass. Importantly however, the $N = 256$ and $N = 512$ models are converged, and even though the $N = 128$ model underestimates the SFE at intermediate times, its final SFE is the same as for the higher resolution models.

We show also in Figure 11 the density distribution at t_{50}, when 50% of the final stellar mass has been assembled. With resolution reduced by a factor of two in the 128^3 models, the star particle density threshold is at $\sim 40\rho_0$ or $n_H \sim 4\times10^3$ cm^{-3} compared to $\rho \sim 150\rho_0$ or $n_H \sim 1.5\times10^4$ cm^{-3} for $N = 256^3$. We believe that the lack of convergence evident in the low resolution models (see Figure 10), which leads to an underestimation of the SFE, is because this threshold is not sufficiently high compared to the lognormal distribution, as evident from the cutoff in Figure 11 here. However, the convergence of the 256^3 and 512^3 models in terms of stellar efficiency (see Figure 10) would suggest that in our highest resolution models, we capture the distribution of gas dominated by turbulence, with only collapsing regions assigned to sink particles. Thus, while insufficient resolution can lead to an underestimate of the SFE, we believe that increasing resolution beyond a certain point primarily provides improved resolution of collapsing cores without changing the SFE. This speculation could be tested with AMR simulations.

A similar picture holds for models at the highest surface densities we simulate. In Figure 12a we again show evolution of the global stellar efficiency as a function of resolution, but in this case for a cloud of mass $M_{\rm cl,0} = 2 \times 10^5\ M_\odot$. For this model, the $90^{\rm th}$ percentile in optical depth lies at $\tau_{\rm cell,90} \sim 8$, which is a factor of 4 larger than the limit found in Appendix A for best accuracy in capturing radiation forces. However, the larger values of $\tau_{\rm cell}$ do not have a major impact on the evolution of the global efficiency, presumably because errors are only $\sim 10\%$ at larger $\tau_{\rm cell}$ (see Appendix A), and because only a small fraction of the gas has large $\tau_{\rm cell}$. As for the fiducial cloud, stars do begin forming slightly earlier in the higher resolution run and they do form at a slightly faster rate, but the final efficiency is the same.

In Figures 10b and 12b, we show the gas virial parameter, for our fiducial and highest-Σ models at different resolution. As for the stellar efficiency, our simulations are not well converged at $N = 128$, but there are few differences between the $N = 256$ and $N = 512$ runs, at least until the bulk of star formation is already complete.

4. Star Formation Efficiencies

We now turn to the central question of this paper: what mechanisms are dominant in setting the star formation efficiency in gaseous clouds, and how do these depend on cloud parameters? As the key elements are turbulence and radiative feedback, it is interesting to consider these effects separately at first.

Table 3. Model Results

Model	ε	$\varepsilon_{\rm adj}$	t_* [$t_{\rm ff}$]	$t_{1/2}$ [$t_{\rm ff}$]	$t_{90\%}$ [$t_{\rm ff}$]	$t_{\rm unb}$ [$t_{\rm ff}$]	β	$t_{\rm break}$ [$t_{\rm ff}$]	$\varepsilon_{{\rm ff},\bar{\rho}}$
Σ-M2E4-R25	0.12	0.14	0.67	0.88	1.51	$1.14^{+0.18}_{-0.24}$	_[a]	_[a]	_[a]
Σ-M5E4-R35	0.18	0.20	0.63	1.07	2.05	$1.17^{+0.22}_{-0.23}$	_[a]	_[a]	_[a]
Σ-M2E4-R20	0.22	0.25	0.61	1.08	1.72	$1.35^{+0.25}_{0.12}$	_[a]	_[a]	_[a]
Σ-M5E4-R25	0.25	0.28	0.52	1.01	1.71	$1.18^{+0.16}_{-0.20}$	1.64	0.80	0.49
Σ-M1E5-R35	0.23	0.26	0.49	1.00	1.53	$1.22^{+0.19}_{-0.22}$	0.77	0.85	0.24
Σ-M2E4-R15	0.30	0.34	0.47	1.07	1.65	$1.21^{+0.12}_{-0.19}$	1.08	0.70	0.37
Σ-M1E4-R10	0.30	0.34	0.54	1.09	1.64	$1.29^{+0.16}_{-0.20}$	1.11	0.78	0.34
Σ-M5E4-R20	0.32	0.36	0.46	1.02	1.51	$1.19^{+0.14}_{-0.16}$	1.17	0.73	0.45
Σ-M1E4-R08	0.39	0.44	0.47	1.11	1.75	$1.34^{+0.16}_{-0.20}$	0.85	0.92	0.41
Σ-M1E5-R25	0.32	0.37	0.46	1.05	1.48	$1.26^{+0.14}_{-0.19}$	1.25	1.02	0.36
Σ-M2E5-R35	0.31	0.35	0.47	1.08	1.51	$1.32^{+0.16}_{-0.24}$	0.87	0.74	0.29
Σ-M5E3-R05	0.42	0.49	0.54	1.17	1.95	$1.45^{+0.17}_{-0.21}$	0.69	1.02	0.37
Σ-M2E4-R10	0.42	0.48	0.44	1.08	1.58	$1.33^{+0.16}_{-0.22}$	0.93	0.76	0.43
Σ-M5E4-R15	**0.42**	0.48	**0.37**	**1.06**	**1.57**	$1.33^{+0.14}_{-0.21}$	**0.95**	**0.81**	**0.43**
Σ-M1E5-R20	0.41	0.47	0.32	1.02	1.56	$1.31^{+0.18}_{-0.21}$	0.88	0.84	0.45
Σ-M2E4-R08	0.49	0.56	0.42	1.10	1.71	$1.46^{+0.18}_{-0.24}$	0.94	0.80	0.49
Σ-M2E5-R25	0.41	0.41	0.32	1.04	1.57	$1.43^{+0.20}_{-0.24}$	0.87	0.92	0.42
Σ-M1E4-R05	0.52	0.60	0.44	1.16	1.80	$1.59^{+0.23}_{-0.25}$	0.83	0.91	0.51
Σ-M1E5-R15	0.52	0.59	0.29	1.04	1.63	$1.40^{+0.22}_{-0.13}$	1.31	1.14	0.45
Σ-M5E4-R10	0.58	0.65	0.31	1.09	1.67	$1.55^{+0.21}_{-0.28}$	0.95	0.78	0.49
Σ-M2E5-R20	0.48	0.54	0.28	1.21	1.86	$1.43^{+0.31}_{-0.18}$	1.05	0.63	0.51
Σ-M5E4-R08	0.62	0.70	0.31	1.11	1.77	$1.73^{+0.28}_{-0.30}$	1.15	0.78	0.49
Σ-M2E4-R05	0.61	0.69	0.37	1.20	1.86	$1.83^{+0.34}_{-0.32}$	1.11	0.78	0.49
Σ-M2E5-R15	0.61	0.69	0.26	1.08	1.63	$1.75^{+0.25}_{-0.25}$	1.30	0.56	0.47
α-A0.1	0.91	0.91	0.67	1.02	1.13	$1.16^{+0.04}_{-0.13}$	1.24	0.83	0.42
α-A0.2	0.87	0.87	0.60	1.04	1.22	$1.27^{+0.06}_{-0.19}$	1.19	0.78	0.43
α-A0.4	0.67	0.67	0.51	0.99	1.23	$1.28^{+0.07}_{-0.17}$	1.39	0.75	0.44
α-A0.8	0.58	0.59	0.44	1.00	1.31	$1.28^{+0.10}_{-0.15}$	0.98	0.77	0.36
α-A1.5	0.47	0.54	0.43	1.03	1.54	$1.29^{+0.17}_{-0.19}$	1.10	0.70	0.41
α-A2.0	**0.42**	0.48	**0.37**	**1.06**	**1.57**	$1.33^{+0.14}_{-0.21}$	**1.03**	**0.80**	**0.43**
α-A3.0	0.28	0.35	0.36	0.99	1.47	$1.33^{+0.18}_{-1.33}$	0.92	0.80	0.36
α-A6.0	0.12	0.35	0.27	1.03	1.66	_[b]	1.57	0.87	0.16
α-A10.0	0.05	0.32	0.14	1.00	1.39	_[b]	0.20	1.95	0.07

Note. — Columns display the following information (i) final efficiency of star formation, (ii) final efficiency adjusted for the inital turbulence-driven mass outflow, (iii) time of first star formation, (iv) time at which half of the final stellar mass is assembled, (v) time at which 90% of the final stellar mass is assembled, (vi) time at which the cloud becomes unbound (reaches a virial parameter of $\alpha_{\rm vir} = 5^{+5}_{-3}$), (vii) post-break power law exponent of the stellar mass evolution using a double power-law fit, (viii) break time in double power law fit to the stellar mass evolution, and (ix) star formation efficiency per freefall time as defined in Equation 25.

[a]: In these models, the star formation rate was not fit as there were insufficient numbers of discrete star particles to perform a meaningful fit

[b]: In these models, $t_{\rm unb}$ was not calculated since the models were initially unbound.

4.1. The Effect of Radiative Feedback

We begin by presenting results from a set of models with the initial turbulent energy a factor of 20 lower than in the fiducial case (i.e., with $\alpha_{\rm vir,0} = 0.1$). In Figure 13, we show snapshots of the column density in the x-y plane for a model cloud with the fiducial initial surface density, but with reduced initial turbulence. The lack of turbulent support means that for the first $\sim 0.6 t_{\rm ff,0}$, the cloud undergoes nearly free-fall collapse, contracting to around 40% of its initial radius and converting potential to kinetic energy. Star formation only begins once this contraction is complete and the virial parameter for the cloud is near unity.

After the initial contraction and virialization, the evolution is quite similiar to the fiducial case as the gas density distribution becomes similarly filamentary, with preferential directions set by the seed turbulent field. Low initial turbulence simplifies the picture in several respects. Firstly, stars tend to form very close to the center of the cloud, with very little initial momentum away from the center of mass. This can be seen in the lower two panels of Figure 13, where star particles close to the cloud center eventually converge to a single, massive, central star particle. Secondly, star formation occurs on a relatively short timescale compared to the initial free-fall time due to the high densities and small physical length scales involved. Therefore, the majority of stellar mass is assembled in less than 25% of a free-fall time after the initial collapse.

As a very simple model of star formation, one could imagine an initial roughly spherical collapse, until the cloud reaches a characteristic radius xr_0 at which the virial parameter is of order unity. Once stars have begun to form close to the center and have evacuated their local environment, we might expect the remnant cloud's effective radius to evolve under the competing effects of the inward force of gravity and the outward force of radiation. Star formation, or at least accretion on to the young central star cluster would then continue so long as gravity dominates over the effects of stellar feedback, and it would stop once enough stars form for radiation forces to disperse the remaining gas in the cloud.

This picture is essentially that of a radiation dominated HII region, with a single, central stellar cluster that stops accreting mass once the luminosity is sufficient to drive away all surrounding gas. Such systems, in different limits, have been analyzed previously in Elmegreen (1983); Scoville et al. (2001); Krumholz & Matzner (2009); Murray et al. (2010); Fall et al. (2010); Kim et al. (2016) and considering effects of inhomogeneity by Thompson & Krumholz (2016). We review the ideas involved, connecting to the results of our simulations.

We consider a system consisting of a spherical shell of gas with mass $M_{\rm sh} = (1-\varepsilon)M_{\rm cl,0}$ surrounding a point mass representing a stellar cluster of mass $M_* = \varepsilon M_{\rm cl,0}$. At any point in time, the circumcluster shell will have a distribution of surface densities around the mean surface density $\langle \Sigma^c(\varepsilon, x, \Sigma_{\rm cl,0})\rangle$, where $\Sigma_{\rm cl,0} = M_{\rm cl,0}/\pi r_0^2$ is the initial, observed cloud column density. The mean surface density would decrease as gas is converted to stars, but increase under global collapse, so the outcome depends on the initial cloud reference surface density $\Sigma_{\rm cl,0}$, the time-dependent stellar efficiency ε, and the radius to which the cloud collapses xr_0. We note also that

here $\langle\Sigma^c\rangle = M_{\rm sh}/(4\pi r^2)$ represents the mean surface density seen by the central star cluster, as distinct from the cloud column density seen by an external observer $M_{\rm sh}/(\pi r^2) = 4\langle\Sigma^c\rangle$.

In this simple model, assuming all the flux is absorbed, the radiative force per unit area in the shell due to the central luminous source is $F_{\rm rad} = L/(4\pi r^2 c) = \Psi M_*/(4\pi r^2 c)$. Meanwhile, there are two components to the gravitational force applied to a local patch of surface density Σ^c. Firstly, there is the force per unit area due to the central point mass $F_1 = GM_*\Sigma^c/r^2$. Secondly, unlike previous studies (Fall et al. 2010), we also include a term for the self-gravity of the shell per unit area, which is $F_2 = GM_{\rm sh}\Sigma^c/(2r^2)$. The exact normalization of this latter force is derived for a uniform density shell and may change with surface density variations. However, with the basic argument that gas at the radial center of the shell will feel the force of all interior mass, or half the total shell mass, this is at least approximately correct even when the shell surface density is not uniform.

For a region with surface density Σ^c, the Eddington ratio $F_{\rm rad}/F_{\rm grav} = F_{\rm rad}/(F_1 + F_2)$ is equal to $\Psi M_*/[2\pi cG\Sigma^c(2M_* + M_{\rm sh})]$. At a time when the net star formation efficiency is ε, we can evaluate the Eddington surface density Σ_E such that the inward and outward forces balance and the Eddington ratio is unity:

$$\begin{aligned}\Sigma_E &= \frac{\varepsilon}{\varepsilon+1}\frac{\Psi}{2\pi cG} \\ &= 759\ {\rm M}_\odot\ {\rm pc}^{-2}\frac{\varepsilon}{1+\varepsilon}\left(\frac{\Psi}{2000\ {\rm erg\ s^{-1}\ g^{-1}}}\right); \end{aligned} \quad (10)$$

here we have used $M_* = \varepsilon M_{\rm cl,0}$ and $M_{\rm sh} = (1-\varepsilon)M_{\rm cl,0}$. In local patches where surface densities within the shell exceed the Eddington level $\Sigma^c > \Sigma_E$, gas will be able to continue collapsing, and where $\Sigma^c < \Sigma_E$, the gas can can be driven outwards. We note that even for $\varepsilon \to 1$, $\Sigma_E < 400{\rm M}_\odot\ {\rm pc}^{-2}$, implying that UV radiation feedback by itself is not expected to be effective in expelling gas from very high surface density GMCs (see Skinner & Ostriker 2015, for a study of reprocessed radiation effects in this regime)

We now consider a very simple hypothesis, similar in spirit to Fall et al. (2010), in which star formation, and accretion halts completely once the mean circumcluster surface density reaches the Eddington value, $\langle\Sigma^c\rangle = \Sigma_E$. For a given $\varepsilon(t)$, the mean circumcluster surface density can be related to the initial cloud mass and surface density by

$$\begin{aligned}\langle\Sigma^c\rangle &= \frac{(1-\varepsilon)M_{\rm cl,0}}{4\pi(xr_0)^2} \\ &= \frac{(1-\varepsilon)}{4x^2}\Sigma_{\rm cl,0}, \end{aligned} \quad (11)$$

where the $(1-\varepsilon)$ comes from the conversion of gas to stars, the factor of x from cloud contraction, and the additional factor of 4 from the fact that $\Sigma_{\rm cl,0} = M_{\rm cl,0}/(\pi r_0^2)$ is an observed column density. If we substitute $\langle\Sigma^c\rangle$ from Equation (11) for Σ_E in Equation (10), we obtain a simple relationship

between the star formation efficiency and the initial cloud surface density:

$$\begin{aligned} \frac{1}{\varepsilon} - \varepsilon &= \frac{2\Psi x^2}{\pi c G \Sigma_{\rm cl,0}} \\ &= 30.5 x^2 \left(\frac{\Sigma_{\rm cl,0}}{100 \text{ M}_\odot \text{ pc}^{-2}} \right)^{-1} \left(\frac{\Psi}{2000 \text{ erg s}^{-1} \text{ g}^{-1}} \right). \end{aligned} \quad (12)$$

Similar to Equation (6) of Fall et al. (2010), this predicts a low efficiency ($\varepsilon \sim 3\%$) of star formation in GMCs with $\Sigma \sim 100$ M$_\odot$ pc^{-2}, typical of the Milky Way.

To test whether this simple radiative force balance argument can capture simulated cloud behavior, we first consider low turbulence models, $\alpha_{\rm vir,0} = 0.1$, for a range of surface densities. In Figure 14 we show the final star formation efficiency for this set of simulations, which have initial masses and radii the same as for our Σ-series.

In Figure 14 we also show the fit of the simple model represented by Equation (12) to our cloud simulations. In the low turbulence case, the shape of Equation (12) fits relatively well, matching the drop in efficiencies in our low surface density clouds. However, the best fit requires a value of $x^2 = 0.005$, or linear contraction of the cloud radius by $x \sim 0.07$. Modeling the cloud contraction is not straightforward due to the non-spherical gas distribution. Even so, it is clear from looking at Figure 13 that the low-turbulence clouds collapse to around $x \sim 1/2$ of their initial radii. This is a factor of more than five larger than the nominal best fit. We conclude that although Equation (12) can fit the numerical results for the reduced turbulence models, the parameters required are not consistent with the true evolution and structure of the cloud.

The source of this discrepancy is likely that the surface density seen by the radiation field is not uniform, but is instead distributed over at least an order of magnitude. As a consequence, at a given ε, even if the mean surface density in a cloud is comparable to Σ_E as given in Equation (10), there will be many higher surface density regions that can still collapse, leading to an increase in ε. Conversely, as noted by Thompson & Krumholz (2016), this also means that low surface density regions can be driven away even when the stellar luminosity is not sufficient to drive off the bulk of a cloud's mass. To assess the impact of this, we now turn to the effect that turbulence has on changing the gas density distribution and therefore also this simple picture of star formation regulation.

4.2. The Effect of Turbulence

Qualitatively, we expect turbulence to affect cloud evolution in two separate ways. Firstly, since our Σ-series clouds are only marginally bound, the initial turbulence will unbind a certain amount of the gas on the edges of the cloud immediately. This effectively lowers the initial surface density, and sets a maximum on the star formation efficiency. Secondly and more fundamentally, turbulence dramatically alters the density and surface density distributions.

We may gain a more concrete idea of what turbulence means for star formation by considering a simplified version of our Σ- and α-series in which radiative feedback is turned off, so that only turbulence and self-gravity set the star formation rate. In these simulations, star formation continues until all the gas is consumed, and the only gas that is not converted to stars is that which is initially unbound by the turbulence.

Figure 15 shows the resulting column density evolution for our fiducial model with no radiation. Until more than a freefall time the no-feedback and feedback cases are very similar. Gas collapses along the same filaments, with the same initial density structure. Moreover, stars appear to form at roughly the same rate despite the lack of radiative feedback to stir up additional turbulence. This is likely because even though the no-feedback model does not drive out low-density gas, and so does not show the same prominent columns seen in Figures 3 – 5, the high density sites of star formation remain similar. Differences between the two models appear only at late times, since in the model without feedback, star formation continues at the same rate for close to an extra free-fall time. Eventually, the majority of the no-feedback cloud is converted into stars. Only the gas driven away by the initial turbulence does not contribute to star formation.

In fact, if we compare the evolution of stellar mass in all of our Σ and α-series models (discussed in detail below) with and without feedback, we find that they are essentially identical up until the point that radiation begins to disperse the gas. We may define a time $t_{\rm fb}$, at which there is a 10% difference in stellar mass between simulations with and without radiation feedback. We then define $f_{\rm fb}$, the fraction of the final stellar mass in the feedback model that has been assembled by time $t_{\rm fb}$. In Figure 16 we show $f_{\rm fb}$ as a function of both initial surface density and virial parameter. We see that for almost all models, except for those at low surface density or high virial parameter (where there is little stellar mass formed), between 70 and 90% of the stellar mass is assembled before radiative feedback can significantly affect star formation.

This suggests that the star formation rate in our clouds is determined primarily by the initial conditions, via the density structure that is imposed by the interplay between gravity and turbulence. The majority of stellar mass growth is through stars formed early on before radiative feedback becomes important. As will be discussed further in Section 4.6, radiation does little to suppress this early star formation. Instead, radiative feedback is primarily important in rapidly truncating star formation by driving gas from the cloud, once sufficiently many stars have formed in the turbulent density field.

4.2.1. Turbulent Outflows

The most obvious initial effect of turbulence is the unbinding of small fractions of mass with high velocities in the tail of the distribution. We may calculate the total mass in outflows due to the initial turbulence alone by running simulations with no radiative feedback until all of the gas in the box is converted to stars. In these models, any gas that leaves the cloud is unbound by the

initial turbulence.

In Figure 17a, we show the corresponding outflow mass fractions $\varepsilon_{\rm of}$ for our no-feedback Σ-series models. The outflowing mass amounts to between 10 and 15% of the initial cloud mass, with little variation between low and high surface density. Without radiation, the primary dimensionless parameter that varies for different values of R and M at fixed $\alpha_{\rm vir,0} = 2.0$ is the Mach number $\mathcal{M}$. However, there is little direct dependence of the outflow mass on $\mathcal{M}$ at fixed $\alpha_{\rm vir,0}$, since the escape velocity from the edge of the cloud increases proportionally to the Mach number at fixed virial parameter.

As shown in Figure 17b, the outflow mass depends strongly only on the initial virial parameter $\alpha_{\rm vir,0} \propto \mathcal{M}^2/(GM/r)$, i.e., the strength of the turbulence relative to gravity. Below $\alpha_{\rm vir,0} \sim 1$, there is effectively no outflow, as seen for the case of $\alpha_{\rm vir,0} = 0.1$. Meanwhile, above $\alpha_{\rm vir,0} \sim 5$, the outflow mass fraction approaches unity.

The dependence on $\alpha_{\rm vir,0}$ can be understood in terms of the fraction of gas that escapes due to an initial turbulent velocity above the local escape velocity. For a uniform density cloud, the escape velocity at radius r is $v_e^2(r) = (GM/r_0)(3 - r^2/r_0^2)$, while in our models the initial velocity field is Gaussian with dispersion $v_{RMS}^2 = 3GM\alpha_{\rm vir,0}/(5r_0)$. Therefore, the total outflow mass fraction due to the initial turbulence is just the fraction of mass, at any given radius, above $v_e(r)$:

$$\varepsilon_{\rm of,init} = \int_0^1 dx\ 3x^2 \left[1 - {\rm erf}\sqrt{\frac{5(3-x^2)}{6\alpha_{\rm vir}}}\right]. \tag{13}$$

This quantity is indicated by the black curve in Figure 17b. For $\alpha_{\rm vir,0} \leq 3$, Equation (13) somewhat overestimates the total outflow mass, since the initial turbulence is damped, and gas in the cloud interior, which may have an initial velocity higher than the escape velocity, will nevertheless collapse to form stars. However, it does represent a reasonable estimate, since the majority of outflowing mass is on the outer edges of the cloud, where the escape velocity is lowest.

Above $\alpha_{\rm vir,0} \sim 3$, we no longer predict the outflow mass well since we cannot distinguish between gas that leaves the box and gas that becomes truly unbound. Even accounting for an escape velocity to $2r_0$ rather than infinity, $v_2(r)^2 = (GM/r_0)(2 - r^2/r_0^2)$, indicated by the red line in Figure 17b, we still underestimate the outflow mass at large $\alpha_{\rm vir,0}$, since the remaining gas mass is at too low density to form a significant mass in stars, and so may drift outside the box while still bound. However, without dramatically increasing the box size, with associated high computational cost, this degeneracy is unavoidable. Therefore, at values of $\alpha_{\rm vir,0} \gtrsim 3$, Equation (13) may underestimate the net star formation efficiency if, in reality, some gas that is expelled from our box were to ultimately recollapse.

4.2.2. Surface Density PDF

In addition to driving outflows, turbulence also has an effect on the gas density structure. In particular, the non-uniformity of the cloud means that it has significant variations in surface density. To quantify this, we calculate the surface densities projected in the x-y, x-z, and y-z planes, and we consider the probability distribution function over all three.

For our fiducial $\alpha_{\rm vir,0} = 2$ model, the resultant surface density distributions by both area $P_A(\Sigma)$ and mass $P_M(\Sigma)$ are shown in Figure 18a,c at t_{10}. By this time, both P_A and P_M are roughly log-normal in shape at high Σ, with similar variances of $\sigma_{\ln\Sigma} \sim 1$. The area distribution has a long tail at low surface density due to the fact that we are sampling over the whole simulation volume rather than just the cloud volume. Meanwhile, as there is little cumulative mass in these low density regions, the mass distribution is much more obviously lognormal, consistent with previous simulations of GMCs with supersonic turbulence (see e.g. Ostriker et al. 2001; Vázquez-Semadeni & García 2001; Federrath et al. 2010).

We may therefore parameterize the "cloud" portion of both $P_A(\Sigma)$ and $P_M(\Sigma)$ as lognormal distributions with mean $\mu_{(A/M)}$ and standard deviation $\sigma_{\ln\Sigma}$:

$$P_{(A/M)}(\Sigma)\ d\ln\Sigma = \frac{1}{\sigma_{\ln\Sigma}\sqrt{2\pi}}\exp\left[-\frac{\left(\ln\Sigma - \mu_{(A/M)}\right)^2}{2\sigma^2_{\ln\Sigma}}\right]\ d\ln\Sigma. \tag{14}$$

At any given time, the total mass in the system is conserved so that $P_M(\Sigma) \propto \Sigma P_A(\Sigma)$. This implies that both distributions must have the same standard deviation and gives a relation between the mean surface density and the means of the two lognormals:

$$\ln\langle\Sigma\rangle_{\rm cloud} = \mu_A + \frac{1}{2}\sigma^2_{\ln\Sigma} = \mu_M - \frac{1}{2}\sigma^2_{\ln\Sigma}. \tag{15}$$

Thus, half of the cloud's mass is at surface densities above/below $\langle\Sigma\rangle_{\rm cloud}\exp(\sigma^2_{\ln\Sigma}/2)$, and half of its area is at surface densities above/below $\langle\Sigma\rangle_{\rm cloud}\exp(-\sigma^2_{\ln\Sigma}/2)$. Here, we emphasize the difference between the mean cloud surface density $\langle\Sigma\rangle_{\rm cloud} \sim M_{\rm cl}/A_{\rm cl}$, which can be obtained using Equation 15 after fitting lognormals to obtain $\mu_{(A/M)}$ and $\sigma_{\ln\Sigma}$, and the mean surface density over the whole simulation volume $\langle\Sigma\rangle_{\rm box} \sim M_{\rm cl}/A_{\rm box}$.

Comparing the fitted lognormal functional form to the PDFs in Figures 18 we see that the lognormal approximation is reasonable, particularly at the high-density end for P_A and around the peak for P_M. The fits we show are only calculated between the $10^{\rm th}$ and $90^{\rm th}$ percentile in mass, so as to avoid sampling the low surface density regions outside the cloud. We also assume measurement errors proportional to $\sqrt{N}$ where N is the number of grid cells in each density bin. At the time shown in Figures 18c, the median or peak surface density of the mass distribution for the fiducial model is around $\Sigma \sim 100$ M$_\odot$ pc^{-2}, but part of the mass lies beyond even $\Sigma \sim 300$ M$_\odot$ pc^{-2}. The peak of the distribution by area shown in Figures 18a is lower, $\Sigma \sim 25$ M$_\odot$ pc^{-2}. As we shall discuss below, the wide variation in Σ implies that at early times, radiation forces can be much more effective in some regions than in others.

The distribution is not just a broad lognormal at the onset of star formation, but remains broad as it progresses. For example, Figures 18b,d show the area and mass PDFs at $t_{50} = 1.06t_{\rm ff,0}$. At this time, the best-fit parameters are $\sigma_{\ln\Sigma} = 1.38$ (where this is taken as the average of fits to the area and mass distributions), $\mu_A = 2.53$, and $\mu_M = 4.45$, so that the mass conservation relations are approximately followed and $\langle\Sigma\rangle_{\rm cloud} \sim 33$ M$_\odot$ pc^{-2}.

In Figures 19a,b, we show the best fit mean and standard deviation parameters as a function of time for lognormal fits to the surface density distribution of our fiducial cloud. A drop in reduced χ^2 values in Figure 19c only really develops after $\sim 0.4t_{\rm ff,0}$ indicating that it is only by this time that turbulence has erased the initial conditions. This is expected, since the cloud is initially uniform and the development of density structure has a timescale set by the turbulent crossing time $t_{\rm cross} = r_0/v_{\rm rms} = 1.2t_{\rm ff,0}$. While the surface density distribution gradually broadens over the first $t_{\rm ff,0}$, after this time it effectively reaches a steady state in both the feedback and no-feedback models, with $\sigma_{\ln\Sigma} \sim 1 - 1.5$. Even though the surface density distributions are visibly different at $t = 1.06t_{\rm ff,0}$ for the feedback (Figure 3) and no-feedback (Figure 15) models, they are statistically similar, since it is only the lower column density regions that are affected by radiative feedback. This holds true until around $1.5t_{\rm ff,0}$, by which time the majority of stars have formed and the majority of remaining gas in the fiducial model is outflowing. As gas is accreted by star particles or is driven from the cloud, the mean and peak of the distribution naturally shift downward. However, the width of the distribution remains similar throughout star formation.

As noted above, we cannot obtain $\langle\Sigma\rangle_{\rm cloud}$ directly from our simulations, since our simulation volume comprises both the "cloud" and the surrounding empty region (or larger scale lower-density ISM in a real system). However, if we assume that the "cloud" portion of the distribution is a lognormal, then we can fit to the PDFs and use Equation 15 to obtain $\langle\Sigma\rangle_{\rm cloud}$. Our fits to obtain μ_A, μ_M, and $\sigma_{\ln\Sigma}$ extend from the 10$^{\rm th}$ to the 90$^{\rm th}$ percentile by mass, which effectively excises the low surface density regions external to the cloud.

We can define the mass-weighted mean surface density over the whole box as $\langle\Sigma\rangle_{\rm M,box} = \langle\Sigma^2\rangle_{\rm box}/\langle\Sigma\rangle_{\rm box}$, where $\langle\Sigma\rangle_{\rm box}$ is the area-weighted mean. Under the assumption that the "cloud" portion is a lognormal, $\langle\Sigma\rangle_{\rm M,cloud} = \langle\Sigma\rangle_{\rm cloud}\exp(\sigma^2_{\ln\Sigma})$, where $\langle\Sigma\rangle_{\rm A,cloud} \equiv \langle\Sigma\rangle_{\rm cloud}$. Figure 20 shows, for the fiducial model, the evolution of the area- and mass-weighted surface densities computed in two different ways: taking direct averages over the box, and using the fitted lognormals to identify just the "cloud" material.

From Figure 20, $\langle\Sigma\rangle_{\rm box}$ starts a factor ~ 5 below $\langle\Sigma\rangle_{\rm cloud}$, because the projected surface area of the cloud is $\sim 1/5$ of the box surface area. Over time, as the cloud disperses and fills more of the simulation area and volume, these measures become more similar. In contrast, $\langle\Sigma\rangle_{\rm M,box}$ and $\langle\Sigma\rangle_{\rm M,cloud}$ are much closer to each other over the whole evolution, and are each an order of magnitude larger than $\langle\Sigma\rangle_{\rm box}$. We conclude that both the definitions $\langle\Sigma\rangle_{\rm A,cloud} \equiv \exp(\mu_M - (1/2)\sigma^2_{\ln\Sigma})$ and $\langle\Sigma\rangle_{\rm M,cloud} \equiv \exp(\mu_M + (1/2)\sigma^2_{\ln\Sigma})$ well represent the area- and mass-weighted mean values for the cloud material, and that the latter is also similar to the mass-weighted mean over the whole box.

We note also that there is no significant change in the width of the surface density distribution with differing initial cloud mass and radius. For a number of different models in our Σ-series, we compute best-fit values of $\sigma_{\ln\Sigma}$ at times t_{10}, t_{50}, and t_{90}, with the results shown in Figure 21a. In most models, there appears to be a modest increase in the lognormal width with time from the width at t_{10}, since this occurs at around $\sim 0.6 t_{\rm ff,0}$, and as discussed earlier, the lognormal has not quite reached a steady state by this stage. However, after $t \sim 1 - 1.2 t_{\rm ff,0}$, the distribution widths remain roughly constant for the remainder of star formation. Moreover, the distribution width is relatively independent of cloud surface density at $\sigma_{\ln\Sigma} \sim 1.3 - 1.5$ (slightly decreasing towards the low-Σ end, which has lower Mach number).

This makes it clear why the simple hypothesis that stars will form until $\langle \Sigma^c \rangle_{\rm cloud} = \Sigma_E$ is seriously flawed: even the peak by mass of the surface density, $\langle \Sigma \rangle_{\rm M,cloud}$, is a factor of $\exp(\sigma^2_{\ln\Sigma}/2) \sim 3.1$ higher than $\langle \Sigma \rangle_{\rm cloud}$. Thus, half of the gas is at surface density more than three times $\langle \Sigma \rangle_{\rm cloud}$, and a large fraction is in regions at even higher surface density. Forcing these high-Σ regions out of the cloud would demand $\Sigma_E \gg \langle \Sigma \rangle_{\rm cloud}$, requiring a higher luminosity and hence (from Equation 10) larger ε than predicted by Equation (12).

In the above, we have analyzed the distribution of surface densities as would be seen by an external observer. However, for the purposes of gauging the effects of radiation forces from a cluster on the surrounding gas in a cloud, what matters is actually the *circumcluster* distribution of densities. As we shall show in a separate publication (Raskutti et al. 2016, in preparation [Paper II]), this distribution is in fact quite similar to the lognormal PDFs shown and discussed above. For example, for the fiducial model, we find $\langle \Sigma^c \rangle_{\rm cloud} \sim 12\ M_\odot\ {\rm pc}^{-2}$ and $\sigma_{\ln\Sigma} = 1.42$ at $t = 1.06\ t_{\rm ff,0}$, which can be compared to the variance and mean values seen by an external observer $\sigma_{\ln\Sigma} = 1.38$ and $\langle \Sigma \rangle_{\rm cloud} \sim 33\ M_\odot\ {\rm pc}^{-2}$ (see also Figure 19 and 20).

The mean value of the cloud surface density at any time is related to its initial mean surface density via the efficiency and a radial contraction factor x (cf. Equation 11), albeit adjusted for the initial turbulent outflows

$$\langle \Sigma^c \rangle = \frac{(1-\varepsilon)}{4x^2} \Sigma_{\rm adj} \tag{16}$$

where $\Sigma_{\rm adj} = \Sigma_{\rm cl,0}(1.0 - \varepsilon_{\rm of,init})$. In addition, fitting a lognormal form gives a value of $\langle \Sigma \rangle_{\rm cloud}$ from Equation 15. Putting these relations together yields x. We shall show in Paper II that for models with $\alpha_{\rm vir,0} \sim 1 - 2$, this yields $x \approx 1$. That is, the overall size of clouds does not vary much over the star-forming period.

4.2.3. Dependence of the PDF on Seed Field

Before we turn to how the surface density field affects the final stellar efficiency, we briefly consider what factors are important in determining its shape. To do this, we run a variation of the fiducial model in which we initially allow our cloud – with the same seed turbulent velocity field – to evolve without self-gravity. Without star formation and feedback, the gas flows steadily out

from the simulation volume due to the initial turbulence, while the Mach number decreases as the turbulence decays and the highest velocity material leaves the box.

However, after half a freefall time, when stars are beginning to form in the fiducial model, the density distribution has reached a rough steady state (as shown from the variance of the column density PDF in Figure 22). From this point forward, the column density distribution remains roughly lognormal, with a fairly steady, though slowly declining width, and a steadily declining mean as the gas flows out of the box. It is also relatively similar to the fiducial model with gravity, suggesting that the initial density field is set almost entirely by the initial turbulence, with gravity only being important on the smallest scales (or highest densities). The only differences are a reduced width, due to the absence of self-gravity, which flattens the distribution at the high density end, and a reduced mean density due to the increased gas outflows. At the onset of star formation, therefore, the bulk of gas mass (i.e., up to the highest densities) has a lognormal shape set almost entirely by the initial turbulent field.

Figure 21b shows the dependence of $\sigma_{\ln\Sigma}$ on the initial virial parameter. Before the majority of star formation begins at t_{10}, the lower $\alpha_{\rm vir,0}$ models have slightly narrower distributions (lower $\sigma_{\ln\Sigma}$) due to their lower Mach number. However, this trend is reversed over time, with the lower virial parameter models tending to have much broader distributions by the end of star formation. Largely this is because these clouds have very high efficiencies, so that only a small fraction of the cloud mass remains once 90% of stars have formed, hence the lognormal fit is considerably worse.

It must also be kept in mind that $\alpha_{\rm vir}$ changes in time for most of the α series. At high initial virial parameter, $\alpha_{\rm vir,0} \gtrsim 5$, the initial turbulence rapidly drives the highest velocity regions from the box, so that the virial parameter rapidly decays. Similarly, at low initial $\alpha_{\rm vir,0}$, including the reduced-turbulence models considered in Section 4.1, the cloud contracts until the virial parameter is close to unity in all cases. This is evident if we consider the variation of $\sigma_{\ln\Sigma}$ with instantaneous rather than initial virial parameter, shown in Figure 23b. Clouds in the range $\alpha_{\rm vir,0} = 0.1 - 3.0$ all converge to a much smaller range of $\alpha_{\rm vir} = 0.5 - 1.0$ by the time star formation begins. Then, as radiative feedback becomes important, $\sigma_{\ln\Sigma}$ increases slightly with increasing virial parameter.

4.3. Final Efficiencies

In this subsection, we present and analyze results for the full set of turbulent cloud collapse models with radiation feedback. In Figure 24 we show the final star formation efficiencies for our Σ- and α-series cloud models. We have normalized by both the initial cloud mass and the cloud mass corrected for turbulence driven outflows. Interestingly, the efficiency appears to show a logarithmic dependence on Σ across almost two orders of magnitude of variation in the initial surface density. In fact, Figure 24 shows a remarkably good fit to the relation $\varepsilon = 0.37\log\Sigma - 0.26$ (black line). This is true even if we account for the mass loss due to turbulent outflows from the simulation box by setting $\varepsilon \rightarrow \varepsilon_{\rm adj} \equiv \varepsilon/(1.0 - \varepsilon_{\rm of,init})$. The normalization of the relation changes slightly,

but we still obtain a logarithmic relationship between surface density and final efficiency, given by $\varepsilon = 0.41\log\Sigma - 0.26$ (red line).

We can also fit to a logarithmic dependence on the virial parameter, with $\varepsilon = -0.45\log\alpha + 0.51$, although in this case it is less clear whether this is significant, as there are systematic errors at both low and high virial parameter. Moreover, our estimate of the net efficiency is uncertain at high virial parameter, since we overestimate turbulent outflows and correspondingly underestimate star formation.

Although the logarithmic form fits the Σ series well, it is quite different from simple predictions. For example, we can compare the numerical results to the uniform shell force balance model (with $x = 1$) of Equation (12), as shown with the red solid line in Figure 25. Evidently, both the shape and magnitude of the curve from Equation (12) compare poorly with the simulation results.

As discussed earlier, the key difference between the simulated clouds and the simple Eddington limit prediction of Equation (12) is that the cloud does not have uniform surface density. Stars do not keep forming inside a uniform shell and then instantaneously drive that shell away once the efficiency ε and luminosity are large enough for Σ_E to match $\langle\Sigma^c\rangle_{\rm cloud}$. Instead, as will be discussed in more detail in Raskutti et al. (2016), early star formation begins to drive away the lowest surface density regions (those that have have $\Sigma^c < \Sigma_E$). Stars continue forming from the remaining mass until the radiative force is sufficient to drive away much higher surface density gas (as, from Equation 10, an increase in ε raises Σ_E). For example, in our fiducial model, close to the end of star formation at $t = 1.45t_{\rm ff,0}$ when $\varepsilon \sim 0.35$, the mean surface density is $\langle\Sigma\rangle_{\rm cloud} \sim 12\ M_\odot\ {\rm pc}^{-2}$, with the circumcluster surface density around a factor of 2 or 3 lower again, while the Eddington surface density in Equation (10) is $\Sigma_E \sim 200\ M_\odot\ {\rm pc}^{-2}$, implying that enough stars have formed to drive away gas at close to 50 times the mean surface density of the cloud. Figure 19 shows that at this time $\sigma_{\ln\Sigma} = 1.49$ which yields $\mu_M = 2.9$ such that $\ln\Sigma_E = 5.3$ is roughly 1.5-σ above the peak surface density. This would suggest that star formation is halted when enough stars form to drive away not the mean surface density, but instead something closer to the $90^{\rm th}$ percentile of surface density.

Recently, Thompson & Krumholz (2016) have argued that understanding how radiative feedback limits star formation in GMCs requires an accounting of the full surface density distribution set by turbulence. They propose a model in which the instantaneous mass loss rate from a cloud is set by the cloud's freefall time and fraction of mass in a lognormal PDF at surface densities below a critical value. At the same time, they assume the stellar mass and luminosity increases as $\dot{M}_* = \varepsilon_{\rm ff} M_{\rm gas}/t_{\rm ff}$. Here, we develop a related model by considering the mass eligible to be expelled from the cloud at any time, for a given lognormal PDF and star formation efficiency.

From Equation (10), surface densities above the Eddington surface density Σ_E have a net inward force and can continue to either collapse and form stars, or be accreted on to the growing star clusters. Correspondingly, surface densities below Σ_E have a net outward force, and we assume here that such regions become instantaneously unbound without further mixing with other gas.

Although this is clearly an oversimplification, we have found (see Raskutti et al. 2016, for details) that the distribution of outflowing velocities is consistent with essentially ballistic outflow of super-Eddington structures.

If the cloud has a circumcluster surface density distribution $P_M(\Sigma^c)$ by mass, the fraction of mass eligible to be expelled will be $\int_{-\infty}^{\ln\Sigma_E} P_M(\Sigma^c) d\ln\Sigma^c$. If the stellar mass in the cloud at a given instant during its evolution is $M_* = \varepsilon M_{\rm cl,0}$, then the gas mass remaining is $(1-\varepsilon)M_{\rm cl,0}$, and the fraction $\varepsilon_{\rm of}$ of the original gas that is eligible for outflow is:

$$\varepsilon_{\rm of} = (1-\varepsilon)\int_{-\infty}^{\ln\Sigma_E} P_M(\Sigma^c) d\ln\Sigma^c. \tag{17}$$

In Section 4.2.2, we showed that the column density distribution is well approximated by a lognormal distribution, and here, we extend that approximation to the circumcluster surface density (see Raskutti et al. 2016, for details). In this case, Equation (17) may be evaluated as

$$\varepsilon_{\rm of} = \frac{1}{2}(1-\varepsilon)\left(1+{\rm erf}\left(y_E\right)\right), \tag{18}$$

where

$$y_E \equiv \frac{\ln\Sigma_E - \mu_M}{\sqrt{2}\sigma_{\ln\Sigma}}. \tag{19}$$

The quantity $\mu_M = \ln\langle\Sigma^c\rangle + \sigma^2_{\ln\Sigma}/2$ (see Equation 15) is the mean of the mass distribution of $\ln\Sigma^c$ and $\sigma_{\ln\Sigma}$ is the variance. Using Equation (11),

$$\mu_M = \ln\left[\Sigma_{\rm cl,0}(1-\varepsilon)\right] + \frac{\sigma^2_{\ln\Sigma}}{2} - \ln(4x^2) \tag{20}$$

if the circumcluster gas is concentrated in a thin shell. Substituting into Equation (19) and using Equation (10), we obtain:

$$\begin{aligned} y_E &= \frac{1}{\sqrt{2}\sigma_{\ln\Sigma}}\ln\left(\frac{4\Sigma_E x^2}{\Sigma_{\rm cl,0}(1-\varepsilon)}\right) - \frac{\sigma_{\ln\Sigma}}{\sqrt{8}} \\ &= \frac{1}{\sqrt{2}\sigma_{\ln\Sigma}}\left[\ln\left[\frac{2\Psi}{\pi c G\Sigma_{\rm cl,0}}\right] + 2\ln x - \frac{\sigma^2_{\ln\Sigma}}{2} + \ln\frac{\varepsilon}{1-\varepsilon^2}\right]. \end{aligned} \tag{21}$$

With Equation (21), Equation (18) gives the unbound or outflowing fraction $\varepsilon_{\rm of}$ of a cloud with initial surface density $\Sigma_{\rm cl,0} \equiv M_{\rm cl,0}/(\pi r^2_{\rm cl,0})$ in terms of the current efficiency ε and the two free parameters x and $\sigma_{\ln\Sigma}$.

Figure 26 shows the behaviour of $\varepsilon_{\rm of}$ as a function of input stellar efficiency ε for varying $\Sigma_{\rm cl,0}$ and $\sigma_{\ln\Sigma}$. When $\varepsilon = 0$, $\varepsilon_{\rm of} = 0$ since with no stars, the Eddington surface density is zero. As the mass in stars increases, $\varepsilon_{\rm of}$ initially also increases under two competing influences. More stars increase the radiative force and Σ_E so that a larger fraction of the cloud is eligible to become unbound; this increases the factor $1 + {\rm erf}(y_E)$ in Equation (18). However, a larger stellar mass also decreases the gas mass since a larger fraction of the cloud is already bound up in stars; this

decreases the factor $1-\varepsilon$. In the limit $\varepsilon \to 1$, there is no gas reservoir and therefore $\varepsilon_{\rm of} \to 0$. For some value intermediate value of ε between 0 and 1, an infinitesimal increase in ε would decrease $\varepsilon_{\rm of}$ in Equation 18, since the overall decrease in the gas mass reservoir (lower $1-\varepsilon$) outweighs the increase in the fraction of gas that is super-Eddington (higher y_E). This point represents the maximum value of $\varepsilon_{\rm of}$ for any given set of initial cloud parameters and variance in the PDF.

We consider a cloud such that, for a given PDF variance, the maximum in $\varepsilon_{\rm of}$ has been reached; its efficiency is then $\varepsilon = \arg\max \varepsilon_{\rm of}$. At this point, the outflowing gas mass cannot decrease, because this material has already become super-Eddington. The remaining gas reservoir that is neither stars nor outflowing gas is a fraction $(1 - \max \varepsilon_{\rm of} - \arg\max \varepsilon_{\rm of})$ of the original cloud. If this material collapses faster than the PDF in larger-scale cloud can adjust, it will all be added to the existing stars and the final star formation efficiency will be $\varepsilon_{\rm final} = 1 - \max \varepsilon_{\rm of}$. The luminosity from these additional stars would also increase the radiation pressure on the outflowing gas. Alternatively, if the collapse is slower, there may be time for the log-normal density distribution of the remaining gas to adjust, and the final star formation efficiency may rise to a level between $\arg\max \varepsilon_{\rm of}$ and $1 - \max \varepsilon_{\rm of}$. This suggests that for a given PDF variance, there are upper and lower bounds on $\varepsilon_{\rm final}$:

$$\begin{aligned} \varepsilon_{\rm max} &= (1 - \max_{0<\varepsilon<1} \varepsilon_{\rm of}) \\ &= \frac{1}{2} \min_{0<\varepsilon<1} \left[1 + \varepsilon + (\varepsilon - 1){\rm erf}\left(y_E\right)\right] \qquad (22a) \\ \varepsilon_{\rm min} &= \arg\max_{0<\varepsilon<1} \varepsilon_{\rm of}. \qquad (22b) \end{aligned}$$

From Figure 26, the maximum of the function $\varepsilon_{\rm of}$ increases with decreasing $\Sigma_{\rm cl,0}$, since at lower surface densities the gas reservoir can be driven away more easily. Also, broader surface density distributions (larger $\sigma_{\ln\Sigma}$) tend to decrease $\max \varepsilon_{\rm of}$ since more gas is at the highest density, which is more difficult to unbind.

In Figure 25, we compare the predictions of Equation (22) to our numerical results for net star formation efficiencies as a function of initial surface density. We note that we are primarily interested in the efficiency relative to the cloud mass adjusted for initial turbulent outflows $\varepsilon_{\rm adj} = \varepsilon/(1-\varepsilon_{\rm of,init})$, so we substitute the adjusted surface density $\Sigma_{\rm cl,0} \to \Sigma_{\rm adj} = \Sigma_{\rm cl,0}(1-\varepsilon_{\rm of,init})$ in Equation (21). For the parameters entering Equation (21), we use $x = 0.84$ and $\sigma_{\ln\Sigma} = 1.42$, based on the time average of the best-fit values for the circumcluster surface density in the fiducial model (see Paper II for details). We use these same values of x and $\sigma_{\ln\Sigma}$ at all $\Sigma_{\rm cl,0}$. Additionally, since we are interested in comparing to the physical observed cloud, rather than the artificial initial conditions, we show the adjusted efficiency as a function of the adjusted cloud surface density $\langle\Sigma_{\rm cloud}\rangle = \Sigma_{\rm adj}/x^2$ rather than $\Sigma_{\rm cl,0}$.

Figure 25 shows that $\varepsilon_{\rm max}$ from Equation (22a) represents a reasonable estimate of the actual SFE found in the simulations, both in normalization and in the shape of the dependence on $\Sigma_{\rm cloud}$. In principle, however, the final efficiency might be closer to $\varepsilon_{\rm min}$ if conditions were such that the star formation rate were lower.

Equation (22) predicts much higher efficiencies than the fiducial model of Thompson & Krumholz (2016), shown for comparison in Figure 25. Their model has similar ingredients to ours (a lognormal surface density distribution, with both sub-Eddington and super-Eddington regions), with the principal difference being that the Thompson & Krumholz (2016) formalism assumes a fixed star formation rate per unit gas mass, whereas there is no assumption about the star formation rate in our model. Specifically, they assume that stars form at a rate $\dot{M}_* = \varepsilon_{\rm ff} M_g / t_{\rm ff}$ from the total remaining mass (including super-Eddington $\Sigma < \Sigma_E$ regions), and that winds are driven out at a rate proportional to $1/t_{\rm ff}$ from the super-Eddington gas. It is their adoption of a very small fiducial value $\varepsilon_{\rm ff} = 0.01$ (implying a vast discrepancy between star formation and wind expulsion rates) that leads to a highly suppressed final efficiency in their fiducial model. If instead we adopt $\varepsilon_{\rm ff} = 0.44$ (similar to our simulation results in Section 4.6) and apply their formula, their model prediction is somewhat closer to ours, albeit with a lower normalization and shallower dependence on $\Sigma_{\rm cloud}$ (see Figure 25).

The correspondence between the prediction of $\varepsilon_{\rm max}$ in Equation (22a) and our $\Sigma-$series numerical model results is close enough to suggest that the dominant effect in suppressing star formation is radiative feedback driving out structures at successively higher surface densities until a maximum mass of outflowing material is reached. However, there are a number of issues, or at least questions, surrounding this model. First among these is whether the correlation timescale of the lognormal surface density distribution in the cloud is long enough to allow persistent acceleration by the central stars. This is because the dynamical evolution of any given fluid element depends on the coherence time of the (Lagrangian) evolution for the surface density region surrounding it. In principle, the surface density distribution could remain statistically lognormal at all times, while individual regions fluctuate rapidly. If these fluctuations in time are much shorter than the time taken for radiation to accelerate gas from the cloud, then any fluid element would fully sample the distribution of surface densities, and only the mean cloud surface density would be relevant.

The question of the column density correlation timescales in comparison to the cloud destruction timescale has already been discussed in a heuristic manner in Thompson & Krumholz (2016). They compare the turbulence crossing time to the acceleration timescale $t_{\rm acc} \propto r_0 / v_{\rm esc}(r_0)$ and argue that so long as the radiation force is several times stronger than the force of gravity, densities will fluctuate on longer timescales than it takes for the cloud to unbind.

In our simulations, we can measure the temporal correlations of the column in a given area of the sky. We find a correlation time $\sim 0.5 t_{\rm ff,0}$ once star formation has begun. This is roughly comparable to the timescales on which gas is accelerated out of the cloud, suggesting that outflowing low surface density regions might merge with collapsing higher surface density regions before they have a chance to escape the cloud. However, this overall Eulerian correlation time is not necessarily representative for low density regions. In addition, we do find an outflowing velocity distribution consistent with low density regions remaining correlated until they escape the cloud (see Raskutti et al. 2016, for details) and so conclude that this interpretation is not unreasonable. In future tests, to answer this question realistically, we would need to use tracer particles in the gas to track the

flow of individual fluid elements.

We note also that the values of $\sigma_{\ln\Sigma}$ from our simulations (see Figures 21 and 23) are somewhat larger than current estimates from observations, which typically find $\sigma_{\ln\Sigma} < 1$. This may owe in part to line-of-sight contamination, which tends to reduce the observed $\sigma_{\ln\Sigma}$ (e.g., Schneider et al. 2015), and in part to the absence of magnetic fields in the present models, as magnetization reduces shock compression and therefore density variance (e.g., Ostriker et al. 2001; Molina et al. 2012). Figure 27a shows the prediction of Equation (22a) for $\varepsilon_{\rm final}$ as a function of $\Sigma_{\rm cl}$ for a range of $\sigma_{\ln\Sigma}$, demonstrating that the predicted net SFE in a cloud could be considerably lower at low $\sigma_{\ln\Sigma}$.

4.4. Effect of varying Ψ

As a final point, it is worth considering the effects on our model of a varying Ψ due to undersampling of the IMF. Kim et al. (2016) recently studied the effects of an undersampled Chabrier (2003) IMF on the value of Ψ, both stochastically and on average, by using the SLUG code (Krumholz et al. 2015) to simulate the photon output from stellar clusters as a function of mass. They found that although 100 $M_\odot$ clusters produce significantly fewer photons, with $\Psi \sim 200$ erg s^{-1} g^{-1}, by the time $M_\star \sim 2 \times 10^3$ $M_\odot$, the cluster luminosity per unit mass has settled to the final fully sampled value of $\Psi \sim 2000$ erg s^{-1} g^{-1}, with a variation of around ± 0.3 dex around this median. For even larger clusters of $M_\star \sim 10^4$ $M_\odot$, this variance drops to only ± 0.1 dex. We may therefore expect the stellar IMF to be fully sampled for $M_\star \gtrsim 2 \times 10^3$ $M_\odot$.

In all of our simulations, the stellar mass exceeds 2×10^3 $M_\odot$ by the end of the star formation epoch. Our lowest mass cloud has a mass of only 5×10^3 $M_\odot$ but an efficiency of more than 40%, so that more than 2×10^3 $M_\odot$ is in stars. When star particles first form, realistically the IMF would be undersampled. By setting Ψ to a constant, we overestimate the radiative force at early times, while correspondingly underestimating the star formation rate. However, the final efficiencies are largely set by the balance between the radiative force and the gas self-gravity at late times, so these are not changed significantly by our overestimation of Ψ at early times.

The smallest of our star particles are less than $M_\star \sim 10^2$ $M_\odot$, which would imply correspondingly low median values of $\Psi \sim 200$ erg s^{-1} g^{-1}. Therefore, when these star particles first form, we are overestimating the radiative force by a factor of almost 10. We may bracket the effect of this by simulating our fiducial model over a range of possible Ψ values. In Figure 28 we show the stellar efficiency for three different models with Ψ varying between 200 and 2000 erg s^{-1} g^{-1}. The models with lower Ψ form stars at a slightly faster rate and end up with a higher efficiency, since less gas is driven from the cloud by the effects of UV radiation.

However, we note that the variation in efficiency is only ~ 50 % despite an order of magnitude variation in the luminosity per unit mass. In simple models of radiative feedback that assume a uniform shell of gas driven away by radiative pressure, $1/\varepsilon - \varepsilon$ is linear with Ψ. Therefore, variation by an order of magnitude in Ψ would correspond to almost an order of magnitude variation in ε,

or at least a saturation at unity. By contrast, the model we develop, which takes into account the lognormal surface density distribution with best-fit values of x and $\sigma_{\ln\Sigma}$, does a much better job of matching the final stellar efficiency, as shown in Figure 27b.

The above shows that the final SFE is much less sensitive to undersampling of the IMF than simple models would predict. More importantly, by the time star formation stops, all of our clouds, even the lowest mass ones, have enough stellar mass to sample the IMF. Furthermore, the gas surface density structure of our clouds does not change significantly for varying Ψ, since it is largely set by the initial turbulence. Therefore, by the time the IMF becomes fully sampled, the cloud appears roughly the same regardless of the strength of radiative feedback prior to that time. We might then expect the final efficiency to only depend on the final value of Ψ, which is $\Psi \sim 2000$ erg s^{-1} g^{-1} in all cases. In fact, when we run simulations in which the value of Ψ changes from $\Psi \sim 200$ erg s^{-1} g^{-1} at early times to $\Psi \sim 2000$ erg s^{-1} g^{-1} after a freefall time, as shown in Figure 28, the final stellar efficiency is largely unchanged.

4.5. Evolution of Star Formation Rate

So far, we have only been considering the final efficiencies of star forming clouds as a means of assessing when radiative feedback becomes important in unbinding GMCs. However, of just as much interest is the rate of star formation, which is often parameterized by the star formation rate per freefall time:

$$\dot{M}_*(t) \equiv \varepsilon_{\rm ff}(t)\frac{M_g(t)}{t_{\rm ff}(t)}. \tag{23}$$

We now turn to an analysis of how this star formation rate varies in our models.

The majority of previous studies have tended to focus only on the mean SFR per freefall time $\langle\varepsilon_{\rm ff}(t)\rangle$ averaged over the whole epoch of star formation and with a fixed $t_{\rm ff} = t_{\rm ff,0}$ set by the cloud's initial mean density (e.g., Wang et al. 2010; Padoan & Nordlund 2011; Padoan et al. 2012; Bate 2012; Krumholz et al. 2012; Federrath & Klessen 2012; Myers et al. 2014). Here, we adopt the methodology of Lee et al. (2015) and fit the stellar mass history of our clouds to determine if there is any systematic evolution in time. We fit with a power law defined in terms of $t - t_*$, where t_* is the time at which the first star particle is formed. We also initially tested the fitting region of Lee et al. (2015) ranging from $M_* = 0.015M_{\rm cl,0}$ to $M_* = 0.3M_{\rm cl,0}$. Adopting this choice for our fiducial model, similar to Lee et al. (2015) we can confirm a super-linear, though slightly less than quadratic power-law evolution of the star formation efficiency, $M_* \propto t^\beta$ with $\beta \sim 1.5$, as shown in Figure 29.

However, there are a number of issues with fitting a power law to the SFR. Firstly, there is no reason a priori to assume that the gas density distribution or the SFR have reached some sort of steady state at t_*. This is certainly a concern for our simulations, since the cloud begins with uniform density, which is very far from a self-consistent quasi-steady state. It will undergo

turbulent collapse, and the highest density regions may form stars while the shape of the density distribution is still changing considerably. Therefore, a power law starting at t_* will not necessarily capture the physics of star formation in realistic clouds as it may still be affected by the artificial initial conditions.

This can be seen very clearly if we consider the stellar mass evolution in our fiducial model as a function of $t - t_*$, as shown in Figure 29. There is an obvious break in the power law at around $M_* \approx 0.1 M_{\rm cl,0}$ so that a single power law underestimates the stellar mass at both early and late times. This break is not the result of feedback; the model without radiative feedback also shows a similiar break, and an almost identical evolution up to at least $\sim 0.3 M_{\rm cl,0}$.

A much better fit can be achieved if we allow for a broken power law $M_* \propto (t - t_{\rm break})^{\beta}$, with a transition time $t_{\rm break}$. For the fiducial model, $t_{\rm break}/t_{\rm ff,0} = 0.80$ when $M_*/M_{\rm cl,0} = 0.094$. In this case, as shown in Figure 30b, we have a much smaller least squares error for the broken power law model ($\chi^2_{\rm broken}$) as opposed to the simple power law ($\chi^2_{\rm pl}$) with $\chi^2_{\rm broken}/\chi^2_{\rm pl} = 0.042$ over the whole fitting range and $\chi^2_{\rm broken}/\chi^2_{\rm pl} = 0.24$ just above the break mass. More importantly, the broken power law does not systematically depart from the evolution at either low or high stellar mass, and thus more accurately captures the cloud behaviour below the transition.

Interestingly, when we fit to a broken power-law, both regimes show roughly linear growth in the stellar mass with time, albeit at significantly different rates. In fact, if we restrict both regimes to have a constant star formation rate (as shown in Figure 30c) we still get a much better fit than the simple power law above the break time, with $\chi^2_{\rm lin}/\chi^2_{\rm pl} = 0.38$. This suggests two things. Firstly, our fiducial cloud simulation exhibits some transient behaviour even after star formation has begun; until close to a freefall time it seems to be adjusting from the artificial initial state. Secondly, the cloud appears to emerge from this transient state at approximately t_{10}. It then exhibits roughly linear growth in stellar mass until radiative feedback becomes important.

We may test the presence of this transient state by considering a "pre-relaxed" model, in which the cloud is allowed to evolve without self-gravity for the first half of a freefall time and then evolves with gravity beyond this point. When this is done, the stellar and outflowing mass evolve as shown in Figure 31. We see that the pre-relaxed model has both a lower final efficiency and lower SFR. It is however difficult to compare this result to our fiducial model, since it is at lower surface density due to both expansion of the cloud and the much larger fraction of gas unbound by the initial turbulence (around 30 % compared to 10 %). Moreover, it is at a lower virial parameter since the turbulence decays away over the first half a freefall time of relaxation. What we can see is that there is no evidence of a break in the SFR for this model, suggesting that this break is an artificial one born of our initial conditions.

The origin of a constant SFR in later stages is not trivial to explain. The simplest star formation law, and one assumed in a number of previous studies, adopts the form

$$\dot{M}_*(t) = \varepsilon_{\rm ff} \frac{M_g(t)}{t_{\rm ff}(t)}, \tag{24}$$

where $\varepsilon_{\rm ff}$ is a constant and $t_{\rm ff} \propto \rho_g^{-1/2}$ is the instantaneous freefall time for $\rho_g(t)$ the (time-dependent) volume-averaged gas density. A focus of both numerical and observational studies has been to fit to this form and estimate $\varepsilon_{\rm ff}$. In this picture, star formation halts through a combination of gas depletion by star formation and gas expulsion through cloud expansion and a subsequent increase in $t_{\rm ff}$. However, the form of Equation (24) does not seem to apply in our simulations. In our turbulent clouds, the cloud radius remains roughly constant while the majority of stars are forming so that $\rho_g \propto M_g$ and $t_{\rm ff} \propto M_g^{-1/2}$, which would yield $\dot{M}_* \propto M_g^{3/2}$ in Equation (24). Therefore, as the gas mass is depleted, Equation (24) would predict a decrease in the SFR until cloud expansion from feedback drives a rapid increase in the freefall time. In fact, our power law or broken power law fits show that the SFR is constant or increasing until gas is expelled by feedback.

Fits to the simple star formation law of Equation (24) are shown in Figure 30d. The gas mass $M_g(t)$ is taken directly from each simulation, and $t_{\rm ff}(t)$ is found by fitting for the mean cloud density through the density PDF. If we fit this form with star formation beginning at $t = t_*$, the best-fit value is $\varepsilon_{\rm ff} = 0.45$, and there is a huge discrepancy between the numerical and analytic results. Even if we fit only after $t = t_{\rm break}$, the fit is not good; the best-fit efficiency $\varepsilon_{\rm ff} = 1.21$ is high since the early mass growth must be large to compensate for the steady decrease in SFR.

We may test the generality of these conclusions by applying the same methodology to other members of our Σ-series simulations. As a caveat, we saw in Section 3.2 that lower resolution simulations will capture the final SFE, but may underestimate the SFR if they are not converged. This is particularly evident in our low surface density and high virial parameter simulations in which the number of individual star particles formed is small. With this in mind, we omit simulations with $\varepsilon < 0.15$ or $\Sigma_{\rm cl,0} < 20\ M_\odot\ {\rm pc}^{-2}$ from our studies of the SFR.

In Figure 32 we show the best-fit characteristics for both the single power-law fit and the high mass portion of our broken power-law fit, as a function of surface density. For the Σ-series, we observe little variation in either the power law exponent or the break time and mass across the sequence. As for our fiducial model, for the broken power law, the fitted exponent is close to $\beta = 1$ for most cases. Meanwhile, a single power law almost always shows super-linear behavior, with $\beta \sim 1.5$.

At the break time, roughly 0.1 $M_{\rm cl,0}$ in stellar mass has formed across all models. The break times also show little variation with surface density, being close to $t_{\rm break} \sim 0.8 t_{\rm ff,0}$ for the broken power law, with $t_* \sim 0.5 t_{\rm ff,0}$. The most massive clouds begin star formation a little earlier, since they are already denser, hence regions reach critical densities high enough to undergo local collapse at earlier times. This slight surface density dependence also persists in the break time for the broken power law, suggesting that it may be as arbitrary as t_*. Potentially, the initial conditions still affect the state of the system at $t_{\rm break}$, although our simulations do not show any strong evidence for a continuous acceleration in the star formation rate. Nevertheless, simulations with more realistic cloud initial conditions are needed before any definitive statements can be made about varying star formation rates in turbulent clouds.

4.6. Star Formation Per Freefall Time

The fact that our star formation efficiencies grow roughly linearly with time allows us to quantify these star formation rates quite easily. We replicate the method of Padoan & Nordlund (2011); Krumholz et al. (2012); Myers et al. (2014) and fit a straight line to the stellar mass vs. time above the transition mass discussed in Section 4.5. We then calculate the efficiency per freefall time defined as

$$\varepsilon_{\mathrm{ff},\bar{\rho}} \equiv \frac{\langle \dot{M}_* \rangle t_{\mathrm{ff},\bar{\rho}}}{M_{\mathrm{cl},0}} \tag{25}$$

where the mean density used in $t_{\mathrm{ff},\bar{\rho}}$ is calculated from directly fitting a lognormal form to the density PDF at the start of star formation, defined here as t_{break}, and extracting the mean density $\langle \rho \rangle$. For the Σ-series, this is very close to the initial cloud density since only around 10% of the mass is lost in early turbulent outflows and there is very little global cloud contraction or expansion. However, the mean density differs significantly from the initial cloud value for the models with low virial parameter, where the cloud contracts significantly.

In Figure 33 we show the resulting star formation rate coefficients as a function of both surface density and virial parameter. Almost irrespective of both virial parameter and surface density, we find a rate coefficient $\varepsilon_{\mathrm{ff},\bar{\rho}} \sim 0.25 - 0.5$. Notably, the inclusion of radiative feedback only mildly decreases the star formation rate, with no systematic surface density dependence. This is not surprising as we had already noted that turbulence dominates the star formation at early times. These results again suggest that UV feedback in clouds can be effective as a means of limiting star formation and unbinding clouds, but does little to suppress the instantaneous star formation rate.

4.7. Cloud Lifetimes

The consequence of such high star formation rates is that our model clouds either convert most of their gas mass to stars, or become unbound on short timescales. While it is difficult to characterize exactly when the bulk of gas mass from a filamentary cloud becomes unbound, the proxy we use is the virial parameter. Similar to Colín et al. (2013), we find that in all our Σ-series simulations, the virial parameter remains close to unity when the dynamics are set by gravitational collapse and turbulence, but then quickly expand to $\alpha_{\mathrm{vir}} \sim 50$ once radiative feedback begins to dominate. Therefore, we arbitrarily take $\alpha_{\mathrm{vir}} = 5$ as our criterion for unboundedness, noting that the expansion from being formally unbound at $\alpha_{\mathrm{vir}} = 2$ to $\alpha_{\mathrm{vir}} \gtrsim 10$ takes $\sim 0.3 t_{\mathrm{ff},0}$.

In Figure 34a, we show the time t_{unb} when clouds become unbound ($\alpha_{\mathrm{vir}} = 5$) as a function of surface density. We find that clouds last between 1.2 and 1.9 $t_{\mathrm{ff},0}$ at most and that radiative feedback acts very rapidly to unbind the clouds, with the transition from $\alpha_{\mathrm{vir}} = 2$ to $\alpha_{\mathrm{vir}} = 10$ never taking longer than half a freefall time. Star formation still continues slowly as clouds continue to expand beyond $\alpha_{\mathrm{vir}} = 5$, but if we look at the time t_{80} as shown in Figure 34a, it is generally similar to t_{unb}, while t_{90} roughly corresponds to clouds reaching a virial parameter of ~ 10.

Given that the first stars only begin forming at around $\sim 0.5 t_{\rm ff,0}$, and clouds only reach a state where the artificial initial conditions are erased at $\sim 0.8 t_{\rm ff,0}$ (where this number is taken from both the minimum in the virial parameter, and the break times in fits to the SFR), this means that the majority of clouds form stars over a period shorter than a global freefall time.

This can be seen if we consider the cloud star-forming time, defined as $t_{\rm unb} - t_*$, in Figure 34b. Since $\varepsilon_{{\rm ff},\bar{\rho}}$ varies mildly but $\varepsilon_{\rm final}$ increases more strongly with Σ, there is an increase in cloud lifetime in units of $t_{\rm ff,0}$ with Σ, as the more massive clouds will convert more of their gas to stars before the effects of radiative feedback dominate and, additionally, begin forming stars at a slightly earlier time. However, as high-Σ clouds also have much shorter freefall times, we find that, generically, cloud star formation times ($t_{\rm unb} - t_*$ or $t_{90} - t_*$) are between 2 and 8 Myr (see Figure 34c), with more massive clouds being slightly shorter-lived than their low surface density counterparts. Since SN feedback can only act more than 3 Myr after $\sim t_*$, it seems likely that if there were no other source of star formation suppression, direct radiation pressure would be able to disperse clouds across a wide range of surface densities before SNe begin to impact cloud dynamics. However, this cloud dispersal would be at the expense of a larger net star formation efficiency than inferred from observations in many Milky Way clouds.

This apparent conflict with observation may potentially be explained in several ways. One possibility is that GMCs are strongly affected by additional sources of internal feedback not modeled here (such as ionizing radiation[1]) or external feedback (including supernova blast waves from stars formed in other GMCs). Another is that GMCs may have effective virial parameters exceeding 2, e.g., if the outer parts are still condensing even as the inner parts begin vigorous star formation.

5. Summary and Discussion

We have carried out three-dimensional RHD simulations of internal gravitational collapse, star formation, and destruction of turbulent models of GMCs. Our models consider a range of masses, radii, and initial virial parameters representative of observed Milky Way GMCs, with initial surface densities in the range 10 - 300 $M_\odot$ pc^{-2}. Each cloud is initialized with power-law turbulence and simulated in a computational domain twice the initial cloud diameter, adopting an isothermal equation of state for the gas. Sink particles (representing star clusters) formed via gravitational collapse become sources of radiation, with a constant luminosity-to-mass ratio $\Psi = 2000$ erg s^{-1} g^{-1}. We follow each cloud for four (initial) freefall times, until all the gas mass is either in stars or has been expelled from the box. Cloud destruction is a consequence of the direct radiation forces applied to the gas and the relatively high opacity $\kappa = 1000$ cm^2 g^{-1}, appropriate for non-ionizing UV. We incorporate the effects of radiation, from sink/star particles but not re-emitted

[1] High-pressure ionized gas can drive expansion of the surrounding neutral gas and can itself directly escape the cloud from "blister" HII regions if the potential well is not too deep.

IR, using *Hyperion*, which provides time-dependent solutions for the radiation energy density and flux. Our main goal is to investigate the effect that radiation forces from distributed stellar sources have on the SFE and SFR of turbulent, star-forming clouds.

The clouds in our simulations follow similar evolutionary tracks. Initially, there is a period of structure formation and fragmentation driven by turbulent compression and self-gravity. For clouds with initial $\alpha_{\rm vir,0} = 2$, by $t \sim 0.6 t_{\rm ff,0}$ this creates a filamentary gas distribution in which $\sim 10\%$ of the cloud mass has collapsed to form stars, and a similar fraction has become unbound by the initial turbulence. This is followed by a period of rapid star formation and a transition to cloud expansion driven by radiative feedback. Star formation proceeds but at a slower rate, and it is largely complete by $\sim 2 t_{\rm ff,0}$.

All of our clouds share a number of common features in their gas density distributions, and show similar SFR scalings and coefficients. However, the SFE over a cloud's lifetime depends sensitively on a cloud's mean surface density and initial virial parameter. For virialized, turbulent clouds, we show that limits exist on the SFE, when it is interpreted in terms of a localized, sequential competition between gravity and secularly increasing radiation forces in a cloud with a lognormal distribution of surface densities.

Below, we summarize the similarities and differences among our models, as well as our key conclusions regarding the roles of radiation feedback in controlling star formation and GMC evolution.

1. *Surface Density Distribution*

   After an initial transient phase (lasting $\sim 0.4 t_{\rm ff,0}$ for our fiducial model), the surface densities in our model clouds approach lognormal distributions. The variances $\sigma^2_{\ln \Sigma}$ in the PDFs of mass and area as a function of $\ln \Sigma$ are similar, consistent with expectations for a lognormal distribution. Meanwhile, the means (PDF peaks) are close to the predicted $\mu_M = \mu_A + \sigma^2_{\ln \Sigma}$, where μ_A and μ_M are, respectively, the area- and mass-weighted means of $\ln \Sigma$. The mean value of the gas surface density and PDF peaks slowly decrease over time as gas is accreted onto star particles and expelled from the cloud by radiation forces, while the width of the PDF only slightly increases. After $t \sim t_{\rm ff,0}$, by which time star formation is already well underway, $\sigma_{\ln \Sigma}$ begins to decrease after the radiation field becomes strong enough to disperse low-density gas (see, e.g., Fig. 19b). For all of our models, which have initial Mach number between 10 and 40 and initial virial parameter between 0.1 and 10, the width of the PDF ranges only over $\sigma_{\ln \Sigma} \sim 1 - 2$, with $\sigma_{\ln \Sigma} \sim 1 - 1.5$ for the Σ series (see Fig. 21).

   The lognormal distributions of surface density found in our simulations are generally consistent with observations of a range of GMCs, which also show power-law tails at high column densities associated with star-forming regions (e.g., Goodman et al. 2009; Kainulainen et al. 2009; Lombardi et al. 2010, 2015; Schneider et al. 2013, 2015). Our simulations do not show the emergence of a clear power-law tail in the PDF as star formation progresses (cf. Klessen et al. 2000; Vázquez-Semadeni et al. 2008; Federrath et al. 2008; Kritsuk et al. 2011; Collins

et al. 2012; Federrath & Klessen 2013; Lee et al. 2015), likely because our global cloud models lack resolution at the highest densities. The measured values of $\sigma_{\ln\Sigma}$ are somewhat larger in our simulations than in nearby well-studied clouds (Schneider et al. 2015), although more massive, more turbulent GMCs are likely to have broader PDFs.

The stationary lognormal form of the surface density PDF during the main star formation epoch has significant implications, as it allows us to predict the maximum stellar mass that can be formed before clouds are dispersed via radiative feedback (see below).

2. *Time Dependence of the Star Formation Rate*

After an initial transient (ending at $t_{\rm break} \sim 0.8 t_{\rm ff,0}$, when $\sim 10\%$ of the gas has collapsed to make stars), the SFR in our simulations reaches a near-constant value with $M_* \propto (t - t_{\rm break})^{\beta}$, for $\beta \sim 0.8 - 1.2$ (see Figure 32). The majority of the stars in the cloud are therefore formed at near-constant SFR.

Analyses of previous driven-turbulence simulations (Wang et al. 2010; Padoan & Nordlund 2011; Bate 2012; Krumholz et al. 2012; Federrath & Klessen 2012) have mostly concluded that the SFR is approximately constant, as we do. Other simulations have also shown an initial slow phase of stellar growth, which is generally treated as a transient effect arising from unrealistic cloud initial conditions, where the velocity structure is not consistent with cloud self-gravity. However, the idea of a constant SFR has recently come into question, with Myers et al. (2014); Lee et al. (2015) suggesting that the initial behavior is not simply a transient; instead, self-gravity alters the global density structure, resulting in an SFE closer to quadratic than linear in time.

Although our simulations are not perfectly suited to resolving the discrepancy between these two views (as we start from very artificial initial conditions), there does appear to be a very distinct break in the stellar mass evolution at $M_* \sim 0.1\ M_{\rm cl,0}$, after which the stellar mass grows linearly. Future simulations which start with more realistic initial density and velocity distributions (extracted from larger-scale galactic-disk models), while also including physical feedback rather than idealized forcing, should provide more realistic understanding of histories of star formation in turbulent clouds.

3. *Star Formation Efficiency per Freefall Time*

The roughly constant SFR in our simulations (after the calculated break time) makes it straightforward to calculate the SFE per freefall time, $\varepsilon_{{\rm ff},\bar{\rho}} \equiv \langle \dot{M}_* \rangle t_{{\rm ff},\bar{\rho}} / M_{\rm cl,0}$ (see Equation 25). We find $\varepsilon_{{\rm ff},\bar{\rho}} \sim 0.3 - 0.5$ (Figure 33a) for clouds with $\alpha_{\rm vir,0} = 2$, similar to results from other recent simulations of turbulent, star forming clouds (Padoan & Nordlund 2011; Padoan et al. 2012; Federrath & Klessen 2012; Myers et al. 2014; Lee et al. 2015). Our measured $\varepsilon_{{\rm ff},\bar{\rho}}$ values increase slightly with increased surface density or higher Mach number but depend more strongly on initial virial parameter. As the initial $\alpha_{\rm vir,0}$ increases above unity, $\varepsilon_{{\rm ff},\bar{\rho}}$ decreases systematically (Figure 33b). For the high initial $\alpha_{\rm vir,0}$ models, $\varepsilon_{{\rm ff},\bar{\rho}}$ can be as low as 0.1. These results are in line with other (driven-turbulence) simulations, in which the Mach

number and magnetization affect the SFR modestly, but the value of $\varepsilon_{\rm ff}$ depends strongly on $\alpha_{\rm vir}$ (e.g., Padoan et al. 2012). It must be kept in mind, however, that in our models $\alpha_{\rm vir}$ is not constant. This differs from driven-turbulence simulations, in which strong or weak driving can maintain either a low or high level for $\alpha_{\rm vir}$, and $\varepsilon_{\rm ff}$ secularly decreases with $\alpha_{\rm vir}$. For our low turbulence models, $\alpha_{\rm vir}$ grows to reach unity well before t_{50}, which explains why $\varepsilon_{{\rm ff},\bar{\rho}}$ is relatively constant for $\alpha_{\rm vir,0} \lesssim 1$. For high initial turbulence models, $\alpha_{\rm vir}$ drops but never reaches ~ 1 as clouds disperse from the simulation volume before this occurs, which explains why $\varepsilon_{{\rm ff},\bar{\rho}}$ decreases for $\alpha_{\rm vir,0} \gtrsim 2$.

We note that direct radiation feedback does not significantly alter $\varepsilon_{{\rm ff},\bar{\rho}}$ (Figure 33). In comparison to simulations with no feedback, the SFR is mildly reduced: the suppression is stronger at low surface density, but is never more than a factor of $\sim 2/3$. This implies that the primary role of the direct radiation force that we have studied is in truncating star formation by removing gas from clouds, rather than in altering their internal states and star-forming properties.

For both our simulations and others, the low values of $\varepsilon_{\rm ff} \lesssim 0.1$ inferred from many observations (e.g., Krumholz et al. 2012) are only achieved for models with large $\alpha_{\rm vir}$, i.e., unbound rather than bound clouds, or systems where gas concentrations are dispersed by turbulence faster than they collapse gravitationally. Traditionally, GMCs have been believed to be gravitationally bound structures, i.e., with $\alpha_{\rm vir} \sim 1$ (e.g., Solomon et al. 1987; Fukui et al. 2008; Bolatto et al. 2008; Wong et al. 2011). However, gas masses (and therefore virial parameters) of clouds are in fact uncertain, because they either rely on adopting a constant X_{CO} for ^{12}CO, or using another tracer such as ^{13}CO that may not be in LTE in some locations and may be optically thick in others (Bolatto et al. 2013). Indeed, Roman-Duval et al. (2010b) find a wide range of $\alpha_{\rm vir}$ from the Galactic Ring Survey sample. In principle, it would be possible to reconcile theory with observations if molecular gas cycles through both high-$\alpha_{\rm vir}$ and $\alpha_{\rm vir} \sim 1$ states, spending most of its time in the former as "diffuse" gas (see below) and creating stars rapidly only during the latter. To resolve this issue, it will be crucial to obtain empirical measures of the mass fractions of molecular gas at different values of $\alpha_{\rm vir}$.

4. *Cloud Lifetimes*

The consequence of their relatively large $\varepsilon_{\rm ff}$ is that our model clouds evolve quickly, converting some fraction of their gas mass to stars and dispersing the rest on very short timescales (see Fig. 34). We find cloud lifetimes $\sim 1.5-2\ t_{\rm ff,0}$, with the duration of the star formation epoch $\sim 0.7-1.5\ t_{\rm ff,0}$. For our range of parameters, cloud lifetimes are between 2 and 8 Myr.

Observationally, GMC cloud lifetimes are estimated to be $\sim 20-40$ Myr (Leisawitz et al. 1989; Kawamura et al. 2009; Miura et al. 2012; Gratier et al. 2012; Meidt et al. 2015), considerably longer than lifetimes of our model clouds. These estimates typically involve dividing clouds into three distinct populations: Type I with no stars, Type II with HII regions, and Type III with star clusters and HII regions, and then adding together their individual lifetimes. Because our simulated clouds have artificial initial conditions, including containing all their

gas initially rather than accreting it over time, they do not properly model the first two phases that are seen in observed GMCs. The duration of the main star formation/cloud dispersal epoch in our simulations (see Fig. 34c) is only a factor ~ 2 below observed duration estimates of the Type III phase ~ 7 Myr.

5. *Lifetime Star Formation Efficiency*

   In our numerical simulations, we define the net SFE over a cloud lifetime $\varepsilon_{\rm final}$ as the fraction of a cloud's initial mass that ends up in star particles. We measure values in the range $\varepsilon_{\rm final} \sim 0.1 - 0.6$, increasing secularly with the cloud's initial surface density according to $\varepsilon_{\rm final} = 0.37\ {\rm log}\Sigma - 0.26$ over a broad range between 10 and 300 $M_\odot$ pc^{-2} (Figure 24a).

   Our simulations also show a decrease in the efficiency with increasing virial parameter, $\varepsilon_{\rm final} = -0.45\ {\rm log}\alpha_{\rm vir,0} + 0.51$ (Figure 24b). However, the role that turbulence plays in setting the star formation efficiency is more difficult to interpret than that of the surface density, as there are a number of competing effects to disentangle, some of which are dependent on our initial conditions. Turbulence provides support for the cloud, thereby preventing collapse and slowing down star formation, but at the same time, turbulence also broadens the density and surface density distributions, making it more difficult for radiation to drive gas out of the cloud; hence the final efficiency is higher (see item 6 below).

   Naively, our simulations might be taken to suggest that the first effect is dominant, since the star formation efficiency decreases with increasing virial parameter. However, it must be stressed that the lower turbulence clouds start from an artificial state and collapse to a new state that is higher in both surface density and virial parameter. This means that the increased star formation efficiency at low $\alpha_{\rm vir,0}$ can be understood entirely in terms of an enhancement in surface density. Overall, the reduction of star formation by turbulence is relatively modest, in that $\varepsilon_{\rm ff} \sim 0.3-0.5$ for clouds once they have reached a natural "virialized" state. As discussed below, however, the limitation of radiation effects by turbulence-induced compression can increase $\varepsilon_{\rm final}$ by a large factor (more than an order of magnitude) compared to the case in which the density is uniform.

   Except at large values of initial $\alpha_{\rm vir}$ and small Σ, the values of $\varepsilon_{\rm final}$ we find are larger than those observed in Milky Way GMCs (see Section 1). This suggests that other feedback effects that we have not included may be important in trucating star formation in individual GMCs. Yet, other recent investigations of the effects of photoionization on GMC evolution (Walch et al. 2012; Dale et al. 2012, 2013) have also found that star formation efficiencies are quite high. Potentially, the combined effects of non-ionizing and ionizing radiation are not simply additive, such that the overall impact on limiting star formation in a cloud is much greater. However, it is also possible that star formation feedback from supernovae—either within clouds or originating at nearby locations—is more important than the combined early feedback in unbinding the majority of the mass in a GMC. Alternatively, if GMCs have large virial parameters (see below) or are magnetically subcritical, they could have significantly reduced SFRs. It is important to explore all of these alternatives in future simulations.

If most molecular gas is in GMCs, the SFEs and lifetimes of clouds combine to determine the overall molecular depletion time in a galaxy (or galactic region). Averaging over the star-forming epoch of model clouds leads to an effective depletion time $t_{\rm dep} = \Delta t/\varepsilon_{\rm final} =$ 4 to 20 Myr for the Σ-series (Fig. 34d), where $\Delta t \equiv t_{\rm unb} - t_*$ or $t_{90} - t_*$. For the α-series, the corresponding range is 2 to 50 Myr. These values are very small compared to the Gyr extragalactic depletion times measured for CO-emitting gas (see Section 1). The ratio $t_{\rm dep}/t_{\rm ff,0}$ is 2.0 to 2.9 for the Σ-series, and 0.5 to 12 for the α series. While inclusion of additional early feedback effects and magnetic fields would likely reduce the SFE and increase $t_{\rm dep}$ over a cloud lifetime, it is also possible that much of the CO-emitting gas is in fact not in strongly-bound systems. These conditions would be more similar to high-$\alpha_{\rm vir}$ models than near-virial cases. In addition, if observed CO-emitting gas is at lower density, with longer $t_{\rm ff,0}$ than the range we have considered, it would also tend to increase the depletion time.

Maintaining high enough $\alpha_{\rm vir}$ and/or low enough mean density to match the depletion times observed in extragalactic systems likely requires much more strongly driven turbulence than radiation feedback alone can supply. It is possible that in molecule-dominated regions of galaxies, similar to atomic-dominated regions, most of the gas is effectively diffuse, and turbulence is primarily driven by late-stage expanding SNRs. In numerical simulations of diffuse-dominated galactic disk regions with dynamics governed by momentum input from SNRs, the values $\varepsilon_{\rm ff} \sim 0.006$ are indeed found to be quite small, independent of the large-scale mean gas surface density in the disk (Kim et al. 2013).

6. *Analytic Limits on the Star Formation Efficiency*

For a given total stellar luminosity as set by the instantaneous value of ε, only gas in structures of sufficiently low surface density will have the outward radiation force exceed the inward gravitational force. This defines a (time-varying) "Eddington" surface density Σ_E (which depends on ε according to Equation 10) below which gas can be expelled. Our simulations (and other work) show that the PDF of surface densities in a cloud follows a lognormal distribution set by the mean surface density of a cloud and its internal turbulence. For a cluster-forming cloud with a given PDF of circumcluster surface densities, there is a maximum fraction of the original cloud material that can become super-Eddington. At low SFE, the luminosity is low and only a small fraction of the mass (in structures with very low Σ) can be driven out of the cloud; if the SFE is high, all of the remaining gas would be super-Eddington, but there would be very little material available. This suggests that clouds may evolve by sequential expulsion of portions of gas at increasingly high surface density until the maximum mass in outflowing material is reached. We argue that the maximum final SFE $\varepsilon_{\rm max}$ for $\alpha_{\rm vir} \sim 1$ clouds would then depend only on the initial cloud mean surface density and the variance of the lognormal (which does not vary much over our models). Equation (22a) provides a prediction for $\varepsilon_{\rm final}$ based on this formulation, which agrees quite well with our numerical results.

Thompson & Krumholz (2016) also developed an analytic model for the net SFE in a cloud

that accounts for the lognormal distribution of surface densities relative to a critical value that depends on the total stellar luminosity; it differs from our model in that it explicitly depends on timescales for star formation and mass ejection as parameters. While, for their default parameter values, their predicted SFE is much lower than we find numerically, it is closer when a larger value for $\varepsilon_{\rm ff}$ is adopted. Both our analytic model and our numerical simulations show that allowing for a nonuniform (lognormal) surface density distribution leads to much greater final SFE than in simpler "Eddington"-type models with a single instantaneous mean surface density, as in Equation (12) (see also Murray et al. 2010; Fall et al. 2010; Dekel & Krumholz 2013; Kim et al. 2016).

Finally, we note that in sufficiently dense clouds, at least the upper end of the lognormal surface density distribution will be optically thick to IR. It will be interesting to extend into this regime and compare numerical and analytic models that allow for both direct and reprocessed radiation forces. We also note that Equation (22a) predicts a decrease in $\varepsilon_{\rm max}$ at lower $\sigma_{\ln\Sigma}$ (see Figure 27). Potentially, inclusion of magnetic fields could reduce $\sigma_{\ln\Sigma}$ and therefore the SFE; as real GMCs have significant magnetization, this represents an important question to address with future simulations.

We are grateful to the referee for a careful reading of the manuscript and very thorough report, which helped us to improve the presentation. This work was supported by Grant No. AST-1312006 from the National Science Foundation. Part of this project was conducted during a visit to the KITP at U.C. Santa Barbara, which is supported by the National Science Foundation under Grant No. NSF PHY-1125915. MAS is supported by the Max-Planck/Princeton Center for Plasma Physics under Grant No. NSF PHY-1144374. Simulations were performed on the computational resources supported by the PICSciE TIGRESS High Performance Computing Center at Princeton University.

A. Tests of the Numerical Code

In this section, we present tests that examine the extent to which numerical approximations in our code and limited numerical resolution might affect our results. In particular, we are interested in quantifying the regimes of cloud mass and radius (or, equivalently, surface density) over which we accurately capture the physics of radiatively-driven expansion.

Both the *Athena* MHD code and the *Hyperion* RHD extension have been tested extensively in the past. However, the majority of the tests of the *Hyperion* module were performed with radiation in the diffusion limit. This would be satisfied in very optically thick clouds, in which the effects of reprocessed IR continuum radiation are dominant (Skinner & Ostriker 2015). Here, we are interested in the case where gas is optically thick to UV photons from the source and optically thin to re-emitted IR radiation. In this context, the interaction of gas and radiation is very different,

as there is strong local absorption rather than absorption and re-emission over large volumes. We therefore implement several tests to see how well we model this behavior in successively more realistic scenarios.

A.1. Radiative Momentum-Driven Expanding Shell

To test our code behavior in highly idealized conditions, we consider the expansion of a spherical shell of gas due to the absorption of radiation momentum from a central source, similar to that described in Ostriker & Shetty (2011); Skinner & Ostriker (2013). In this problem, we imagine an idealized spherical GMC of mass $M_{\rm cl,0}$ that forms stars of total mass M_* with efficiency $\varepsilon = M_*/M_{\rm cl,0}$. The remaining gas of mass $M_{\rm sh} \equiv (1-\varepsilon)M_{\rm cl,0}$ is ejected as an expanding, spherical shell of radius r due to the radiation force from the stellar component. The stars are modeled here as a centrally-located cluster.

We initialize a shell at an initial radius r_0 with zero velocity at time $t = 0$. In reality, the shell would have some initial velocity, but this just provides an additive constant. Assuming the ejected shell is thin and of uniform surface density $\Sigma(r) = M_{\rm sh}/(4\pi r^2)$, the optical depth across the shell is $\tau_{\rm sh}(r) \approx \Sigma(r)\kappa$, where κ is the absorption opacity of the gas to UV photons. If, as discussed earlier, we are in the limit where we consider only UV radiation, then the flux at r is given by

$$F(r) = \frac{L_*}{4\pi r^2}\exp\left[-\int^r \rho(r')\kappa dr'\right] \equiv \frac{L_* {\rm e}^{-\tau_{\rm sh}(r)}}{4\pi r^2}. \tag{A1}$$

The total radiation force on the shell is then

$$\int F(r)\rho(r)\frac{\kappa}{c}4\pi r^2 dr = \frac{L_*}{c}\int {\rm e}^{-\tau}d\tau = \frac{L_*}{c}(1-{\rm e}^{-\tau_{\rm sh}(r_{\rm max})}). \tag{A2}$$

Neglecting gravitational and internal pressure forces, the outward acceleration of the shell becomes

$$\ddot{r} = \frac{L_*\left[1-\exp\left(-\Sigma(r)\kappa\right)\right]}{M_{\rm sh}c}, \tag{A3}$$

which is independent of the shell's thickness. Substituting for the surface density and the cluster luminosity, the shell acceleration reduces to

$$\ddot{r} = \frac{\Psi\varepsilon(1-{\rm e}^{-\tau_0(r_0/r)^2})}{c(1-\varepsilon)}, \tag{A4}$$

where we have introduced the shell optical depth at $r = r_0$, given by

$$\begin{aligned}\tau_0 &\equiv M_{\rm sh}\kappa/(4\pi r_0^2) \\ &= 1.67\left(\frac{r_0}{10\ {\rm pc}}\right)^{-2}\left(\frac{\kappa}{1000\ {\rm cm^2\ g^{-1}}}\right)\left(\frac{M_{\rm sh}}{10^4\ M_\odot}\right).\end{aligned} \tag{A5}$$

We may simplify further by rewriting Equation (A4) in terms of the dimensionless variables $\tilde{r} \equiv r/r_0$ and $\tilde{t} \equiv t/t_0$, so that

$$\frac{d^2\tilde{r}}{d\tilde{t}^2} = \frac{\varepsilon(1 - \mathrm{e}^{-\tau_0/\tilde{r}^2})}{(1-\varepsilon)}, \tag{A6}$$

where

$$\begin{aligned} t_0 &\equiv \sqrt{\frac{r_0 c}{\Psi}} \\ &= 0.68 \text{ Myr} \left(\frac{r_0}{10 \text{ pc}}\right)^{1/2} \left(\frac{\Psi}{2000 \text{ erg s}^{-1} \text{ g}^{-1}}\right)^{-1/2}. \end{aligned} \tag{A7}$$

The presence of the exponential term in inverse radius precludes a general analytic solution to this problem. However, in the optically thick ($\tau_{\rm sh} \gg 1$) limit, or close to the initial shell radius with $\tau_{\rm sh}(r) \approx \tau_0$, all explicit dependence on radius drops out of Equation (A6). For the $\tau \approx \tau_0$ case it may then be solved trivially to give a quadratic expansion in time

$$\tilde{r} = \frac{\varepsilon(1 - \mathrm{e}^{-\tau_0})}{2(1-\varepsilon)}\tilde{t}^2 + 1.0; \tag{A8}$$

in the optically thick case, we instead have $1 - \mathrm{e}^{-\tau_0} \rightarrow 1$. We note that if the shell is optically thick, then to first order the solution depends only on the inital shell radius, star formation efficiency ε, and luminosity per unit mass Ψ (see Equation A4). Otherwise, dependence on the mass and opacity only enters through τ_0 (see Equation A5) and is only significant for relatively low optical depths.

A.1.1. Convergence Tests

In this test, we wish to explore the sensitivity of our code to changes in the key physical parameters κ and $M_{\rm cl,0}$, as well as numerical parameters N, and $\hat{c}$. We consider a central luminous cluster defined by a sink particle at the origin, with $r_* = 1$ pc for the radiation source function given in Equation (5). This central source illuminates a thin shell with Gaussian density profile given by

$$\rho_{\rm sh}(r) = \frac{M_{\rm sh}}{4\pi r_0^2 \sqrt{2\pi\sigma_{\rm sh}^2}} \exp\left(-\frac{(r-r_0)^2}{2\sigma_{\rm sh}^2}\right), \tag{A9}$$

where $H_0 = 2\sqrt{2\ln 2}\sigma_{\rm sh}$ is the FWHM of the shell.

For this test, we initialize the radiation field using the result of a prior simulation in which we turn on the cluster and evolve the radiation field without evolving the gas hydrodynamics. The final radiation field after ~ 10 radiation crossing times can then be used to initialize the flux and energy density for the case where we consider shell expansion.

To prevent the gas time steps from becoming prohibitively small, we enforce a density floor of $\rho_{\rm min} \equiv 10^{-8}\rho_{\rm sh}(r = r_0)$ initially, as well as after each gas integration step. We employ an N^3

grid on the domain $(x, y, z) \in ([0, 3\,r_0], [0, 3\,r_0], [0, 3\,r_0])$ and enforce outflow boundary conditions along all faces of the box that do not touch the origin of the cloud. We note that due to spherical symmetry, we only run the test in a single octant of the sphere. We run each simulation for a time $t \approx 2t_0$ so that the planar shell reaches an outermost radius of $r \approx 3r_0$.

For the RSLA, it is necessary to choose a value of $\hat{c}$ such that $v_{\rm max} \ll \hat{c}$ at all times. For each of our simulations, the shell reaches a maximum velocity of $v_{\rm max} = \varepsilon v_0 \tilde{t}_{\rm max}/(1-\varepsilon)$, where

$$\begin{aligned} v_0 &\equiv \sqrt{\frac{\Psi r_0}{c}} \\ &= 14.4 \text{ km s}^{-1} \left(\frac{r_0}{10 \text{ pc}}\right)^{1/2} \left(\frac{\Psi}{2000 \text{ erg s}^{-1} \text{ g}^{-1}}\right)^{1/2}. \end{aligned} \tag{A10}$$

As we use $\varepsilon = 0.5$ and $\tilde{t}_{\rm max} = 2$, a choice of $\hat{c} = 250$ km s^{-1} should be satisfactory for the RSLA in most situations. Of course, increased values of Ψ or the star formation efficiency ε will provide greater accelerations and so require higher values of $\hat{c}$. The robustness of our results to variations in $\hat{c}$ is therefore also verified below.

We begin by adopting a set of fiducial parameters roughly characteristic of Milky Way clouds. In addition to $\Psi = 2000$ erg s^{-1} g^{-1} and $\kappa = 1000$ cm^2 g^{-1}, we choose an initial shell radius of $r_0 = 10$ pc, a relatively thin initial shell width of $H_0 = 1.0$ pc, and a cloud mass of $M_{\rm cl,0} = 10^4\ M_\odot$. This mass provides a marginally optically thick shell $\tau_0 \approx 2$ (see Equation A5). Finally, we adopt a star formation efficiency of $\varepsilon = 0.5$; although this is high for Milky Way GMCs, it is similar to the upper range of what we find in our full cloud simulations.

For this test we adopt a sound speed of $c_s = 0.5$ km s^{-1}, which lies somewhere between the turbulent velocities in our full cloud simulations and the true sound speed (a factor of 2 lower). This helps ensure that when resolution is adequate, the shell does not develop thin-shell instability as it is accelerated outward, which would compromise our ability to compare to the analytic spherical solution.

We are initially interested in the numerical parameters N and $\hat{c}$ required to match the analytic thin shell solution for a typical GMC. In Figure 35 we show the results for several fiducial simulations run at different numerical resolutions. Pictured are snapshots of density in slices through the x-y plane at $t = 1.2t_0$ when the mean radius is $r \sim 1.7r_0$ for resolutions $N = 64, 128, 256$, and 512. We note that the shell width remains roughly constant or only slightly expands to a final shell width of $H \sim 2$ pc. However, in the lowest resolution simulation, $N = 64$, the spherical shell is disturbed by grid scale noise. By the time the shell has expanded to close to twice its initial radius, it is no longer spherical, but instead, has large scale perturbations with angle caused by the initial difficulty of resolving a spherical shell on a square grid.

Figure 36a shows the evolution of mass-weighted shell radius with time as compared to the analytic solution at varying resolution for a cloud of mass $10^4\ M_\odot$. Since the optical depth has a radial dependence that appears through the surface density, we may only find the analytic solution

by numerically integrating Equation (A6). Evidently, the numerical solution follows the analytic prediction fairly well even at low resolution, although for higher curvature structures, the accuracy would be reduced at each given resolution. The main conclusion from this test is that at the typical resolution of our simulations, we are able to satisfactorily capture the predicted expansion driven by radiation forces.

The primary other numerical parameter that may affect our results is the reduced speed of light $\hat{c}$. In *Hyperion* simulations measuring the effect of reprocessed radiation, results can be quite sensitive to this parameter, since the RSLA static diffusion criterion requires that the effective radiation diffusion speed remain large compared to dynamical speeds, i.e., $\hat{c}/\tau_{\rm max} \gg v_{\rm max}$, where $\tau_{\rm max}$ is the maximum optical depth across all cells. However, for direct radiation the RSLA criterion is simply $\hat{c} \gg v_{\rm max}$, where the highest surface density clouds we consider typically have $v_{\rm max} \sim v_{\rm esc} \sim 15$ km s^{-1}. The shell expansion test with the fiducial cloud parameters described above has $v_{\rm max} \sim \sqrt{2}v_0 = 20$ km s^{-1}. Figure 36b, showing results for varying $\hat{c}$, demonstrates that there is only a small error with respect to the analytic solution for $\hat{c} \sim 100$ km s^{-1}, and we recover it exactly for $\hat{c} = 250$ km s^{-1}. As discussed earlier, we have conservatively adopted the latter value for all our cloud simulations.

Figure 37a shows the same evolution of shell radius as Figure 36a, but for a more massive cloud with $M_{\rm cl,0} = 3 \times 10^5\ M_\odot$, i.e., thirty times larger than in Figure 36a. The mass of the central cluster is again half this at $M = 1.5 \times 10^5\ M_\odot$. Evidently, the numerical tests no longer agree closely with the analytic solutions for higher mass shells, for numerical resolution N in the range shown. In all cases, the numerical solution systematically underestimates the shell radius. While increasing the numerical resolution may marginally improve the agreement between analytic and numerical solutions, the error is still close to $\sim 10\%$ once the shell has reached the edge of the simulation volume. Meanwhile, if we consider the same test for varying $\hat{c}$ (Figure 37b), we see that increasing the reduced speed of light beyond our adopted value of $\hat{c} = 250$ km s^{-1} does not remedy this discrepancy either. As further tests show (see below), this discrepancy can in fact be traced to inadequate resolution of the flux.

A.1.2. Flux Resolution

The optical depth across individual cells in our grid is $\tau_{\rm cell} = \rho\kappa\Delta x$. If this optical depth exceeds unity by a considerable amount, then the flux across cells is not well resolved spatially and the impulse provided to the gas is not captured accurately. For the shell problem, with $\rho_{\rm sh}(r) \approx \Sigma/H$ and $\Delta x = 4r_0/N$,

$$\tau_{\rm cell} \rightarrow \frac{4\Sigma\kappa r_0}{HN_x}; \tag{A11}$$

this depends on the opacity, the shell surface density (and hence mass and radius) and the numerical resolution.

We may systematically test the dependence of the solution accuracy on $\tau_{\rm cell}$ by using the shell problem with varying κ and Σ (through $M_{\rm cl,0}$). Figure 38a shows the result from varying opacity over two orders of magnitude between 10^3 and 10^5 g cm^{-2}. Above $\kappa \sim 10^4$g cm^{-2}, the shell is completely optically thick and there is no variation in the analytic solution with opacity. The numerical results match the analytic solutions well for opacities $\kappa = 2000$ g cm^{-2} and below, but then they deteriorate as the opacity increases to $\kappa = 5000$ g cm^{-2}. Interestingly, beyond this opacity, even up to $\kappa = 10^5$ g cm^{-2} there is not a significant further increase in the error relative to the analytic solution, and there is only a 10% deviation in radius out to 2 times the initial shell radius (where a real cloud could have become gravitationally unbound).

The underlying reason for these deviations can be seen in the maximum optical depth across individual cells as shown in Figure 38b. In all cases, this increases by up to a factor ~ 10 from its starting value as the shell is compressed during expansion, and then decreases as the shell expands outwards and the mean shell density decreases. More importantly, the value of the maximum optical depth plays a key role in determining solution accuracy. We see that for $\kappa = 2000$ and $\kappa = 5000$ g cm^{-2}, the optical depths peak at $\tau_{\rm cell} = 1.3$ and $\tau_{\rm cell} = 4.3$, respectively, and somewhere between these, there is a transition point at $\tau_{\rm cell} \sim 2-3$ beyond which the flux is not well resolved. For $\kappa = 5000$ g cm^{-2}, $\tau_{\rm cell} \gtrsim 2$ for around $0.5t_0$, and the numerical simulation differs from the analytic solution by around 5%. For larger $\kappa = 10^4$ g cm^{-2}, $\tau_{\rm cell} \gtrsim 2$ for the majority of the shell evolution, which leads to the 10% errors discussed earlier. Beyond this point, increasing the opacity does not have a strong effect on the solution accuracy, since $\tau_{\rm cell} \gtrsim 2$ always.

Figure 39 shows results of similar tests, in which we vary the surface density (through $M_{\rm cl,0}$). Over a range of two orders of magnitude above the fiducial surface density, we see the same trends with cell optical depth. For $M_{\rm cl,0} \lesssim 3 \times 10^4\ M_\odot$, for which $\tau_{\rm cell} \leq 2$ at all times, we match the analytic solution reasonably well. However, at larger masses and correspondingly larger $\tau_{\rm cell}$, we again underestimate the shell expansion velocity at all times.

We conclude that, provided $\tau_{\rm cell}$ remains below ~ 2, we can obtain an accurate solution for this problem. Since $\tau_{\rm cell}$ is inversely proportional to N, we can in principle capture the behavior in increasingly high-density clouds by increasing the numerical resolution, although in practice this becomes numerically prohibitive for very dense systems. In any case, regardless of how high $\tau_{\rm cell}$ becomes, we never underpredict the shell radius by more than 10% even by the time gas in one of our turbulent clouds will have become unbound.

Finally, we note that the maximum values of $\tau_{\rm cell}$ depend strongly on gas compression and hence, on the detailed problem-specific evolution of turbulent clouds. Therefore, while the spherical tests show that a resolution of $N = 256$ is generally sufficient for this problem, we also need to directly test convergence in our full turbulent models.

REFERENCES

Ballesteros-Paredes, J., Vázquez-Semadeni, E., Gazol, A., et al. 2011, MNRAS, 416, 1436

Banerjee, R., Vázquez-Semadeni, E., Hennebelle, P., & Klessen, R. S. 2009, MNRAS, 398, 1082

Bate, M. R. 2012, MNRAS, 419, 3115

Bigiel, F., Leroy, A., Walter, F., et al. 2008, AJ, 136, 2846

Bolatto, A. D., Leroy, A. K., Rosolowsky, E., Walter, F., & Blitz, L. 2008, ApJ, 686, 948

Bolatto, A. D., Wolfire, M., & Leroy, A. K. 2013, ARAA, 51, 207

Brunt, C. M. 2015, MNRAS, 449, 4465

Brunt, C. M., Federrath, C., & Price, D. J. 2010, MNRAS, 403, 1507

Carpenter, J. M. 2000, AJ, 120, 3139

Castor, J. I., Abbott, D. C., & Klein, R. I. 1975, ApJ, 195, 157

Chabrier, G. 2003, PASP, 115, 763

Cohen, M., & Kuhi, L. V. 1979, ApJ, 227, L105

Colín, P., Vázquez-Semadeni, E., & Gómez, G. C. 2013, MNRAS, 435, 1701

Collins, D. C., Kritsuk, A. G., Padoan, P., et al. 2012, ApJ, 750, 13

Cunningham, A. J., Frank, A., Quillen, A. C., & Blackman, E. G. 2006, ApJ, 653, 416

da Silva, R. L., Fumagalli, M., & Krumholz, M. 2012, ApJ, 745, 145

Dale, J. E., Bonnell, I. A., Clarke, C. J., & Bate, M. R. 2005, MNRAS, 358, 291

Dale, J. E., Ercolano, B., & Bonnell, I. A. 2012, MNRAS, 424, 377

—. 2013, MNRAS, 430, 234

Davis, S. W., Jiang, Y.-F., Stone, J. M., & Murray, N. 2014, ApJ, 796, 107

Dekel, A., & Krumholz, M. R. 2013, MNRAS, 432, 455

Dib, S., & Burkert, A. 2005, ApJ, 630, 238

Dobbs, C. L., Krumholz, M. R., Ballesteros-Paredes, J., et al. 2013, arXiv.org

Dopita, M. A., Fischera, J., Sutherland, R. S., et al. 2006, ApJ, 647, 244

Draine, B. T. 2011, ApJ, 732, 100

Elmegreen, B. G. 1983, MNRAS, 203, 1011

Elmegreen, B. G., & Scalo, J. 2004, ARAA, 42, 211

Evans, II, N. J., Dunham, M. M., Jørgensen, J. K., et al. 2009, ApJ Supp, 181, 321

Fall, S. M., Krumholz, M. R., & Matzner, C. D. 2010, ApJ, 710, L142

Falle, S. A. E. G. 1991, MNRAS, 250, 581

Federrath, C., Banerjee, R., Clark, P. C., & Klessen, R. S. 2010, ApJ, 713, 269

Federrath, C., & Klessen, R. S. 2012, ApJ, 761, 156

—. 2013, ApJ, 763, 51

Federrath, C., Klessen, R. S., & Schmidt, W. 2008, ApJ, 688, L79

—. 2009, ApJ, 692, 364

Fukui, Y., Kawamura, A., Minamidani, T., et al. 2008, ApJ Supp, 178, 56

García, P., Bronfman, L., Nyman, L.-Å., Dame, T. M., & Luna, A. 2014, ApJ Supp, 212, 2

Genzel, R., Tacconi, L. J., Lutz, D., et al. 2015, ApJ, 800, 20

Gnedin, N. Y., & Abel, T. 2001, New A, 6, 437

Gong, H., & Ostriker, E. C. 2013, ApJ Supp, 204, 8

González, M., Audit, E., & Huynh, P. 2007, A&A, 464, 429

Goodman, A. A., Pineda, J. E., & Schnee, S. L. 2009, ApJ, 692, 91

Gratier, P., Braine, J., Rodriguez-Fernandez, N. J., et al. 2012, A&A, 542, A108

Hansen, C. E., Klein, R. I., McKee, C. F., & Fisher, R. T. 2012, ApJ, 747, 22

Harper-Clark, E., & Murray, N. 2009, ApJ, 693, 1696

Heyer, M., Krawczyk, C., Duval, J., & Jackson, J. M. 2009, ApJ, 699, 1092

Hockney, R. W., & Eastwood, J. W. 1981, Computer Simulation Using Particles

Hopkins, P. F. 2013, MNRAS, 430, 1880

Iffrig, O., & Hennebelle, P. 2015, A&A, 576, A95

Kainulainen, J., Beuther, H., Henning, T., & Plume, R. 2009, A&A, 508, L35

Kawamura, A., Mizuno, Y., Minamidani, T., et al. 2009, ApJ Supp, 184, 1

Kennicutt, R. C., & Evans, N. J. 2012, ARAA, 50, 531

Kim, C.-G., & Ostriker, E. C. 2015, ApJ, 802, 99

Kim, C.-G., Ostriker, E. C., & Kim, W.-T. 2013, ApJ, 776, 1

Kim, J.-G., Kim, W.-T., & Ostriker, E. C. 2016, ArXiv e-prints

Klessen, R. S., Heitsch, F., & Mac Low, M.-M. 2000, ApJ, 535, 887

Kritsuk, A. G., Norman, M. L., & Wagner, R. 2011, ApJ, 727, L20

Krumholz, M. R. 2014, ArXiv e-prints

Krumholz, M. R., & Dekel, A. 2010, MNRAS, 406, 112

Krumholz, M. R., Dekel, A., & McKee, C. F. 2012, ApJ, 745, 69

Krumholz, M. R., Fumagalli, M., da Silva, R. L., Rendahl, T., & Parra, J. 2015, MNRAS, 452, 1447

Krumholz, M. R., Klein, R. I., McKee, C. F., & Bolstad, J. 2007, ApJ, 667, 626

Krumholz, M. R., & Matzner, C. D. 2009, ApJ, 703, 1352

Krumholz, M. R., Matzner, C. D., & McKee, C. F. 2006, ApJ, 653, 361

Krumholz, M. R., & McKee, C. F. 2005, ApJ, 630, 250

Krumholz, M. R., & Tan, J. C. 2007, ApJ, 654, 304

Krumholz, M. R., & Thompson, T. A. 2012, ApJ, 760, 155

Lada, C. J., Lombardi, M., & Alves, J. F. 2010, ApJ, 724, 687

Larson, R. B. 1969, MNRAS, 145, 271

Lee, E. J., Chang, P., & Murray, N. 2015, ApJ, 800, 49

Leisawitz, D., Bash, F. N., & Thaddeus, P. 1989, ApJ Supp, 70, 731

Leroy, A. K., Walter, F., Sandstrom, K., et al. 2013, AJ, 146, 19

Levermore, C. D. 1984, J. Quant. Spec. Radiat. Transf., 31, 149

Li, Z.-Y., & Nakamura, F. 2006, ApJ, 640, L187

Lombardi, M., Alves, J., & Lada, C. J. 2015, A&A, 576, L1

Lombardi, M., Lada, C. J., & Alves, J. 2010, A&A, 512, A67

Lopez, L. A., Krumholz, M. R., Bolatto, A. D., Prochaska, J. X., & Ramirez-Ruiz, E. 2011, ApJ, 731, 91

Lopez, L. A., Krumholz, M. R., Bolatto, A. D., et al. 2014, ApJ, 795, 121

Mac Low, M.-M., & Klessen, R. S. 2004, Reviews of Modern Physics, 76, 125

Martizzi, D., Faucher-Giguère, C.-A., & Quataert, E. 2015, MNRAS, 450, 504

Matzner, C. D. 2002, ApJ, 566, 302

McKee, C. F., & Ostriker, E. C. 2007, ARAA, 45, 565

McKee, C. F., van Buren, D., & Lazareff, B. 1984, ApJ, 278, L115

Meidt, S. E., Hughes, A., Dobbs, C. L., et al. 2015, ArXiv e-prints

Miura, R. E., Kohno, K., Tosaki, T., et al. 2012, ApJ, 761, 37

Mizuno, N., Rubio, M., Mizuno, A., et al. 2001, PASJ, 53, L45

Molina, F. Z., Glover, S. C. O., Federrath, C., & Klessen, R. S. 2012, MNRAS, 423, 2680

Mooney, T. J., & Solomon, P. M. 1988, ApJ, 334, L51

Murray, N. 2011, ApJ, 729, 133

Murray, N., Quataert, E., & Thompson, T. A. 2010, ApJ, 709, 191

Myers, A. T., Klein, R. I., Krumholz, M. R., & McKee, C. F. 2014, MNRAS, 439, 3420

Myers, P. C., Dame, T. M., Thaddeus, P., et al. 1986, ApJ, 301, 398

Nakamura, F., & Li, Z.-Y. 2008, ApJ, 687, 354

O'Dell, C. R., York, D. G., & Henize, K. G. 1967, ApJ, 150, 835

Ostriker, E. C., & Shetty, R. 2011, ApJ, 731, 41

Ostriker, E. C., Stone, J. M., & Gammie, C. F. 2001, ApJ, 546, 980

Padoan, P., Federrath, C., Chabrier, G., et al. 2014, Protostars and Planets VI, 77

Padoan, P., Haugbølle, T., & Nordlund, Å. 2012, ApJ, 759, L27

Padoan, P., & Nordlund, Å. 2011, ApJ, 730, 40

Pellegrini, E. W., Baldwin, J. A., & Ferland, G. J. 2010, ApJ Supp, 191, 160

Pellegrini, E. W., Baldwin, J. A., Brogan, C. L., et al. 2007, ApJ, 658, 1119

Penston, M. V. 1969, MNRAS, 144, 425

Quillen, A. C., Thorndike, S. L., Cunningham, A., et al. 2005, ApJ, 632, 941

Rahman, N., Bolatto, A. D., Xue, R., et al. 2012, ApJ, 745, 183

Raskutti, S., Ostriker, E. C., & Skinner, M. A. 2016, ApJ

Rogers, H., & Pittard, J. M. 2013, MNRAS, 431, 1337

Roman-Duval, J., Jackson, J. M., Heyer, M., Rathborne, J., & Simon, R. 2010a, ApJ, 723, 492

—. 2010b, ApJ, 723, 492

Saintonge, A., Kauffmann, G., Wang, J., et al. 2011, MNRAS, 415, 61

Sales, L. V., Marinacci, F., Springel, V., & Petkova, M. 2014, MNRAS, 439, 2990

Schneider, N., André, P., Könyves, V., et al. 2013, ApJ, 766, L17

Schneider, N., Ossenkopf, V., Csengeri, T., et al. 2015, A&A, 575, A79

Schruba, A., Leroy, A. K., Walter, F., et al. 2011, AJ, 142, 37

Scoville, N. Z., Polletta, M., Ewald, S., et al. 2001, AJ, 122, 3017

Scoville, N. Z., Yun, M. S., Sanders, D. B., Clemens, D. P., & Waller, W. H. 1987, ApJ Supp, 63, 821

Skinner, M. A., & Ostriker, E. C. 2013, ApJ Supp, 206, 21

—. 2015, ApJ

Solomon, P. M., Rivolo, A. R., Barrett, J., & Yahil, A. 1987, ApJ, 319, 730

Springel, V. 2005, MNRAS, 364, 1105

Stone, J. M., & Gardiner, T. 2009, New A, 14, 139

Stone, J. M., Gardiner, T. A., Teuben, P., Hawley, J. F., & Simon, J. B. 2008, ApJ Supp, 178, 137

Stone, J. M., Ostriker, E. C., & Gammie, C. F. 1998, ApJ, 508, L99

Thompson, T. A., & Krumholz, M. R. 2016, MNRAS, 455, 334

Vazquez-Semadeni, E. 1994, ApJ, 423, 681

Vázquez-Semadeni, E., Banerjee, R., Gómez, G. C., et al. 2011, MNRAS, 414, 2511

Vázquez-Semadeni, E., Colín, P., Gómez, G. C., Ballesteros-Paredes, J., & Watson, A. W. 2010, ApJ, 715, 1302

Vázquez-Semadeni, E., & García, N. 2001, ApJ, 557, 727

Vázquez-Semadeni, E., González, R. F., Ballesteros-Paredes, J., Gazol, A., & Kim, J. 2008, MNRAS, 390, 769

Walch, S. K., & Naab, T. 2014, ArXiv e-prints

Walch, S. K., Whitworth, A. P., Bisbas, T., Wünsch, R., & Hubber, D. 2012, MNRAS, 427, 625

Wang, P., Li, Z.-Y., Abel, T., & Nakamura, F. 2010, ApJ, 709, 27

Weaver, R., McCray, R., Castor, J., Shapiro, P., & Moore, R. 1977, ApJ, 218, 377

Weidner, C., & Kroupa, P. 2006, MNRAS, 365, 1333

Weingartner, J. C., & Draine, B. T. 2001, ApJ, 548, 296

Whitworth, A. 1979, MNRAS, 186, 59

Williams, J. P., & McKee, C. F. 1997, ApJ, 476, 166

Wong, T., Hughes, A., Ott, J., et al. 2011, ApJ Supp, 197, 16

Zuckerman, B., & Palmer, P. 1974, ARAA, 12, 279

This preprint was prepared with the AAS LaTeX macros v5.2.

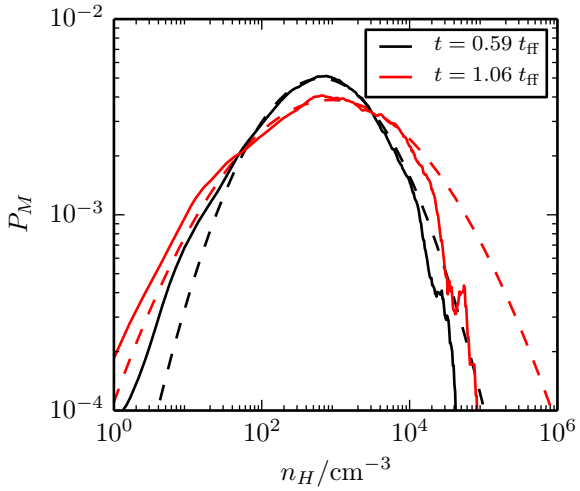

Fig. 7.— **The gas density distribution in our fiducial model at two separate times, $t_{10} = 0.59\ t_{\mathrm{ff},0}$ (black solid) and $t_{50} = 1.06\ t_{\mathrm{ff},0}$ (red solid). We show the distribution of mass as well as the best-fit lognormal to each distribution (dashed), fitting between the 10^{th} and 90^{th} percentiles by mass.**

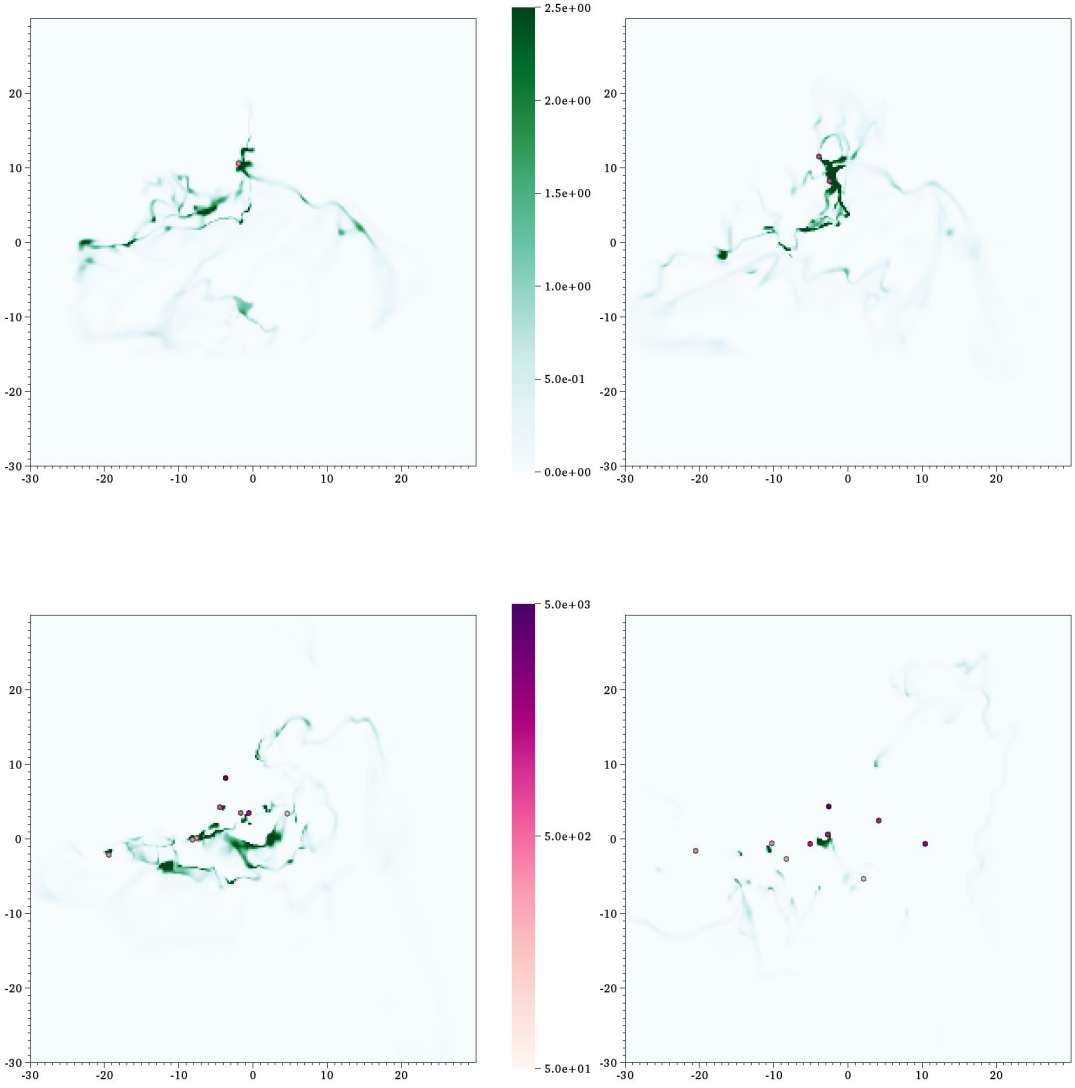

Fig. 8.— Snapshots of the optical depth $\tau_{\rm cell}$ for our fiducial model. We show slices in the x-y plane, passing through the plane of the most massive star particle, at the same four times as Figures 2-5. As in those figures, we show also star particles within $\Delta z = \pm 2$ pc of the slice.

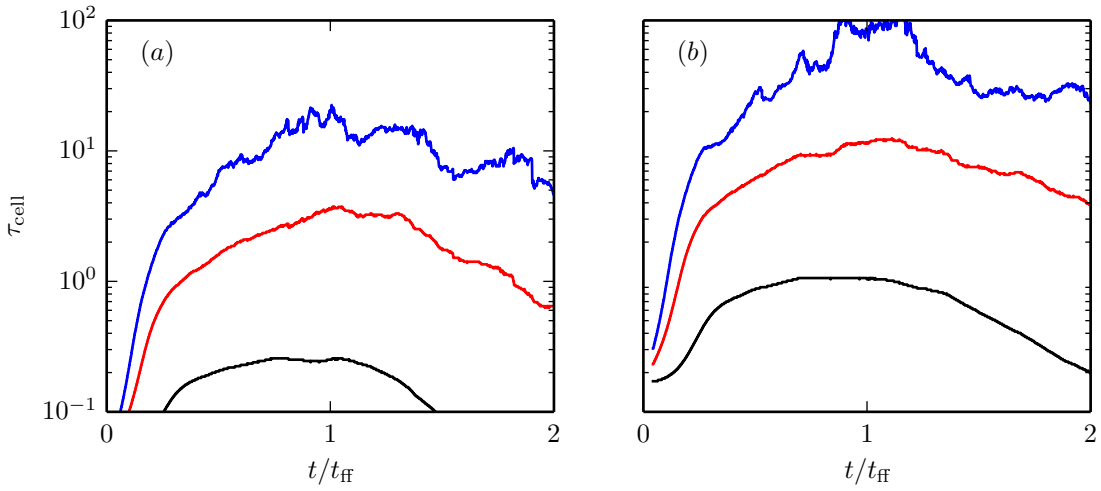

Fig. 9.— Percentiles of the optical depth distribution as a function of simulation time. We show results for both our fiducial cloud (left), and a high surface density cloud with $M_{\rm cl,0} = 2 \times 10^5\ M_\odot$ and $r_0 = 15$ pc, corresponding to $\Sigma_{\rm cl,0} = 283\ {\rm M}_\odot\ {\rm pc}^{-2}$ (right). In both cases we show the optical depth at the $50^{\rm th}$ percentile of the mass distribution (black), the $90^{\rm th}$ percentile (red), and the $100^{\rm th}$ percentile (blue).

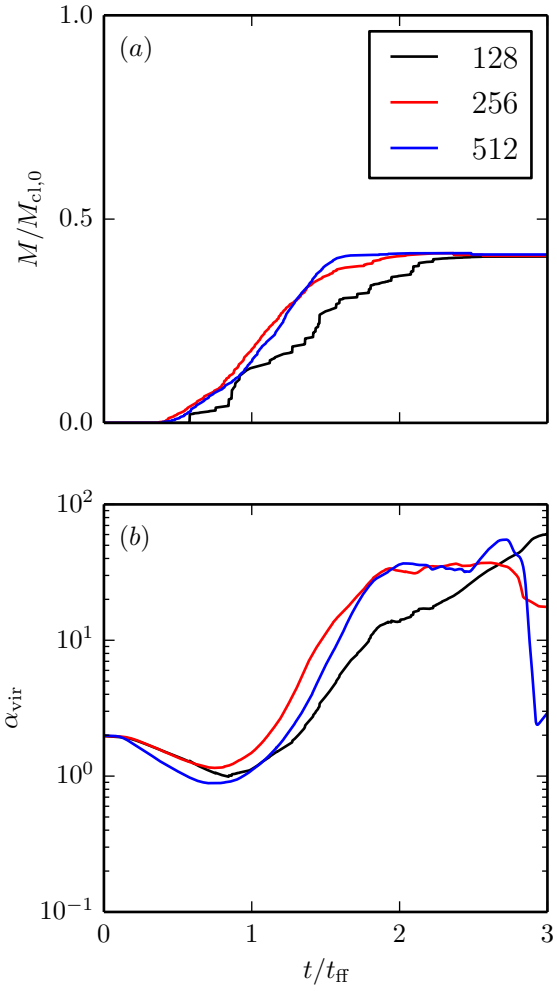

Fig. 10.— Convergence study for the fiducial cloud model with varying resolution N (shown in the key). We show (a) the stellar mass divided by initial cloud mass, and (b) the virial parameter of the gas.

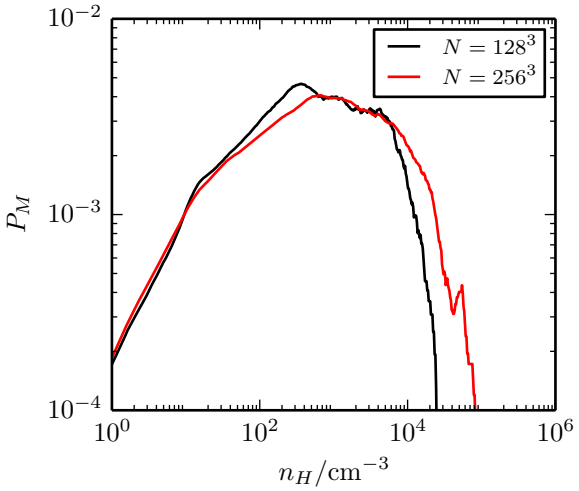

Fig. 11.— **The gas density distribution in our fiducial model at $t_{50} = 1.06\ t_{\mathrm{ff},0}$. We show only the distribution in mass.**

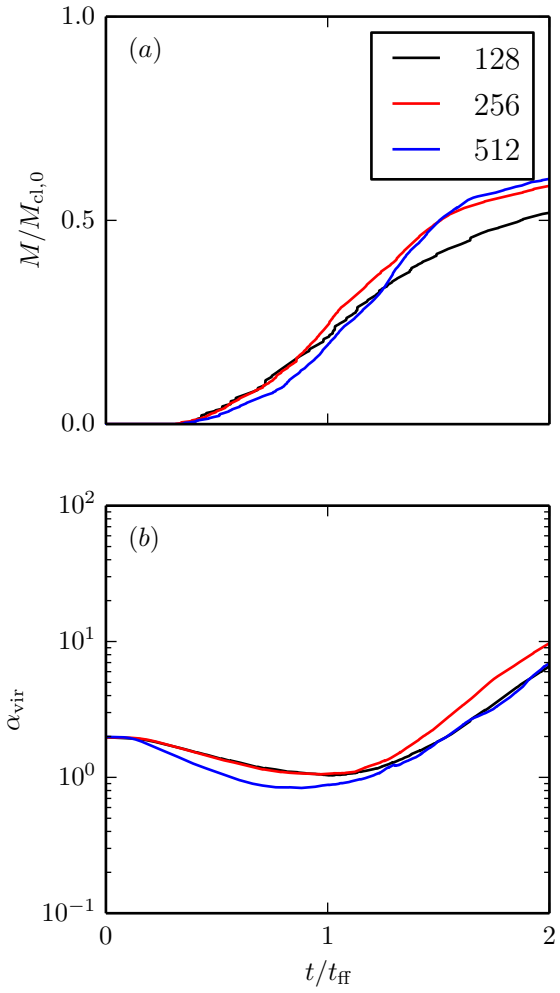

Fig. 12.— Same as Figure 10, but for a higher mass, higher surface density model with $M_{\rm cl,0} = 2 \times 10^5\ M_\odot$ and $r_0 = 15$ pc, corresponding to $\Sigma_{\rm cl,0} = 283\ {\rm M}_\odot\ {\rm pc}^{-2}$.

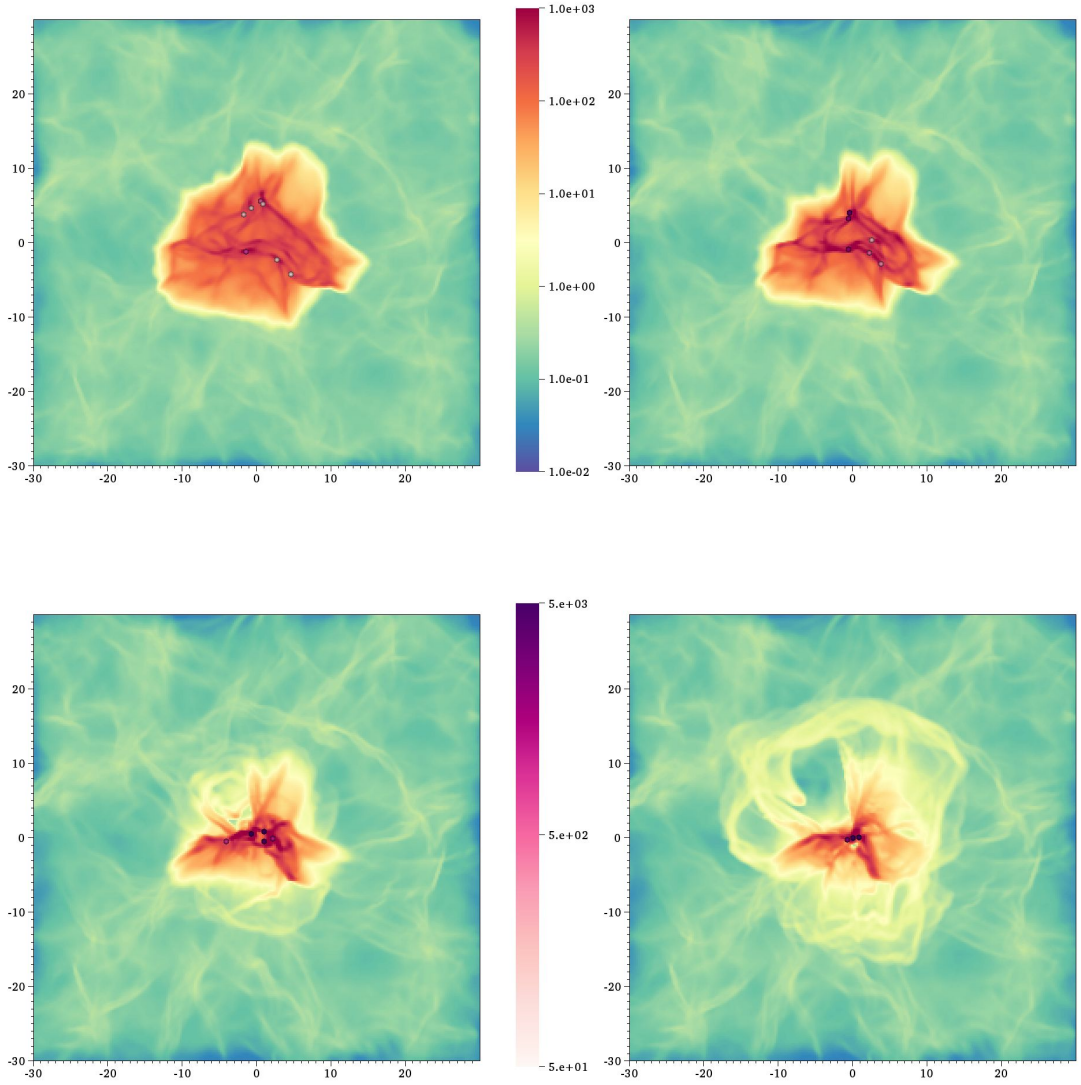

Fig. 13.— Snapshots of the surface density for the fiducial model with reduced turbulence $\alpha_{\rm vir,0} = 0.1$. Surface densities are projected in the x-y plane, and snapshots are shown for $t/t_{\rm ff,0} = 0.72, 0.83, 1.02,$ and 1.13, corresponding to t_2, t_{10}, t_{50} and t_{90}. As for Figure 3, we show also all star particles projected onto the x-y plane. The color scale for the gas column density (top) is in units of $M_\odot$ pc^{-2} and the color scale for the particle mass (bottom) is in units of $M_\odot$.

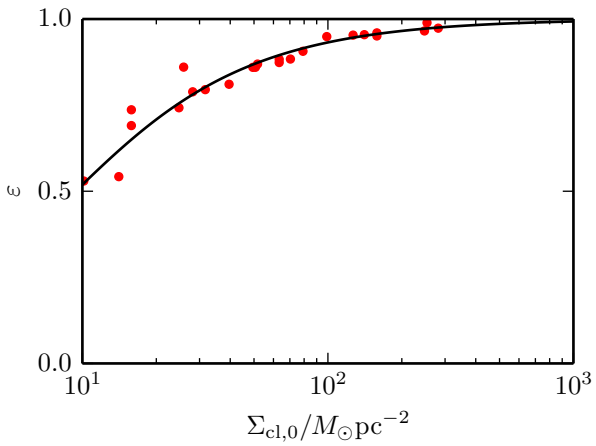

Fig. 14.— Final star formation efficiency ε as a function of surface density (in units $M_\odot$ pc^{-2}) for the Σ-series simulations with reduced turbulence $\alpha_{\rm vir,0} = 0.1$. We show both simulation outputs (red circles) as well as the best-fit to Equation (12) assuming a uniform density shell (black line).

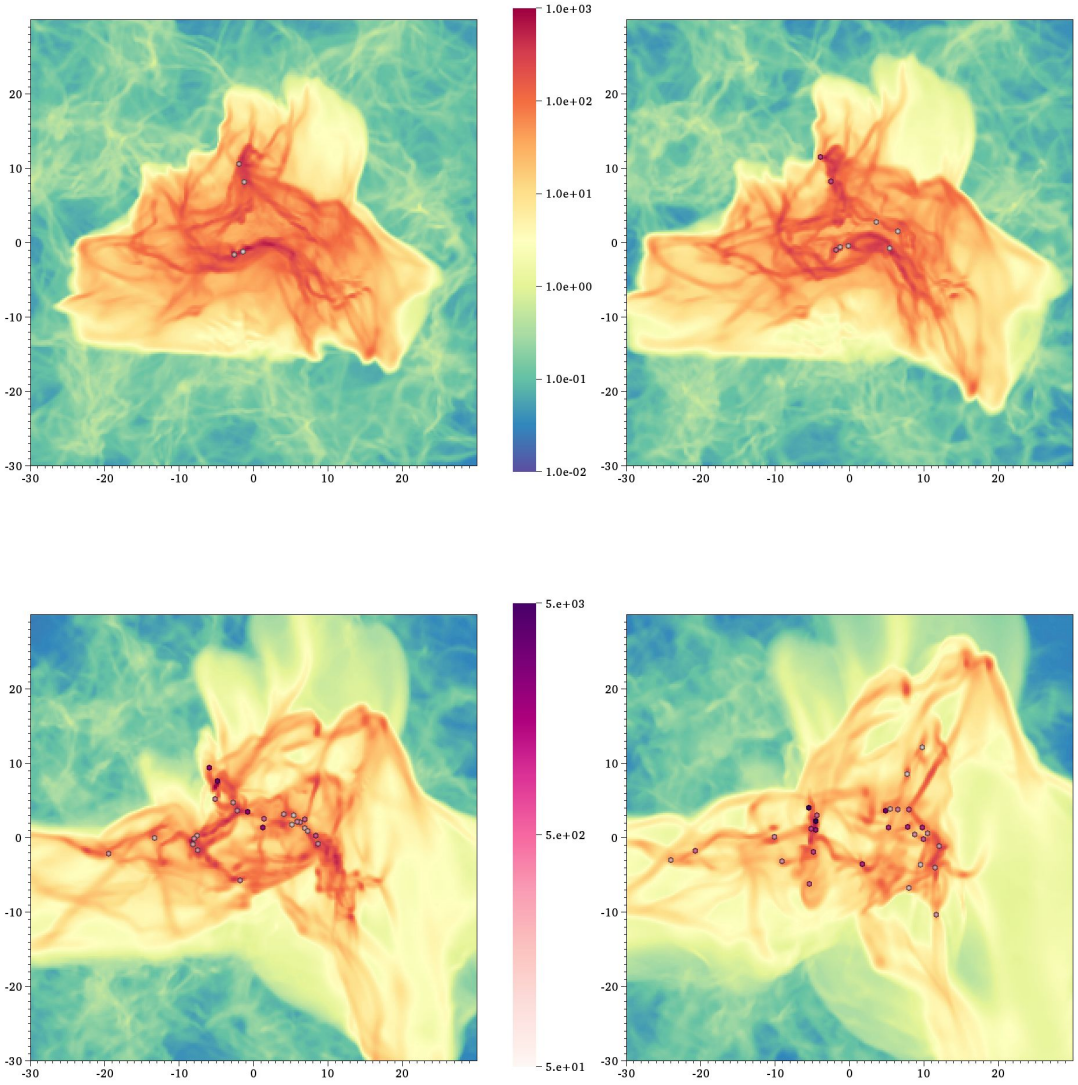

Fig. 15.— Snapshots of the surface density for our fiducial model with no radiative feedback. Snapshots are shown for $t/t_{\rm ff,0} = 0.43, 0.59, 1.06$ and 1.57, i.e., t_2, t_{10}, t_{50} and t_{90} in the fiducial model *with feedback*. We also show all star particles projected onto the x-y plane. The color scale for the gas column density (top) is in units of $M_\odot$ pc^{-2}, and the color scale for the particle mass (bottom) is in units of $M_\odot$.

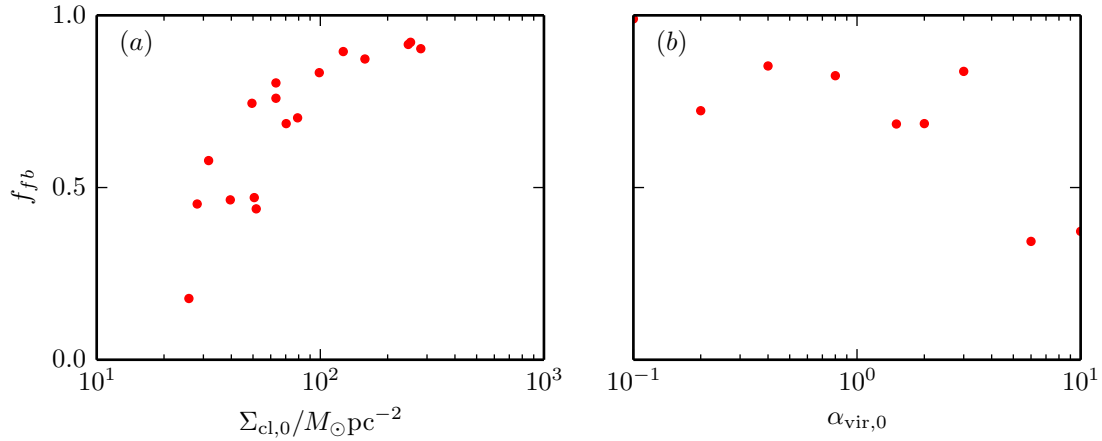

Fig. 16.— Ratio $f_{\rm fb}$ of the stellar mass at time $t_{\rm fb}$ to the final stellar mass for the (a) Σ- series, and (b) α-series simulations.

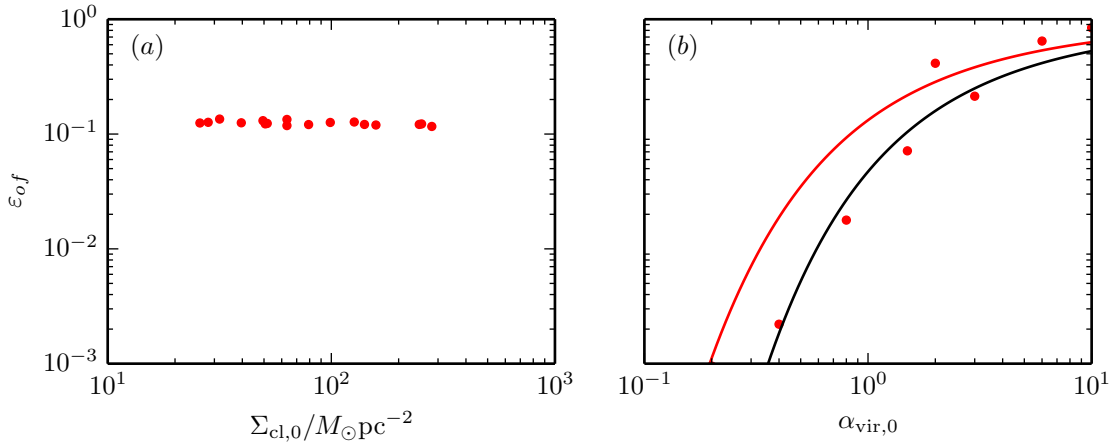

Fig. 17.— Outflow efficiency $\varepsilon_{\rm of}$ for the no-feedback versions (i.e., with radiation turned off) of the (a) Σ-series and (b) α-series simulations. The outflow mass is calculated as the total mass flow out of the box over the 4 free-fall times during which our simulations are run. See text for explanation of black and red curves.

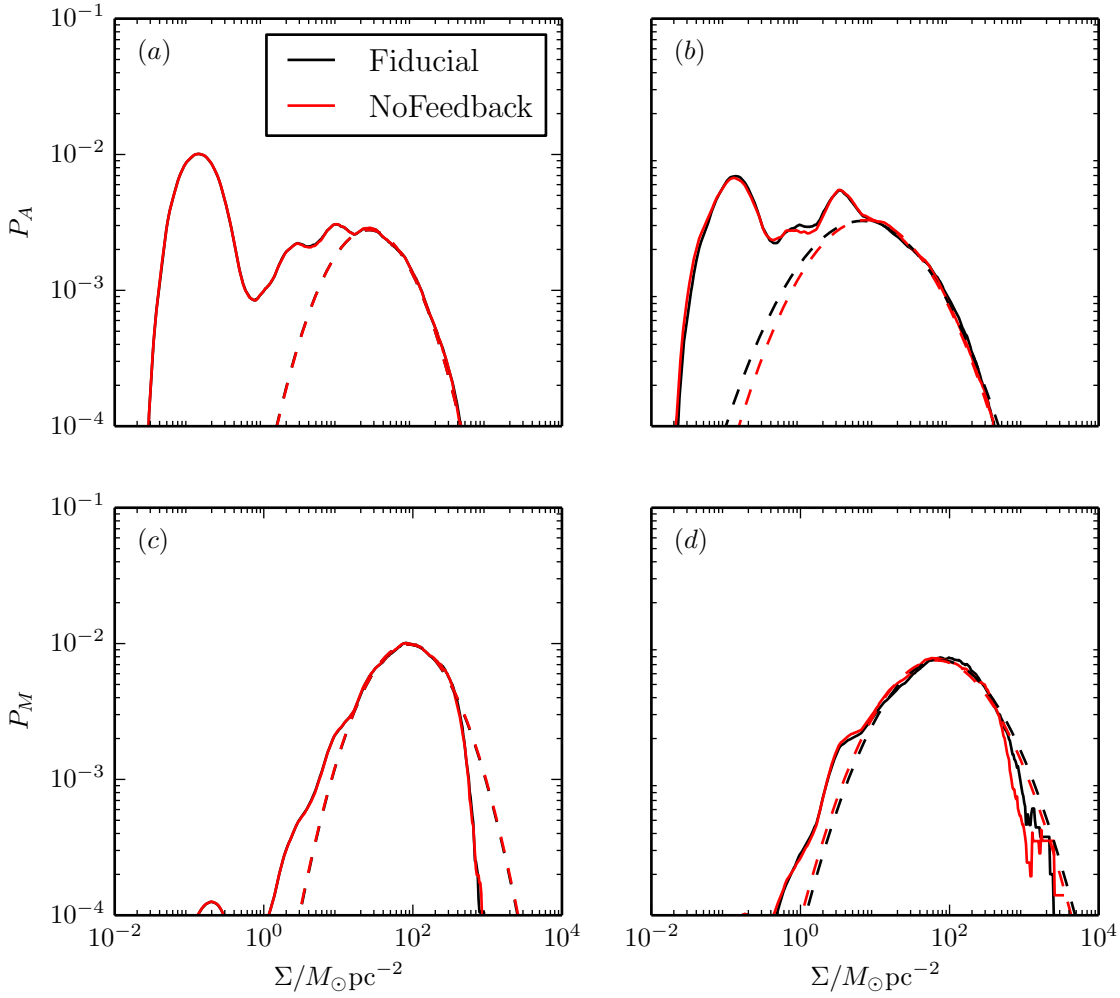

Fig. 18.— Surface density distributions in (top row) area and (bottom row) mass. Times in (a) and (c) are at $t_{10} = 0.59 t_{\mathrm{ff},0}$, and in (b) and (d) are at $t_{50} = 1.06 t_{\mathrm{ff},0}$. We show results for both the fiducial and no-feedback models. In each case, we show both the simulated surface density distributions (solid lines) as well as the best-fit lognormal curves (dashed lines).

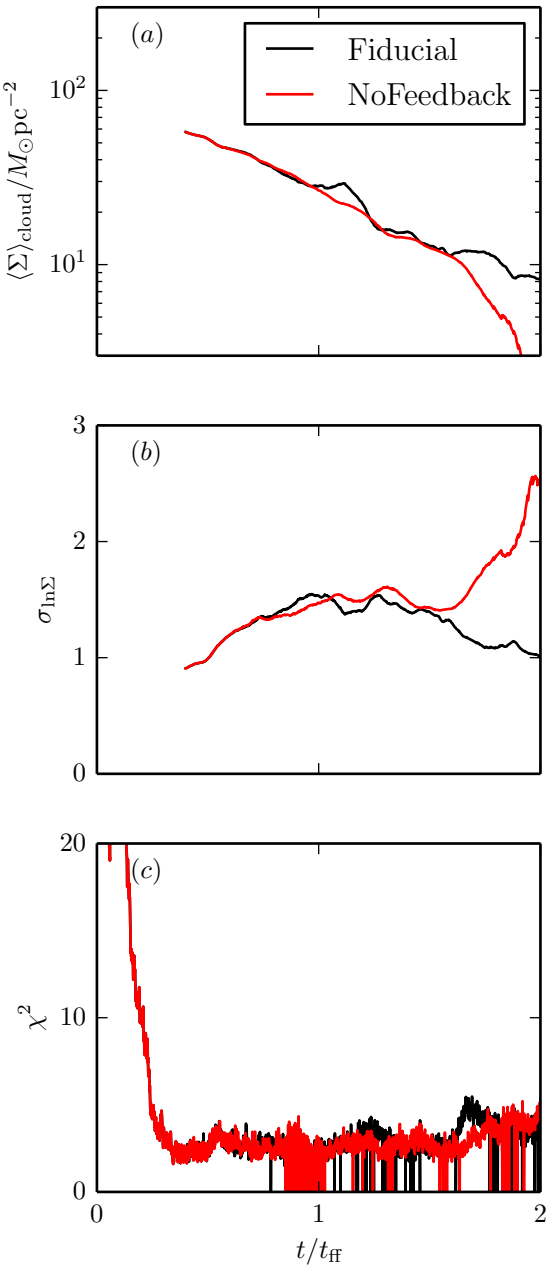

Fig. 19.— Best fit values as a function of time of lognormal fits to our fiducial (black) and no-feedback (red) models. We show (a) the fitted mean surface density $\langle\Sigma\rangle_{\rm cloud}$, (b) the standard deviation to the mass distribution, and (c) the reduced χ^2 of the best fit.

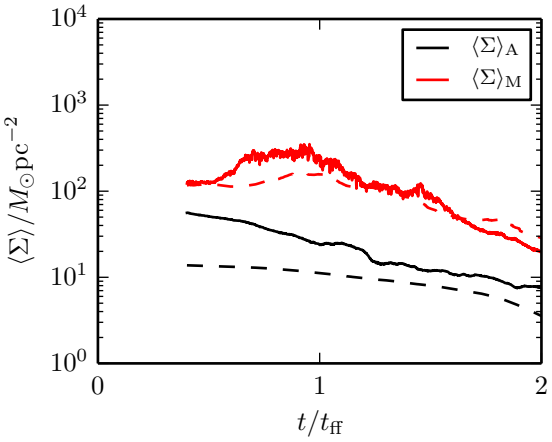

Fig. 20.— Mean surface density as a function of time for our fiducial simulation. We show both the area-weighted mean $\langle\Sigma\rangle_{\mathrm{A}}$ (black) as well as the mass-weighted mean $\langle\Sigma\rangle_{\mathrm{M}}$ (red). For comparison, we show both the values calculated directly by averaging over the whole simulation box (dashed) as well as the values for the cloud alone found by fitting a lognormal distribution to the surface density (solid).

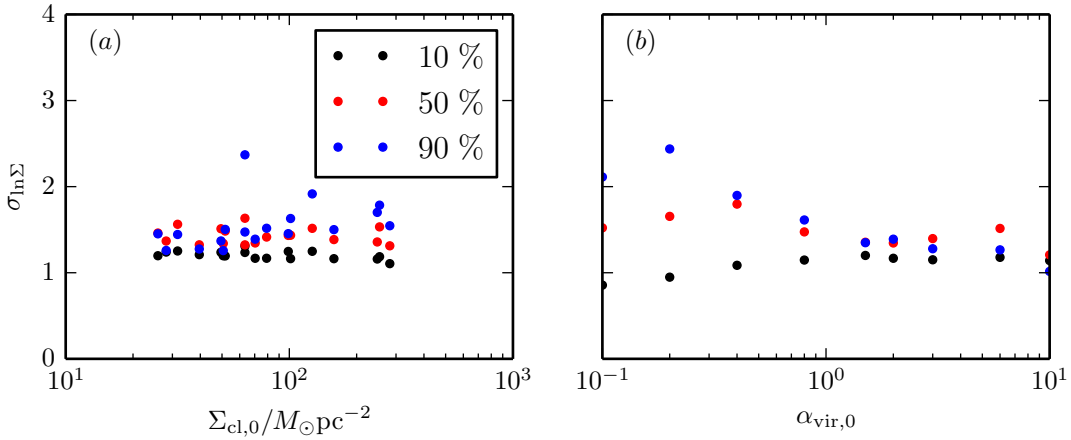

Fig. 21.— Best fit lognormal standard deviation of $\ln\Sigma$ for the (a) Σ-series models and (b) α-series models. We show the best fits at three different times: t_{10}, t_{50} and t_{90}.

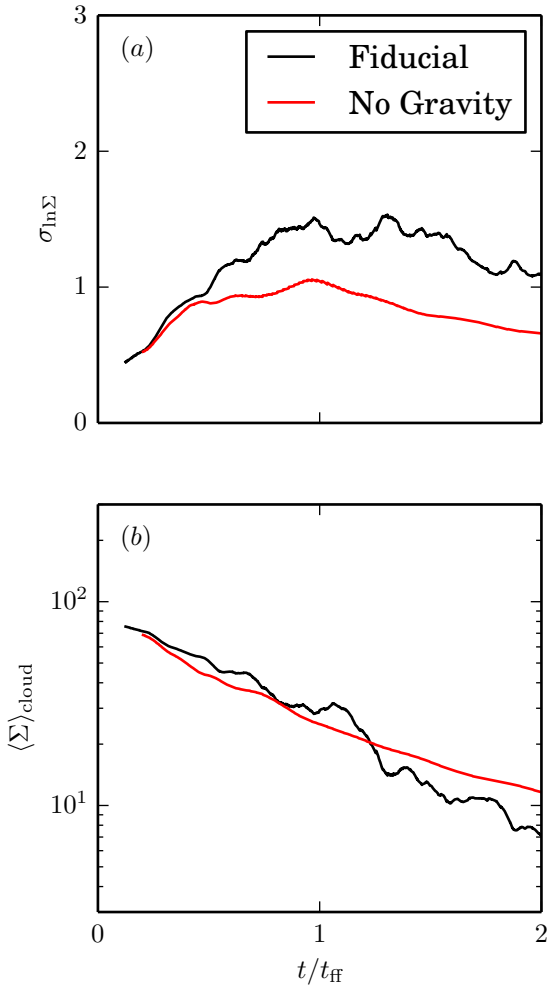

Fig. 22.— Time evolution of the best fit lognormal mean (bottom) and standard deviation (top) to the surface density distribution in our fiducial (black) and no-gravity (red) models.

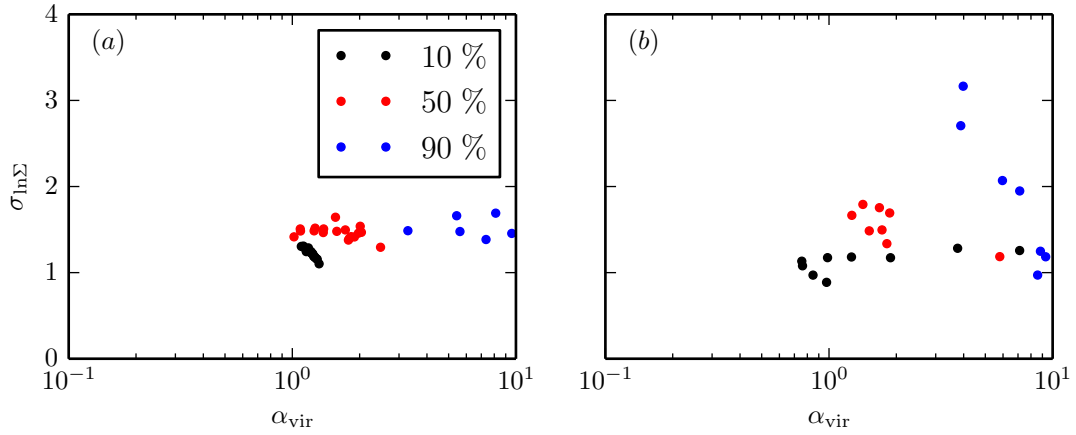

Fig. 23.— Best fit lognormal standard deviation of $\ln\Sigma$ for (a) Σ-series models and (b) α-series models, this time plotted against the instantaneous gas virial parameter in each simulation.

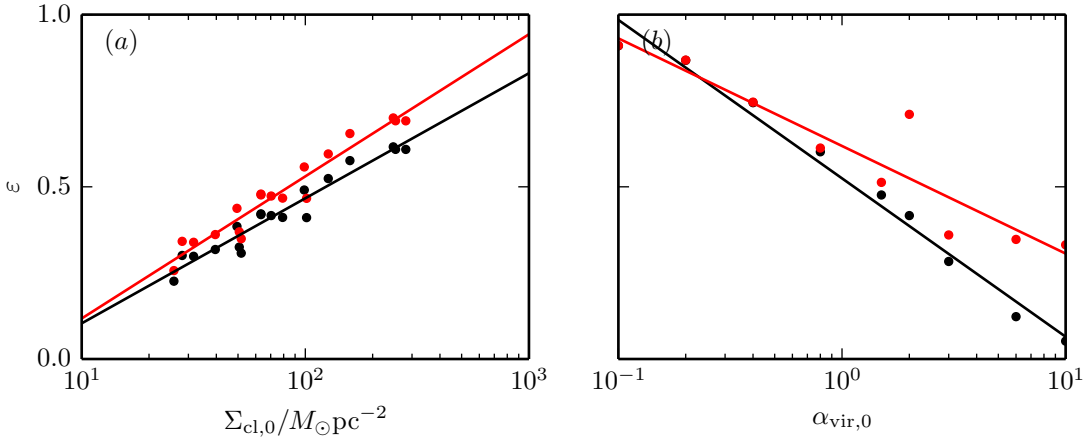

Fig. 24.— Final star formation efficiency ε for (a) Σ-series simulations, and (b) α-series simulations. We show both star formation efficiencies normalized to the initial cloud mass (black circles) and normalized to the cloud mass accounting for initial turbulence-driven outflows (red circles). In all cases we show best-fit logarithmic relations as solid lines.

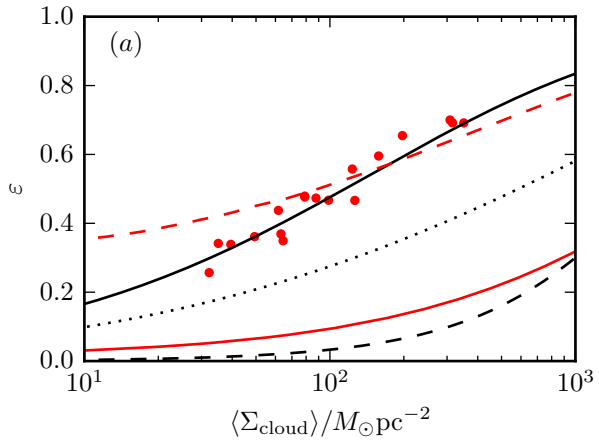

Fig. 25.— Final star formation efficiency ε as a function of surface density for Σ-series simulations. Points show star formation efficiencies ($\varepsilon_{\rm adj}$) normalized to the cloud mass accounting for initial turbulence-driven outflows (red circles). The black solid line shows the prediction of $\varepsilon_{\rm max}$ and the dotted line shows $\varepsilon_{\rm min}$, from Equation (22) with $x = 0.84$ and $\sigma_{\ln\Sigma} = 1.42$ taken from the circumcluster surface density distribution. For comparison, the simple model of Equation 12 with $x = 1$ is shown (black dashed line). We also show the predictions from the model of Thompson & Krumholz (2016), with their fiducial parameter values (red solid), and with values of $\varepsilon_{\rm ff} = 0.44$ and $\sigma_{\ln\Sigma} = 1.42$ based on the results of our simulations (red dashed).

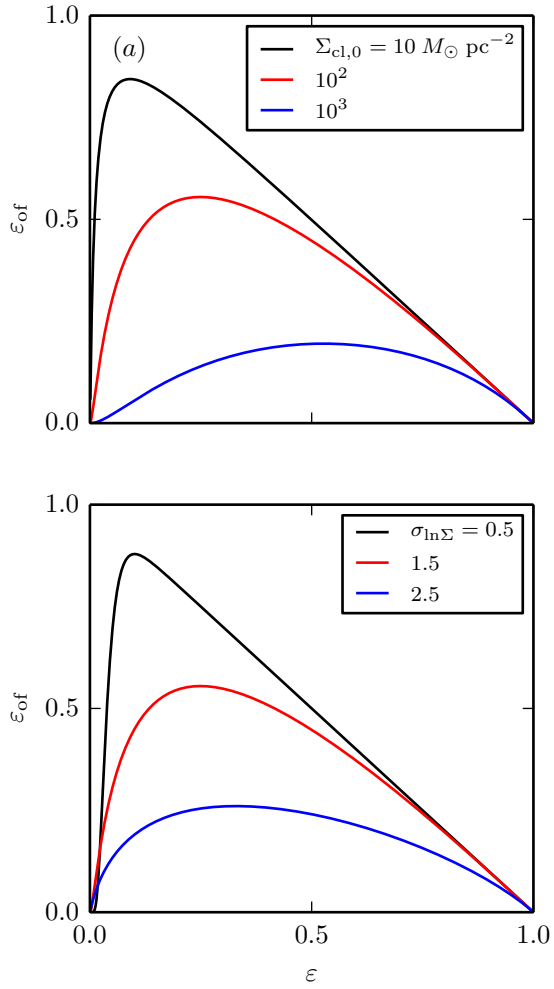

Fig. 26.— Maximum possible stellar efficiency $\varepsilon_{\rm max}$ (Equation 18) as a function of present stellar efficiency ε for (a) clouds of varying initial surface density $\Sigma_{\rm cl,0}$, and (b) varying lognormal surface density distribution width $\sigma_{\ln\Sigma}$. For both cases we use $x = 1$ in Equation (21). In (a), we set $\sigma_{\ln\Sigma} = 1.5$, and the key shows $\Sigma_{\rm cl,0}$ in units of $M_\odot$ pc^{-2}. For (b), we set $\Sigma_{\rm cl,0} = 100\ M_\odot$ pc^{-2} and the key shows values of $\sigma_{\ln\Sigma}$.

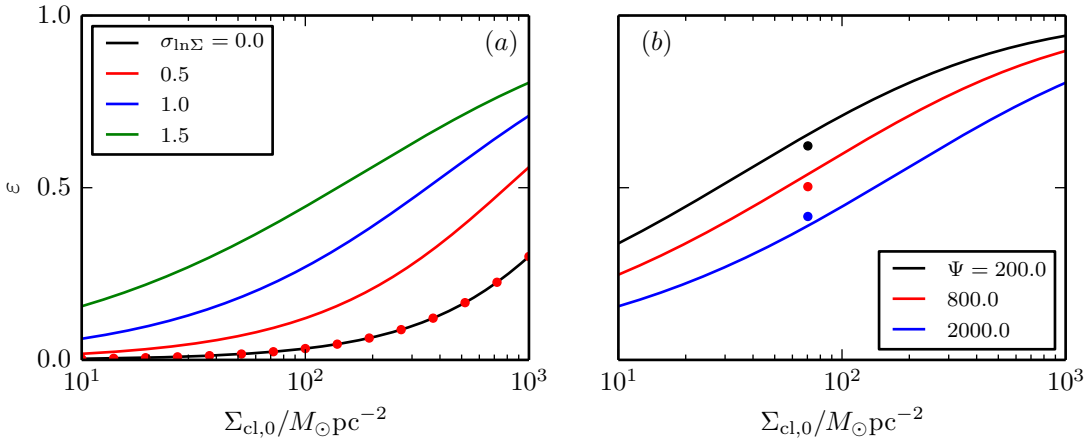

Fig. 27.— Maximum stellar efficiency ε predicted by Equation (22a) as a function of initial surface density for clouds with varying lognormal distribution width $\sigma_{\ln\Sigma}$ (left) and varying Ψ (right). In all cases, we use $x = 1$ and the keys shows appropriate values. For comparison, on the left, we also show values for the simple model of Equation (12) (red circles). As expected, Equation (22a) converges to Equation (12) for small $\sigma_{\ln\Sigma}$, since this is the case of a uniform shell. Meanwhile, for varying Ψ and fixed width $\sigma_{\ln\Sigma} = 1.5$, we also show values of the final efficiency taken from simulations with varying Ψ (circles).

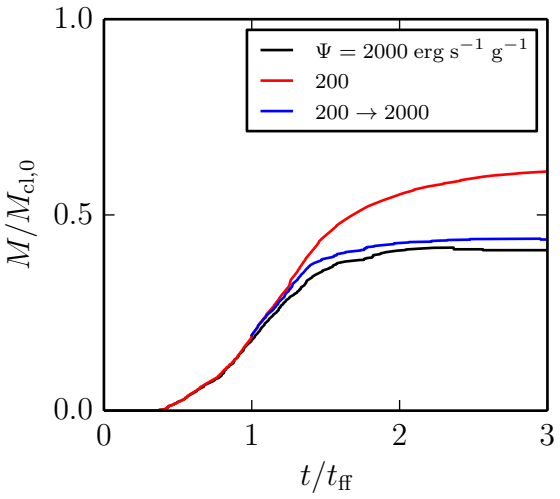

Fig. 28.— Evolution with time of the star formation efficiency for varying values of the luminosity per unit mass Ψ (shown in the legend). We show the fiducial model (black), a low luminosity model (red), and a mixed model for which $\Psi = 200$ erg s^{-1} g^{-1} until a freefall time (at which point $M_* = 8.5 \times 10^3\ M_\odot$), which is then set to the fiducial value $\Psi = 2000$ erg s^{-1} g^{-1} beyond that point.

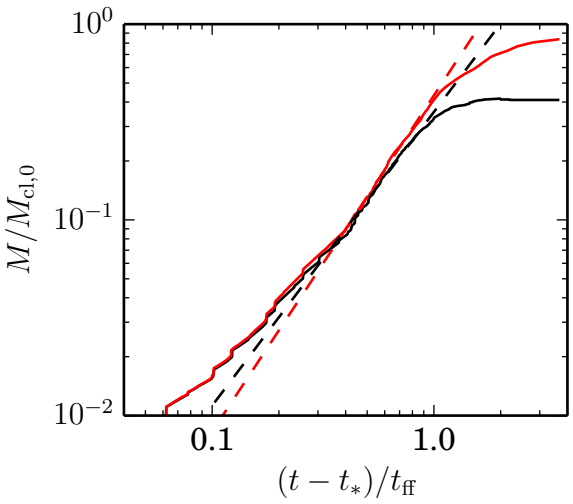

Fig. 29.— Stellar mass as a function of time after the first star was formed for both our fiducial (black) and no-feedback (red) models. For comparison we also show the fits obtained using a single power law in each case (dashed lines).

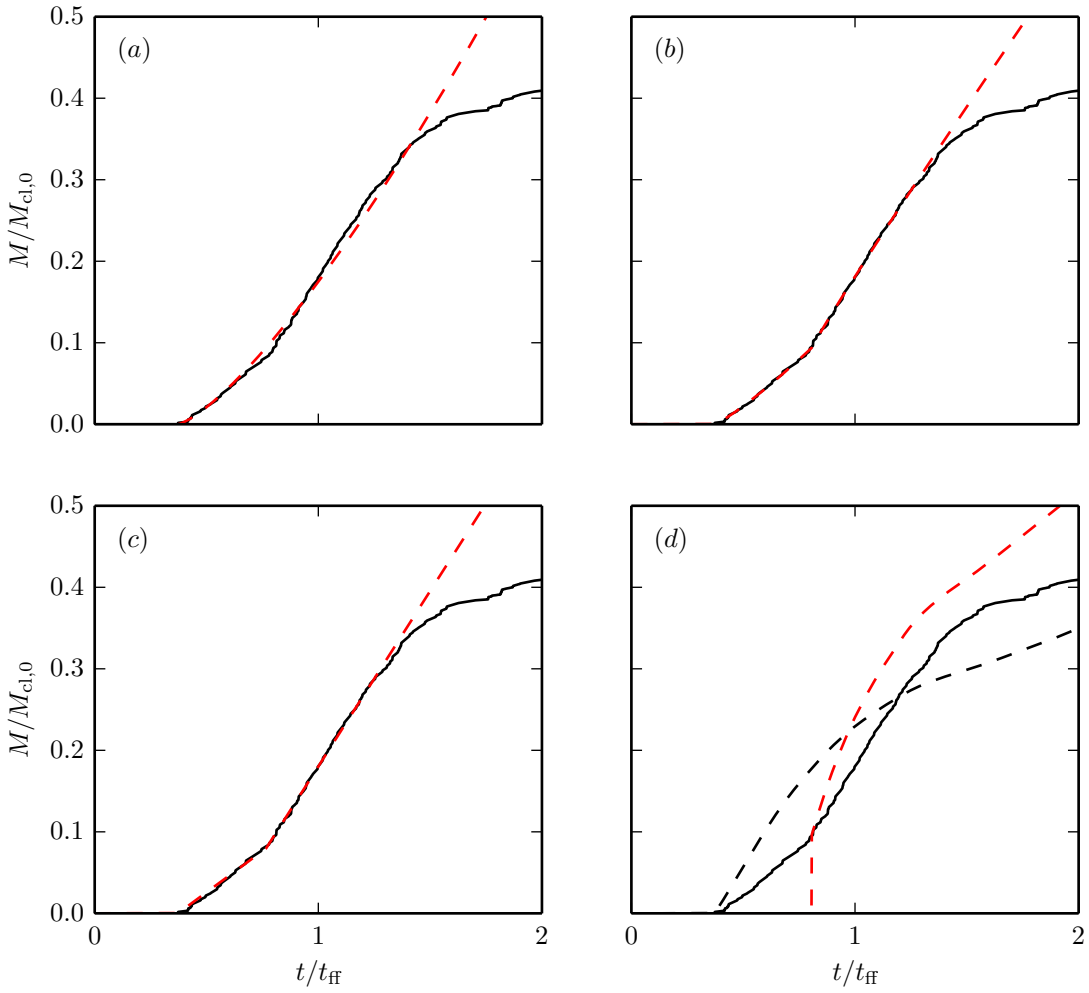

Fig. 30.— Stellar mass as a function of time for our fiducial model in comparison to several fits. In all cases, we show the simulated stellar mass as a solid line. Panel (a) compares to a single power law, panel (b) to a broken power law, and panel (c) a piecewise linear model. In panel (d), we show a comparison to Equation 24 with constant best-fit $\varepsilon_{\rm ff}$ starting either at t_* (black dashed), or starting at $t_{\rm break}$ (red dashed). For (d) we compute ρ and $t_{\rm ff}$ allowing for evolving gas mass and evolving cloud size based on a log-normal fit.

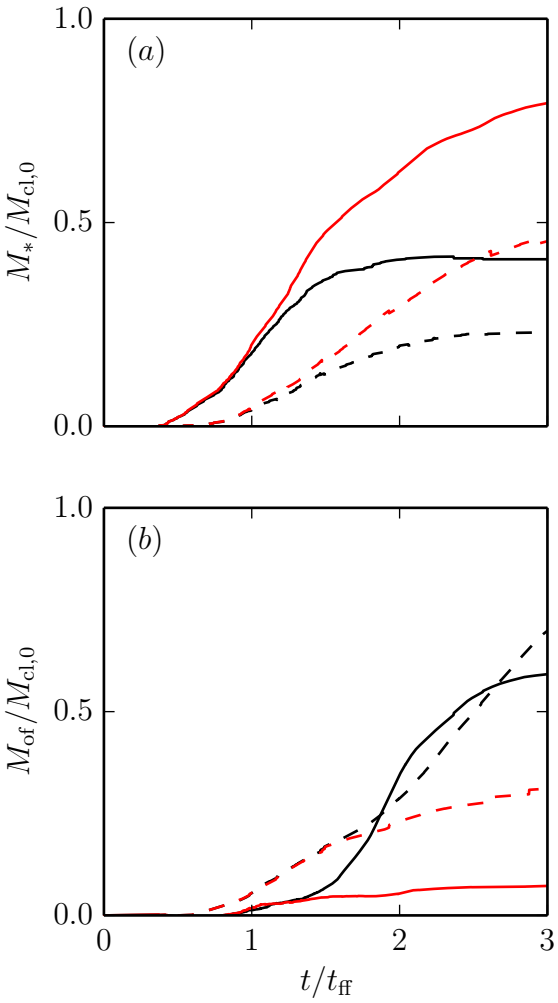

Fig. 31.— Evolution of the star formation efficiency (top) and outflowing mass (bottom) with time for varying initial conditions. We show results for both our fiducial model (solid), as well as a model initialized from conditions in which the density relaxes in response to turbulence before gravity is turned on (dashed). In both cases, we show both models with radiative feedback (black) and without (red).

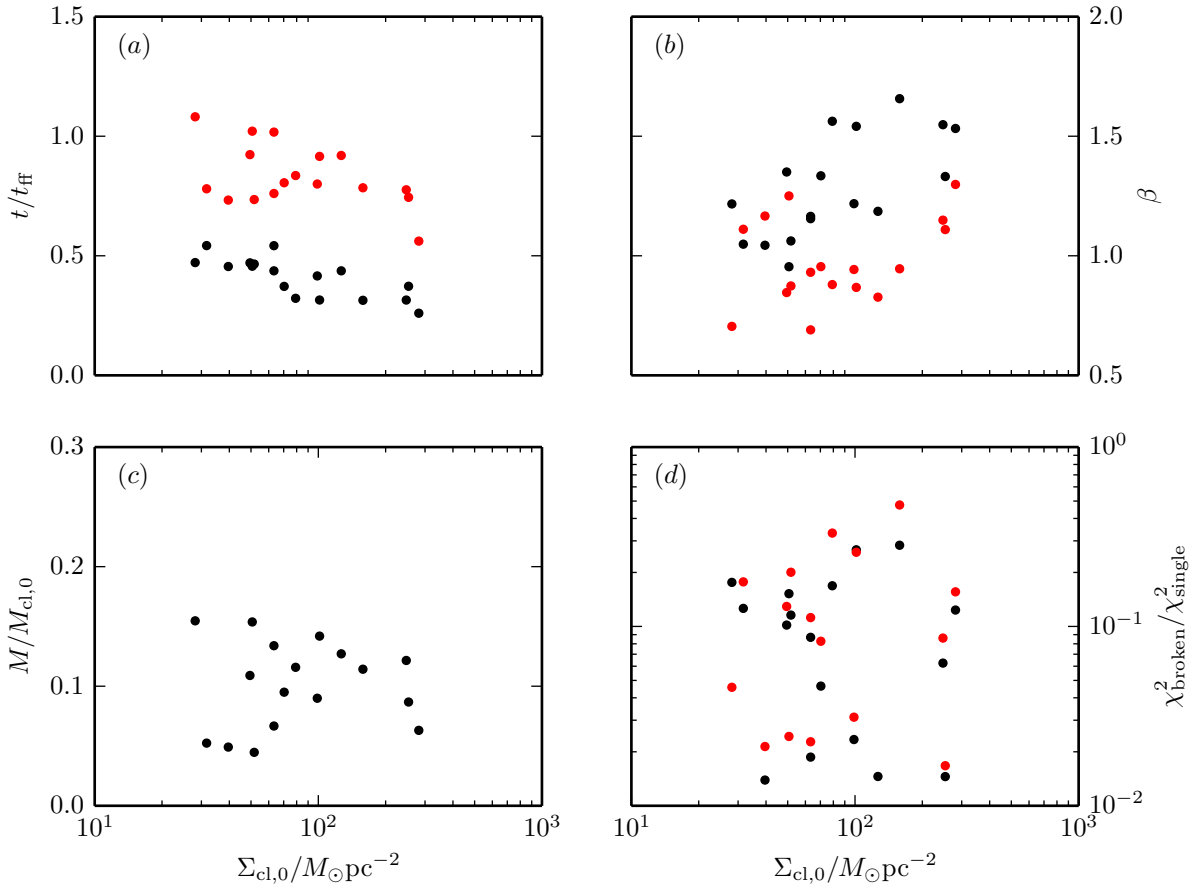

Fig. 32.— Characteristics of our best fit single power law and broken power law fits for the Σ-series. Panel (a) shows the break time $t_{\rm break}$ for the broken power law (red) and t_* (black), while Panel (c) shows the corresponding break masses. Panel (b) shows the post-break exponent in the broken power law (red) or single exponent in the single power law (black). Finally, in Panel (d), we show the relative values of χ^2 for the broken and single power law models, both over the whole fitting range (black) and just after $t_{\rm break}$ (red).

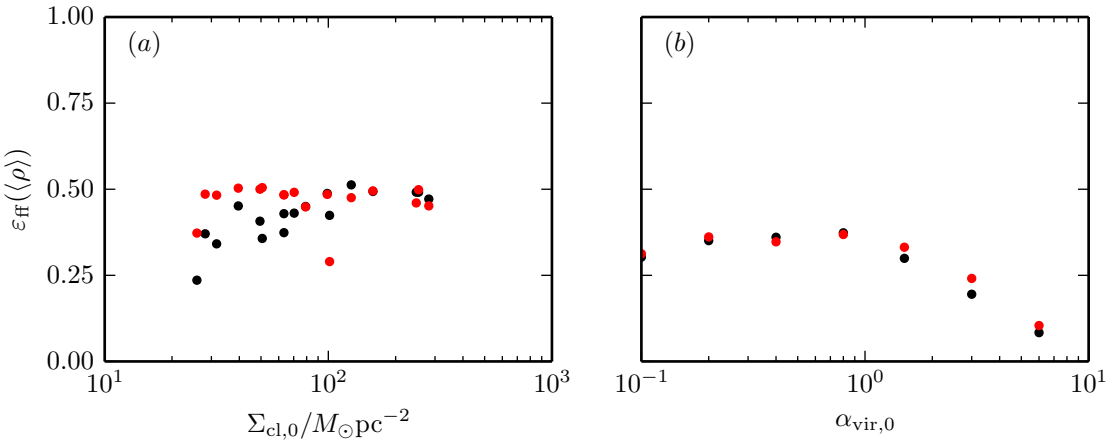

Fig. 33.— Star formation rate coefficient $\varepsilon_{\rm ff,\bar{\rho}}$ (defined in Equation 25) for the (a) Σ-series simulations and (b) α-series simulations. We show results from simulation with radiation feedback (black) and without (red).

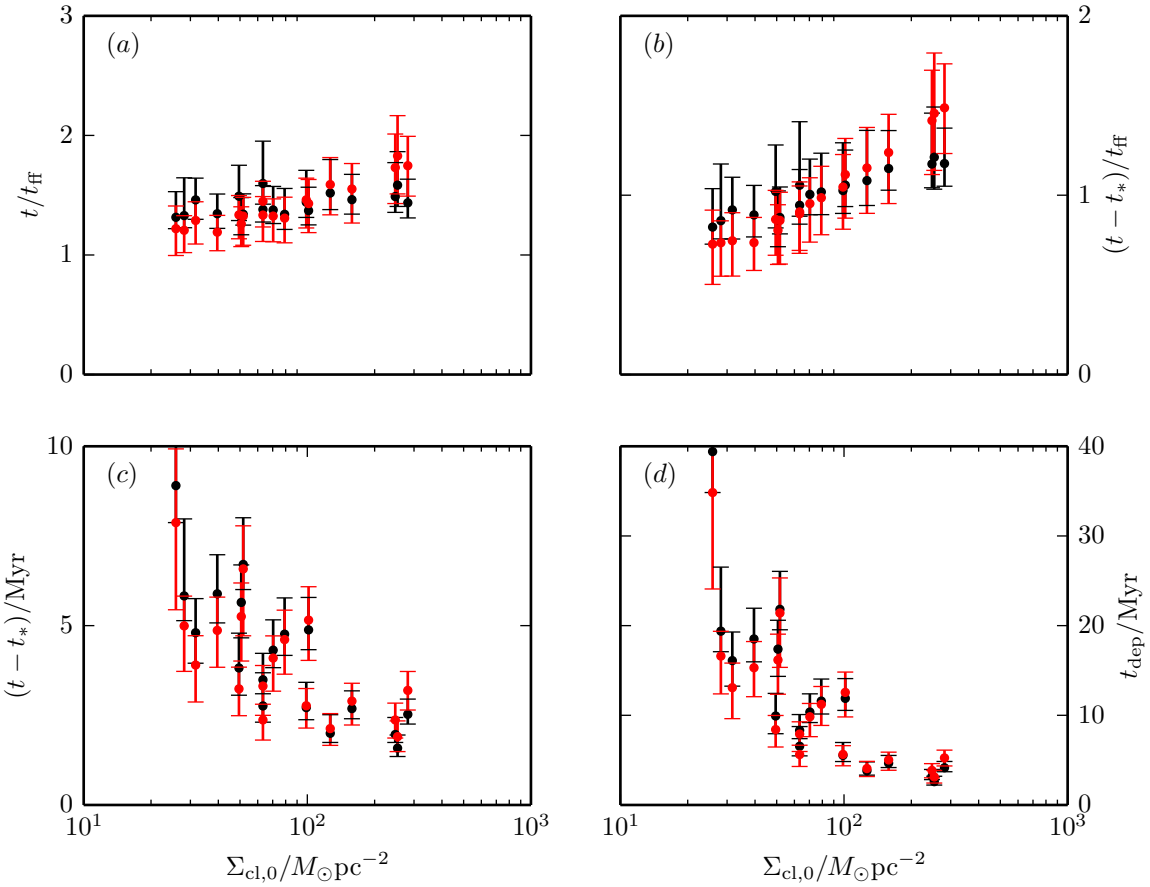

Fig. 34.— Cloud lifetimes as a function of surface density for our Σ-series of models. We show lifetimes calculated using the time t_{80} when $80^{+10}_{-10}\%$ of stars are formed (black) and the time $t_{\rm unb}$ when the virial parameter reaches 5^{+5}_{-3} (red). Error bars denote the limits on these respective values so that the uppermost limit shows t_{90} and the time when $\alpha_{\rm vir} = 10$. In both cases, we show (a) the simulation time when this occurs in units of $t_{\rm ff,0}$, (b) the time after the first star is formed $(t - t_*)$ in units of $t_{\rm ff,0}$, (c) $t - t_*$ in Myr, and (d) the depletion time $t_{\rm dep} \equiv (t - t_*)/\varepsilon_{\rm final}$.

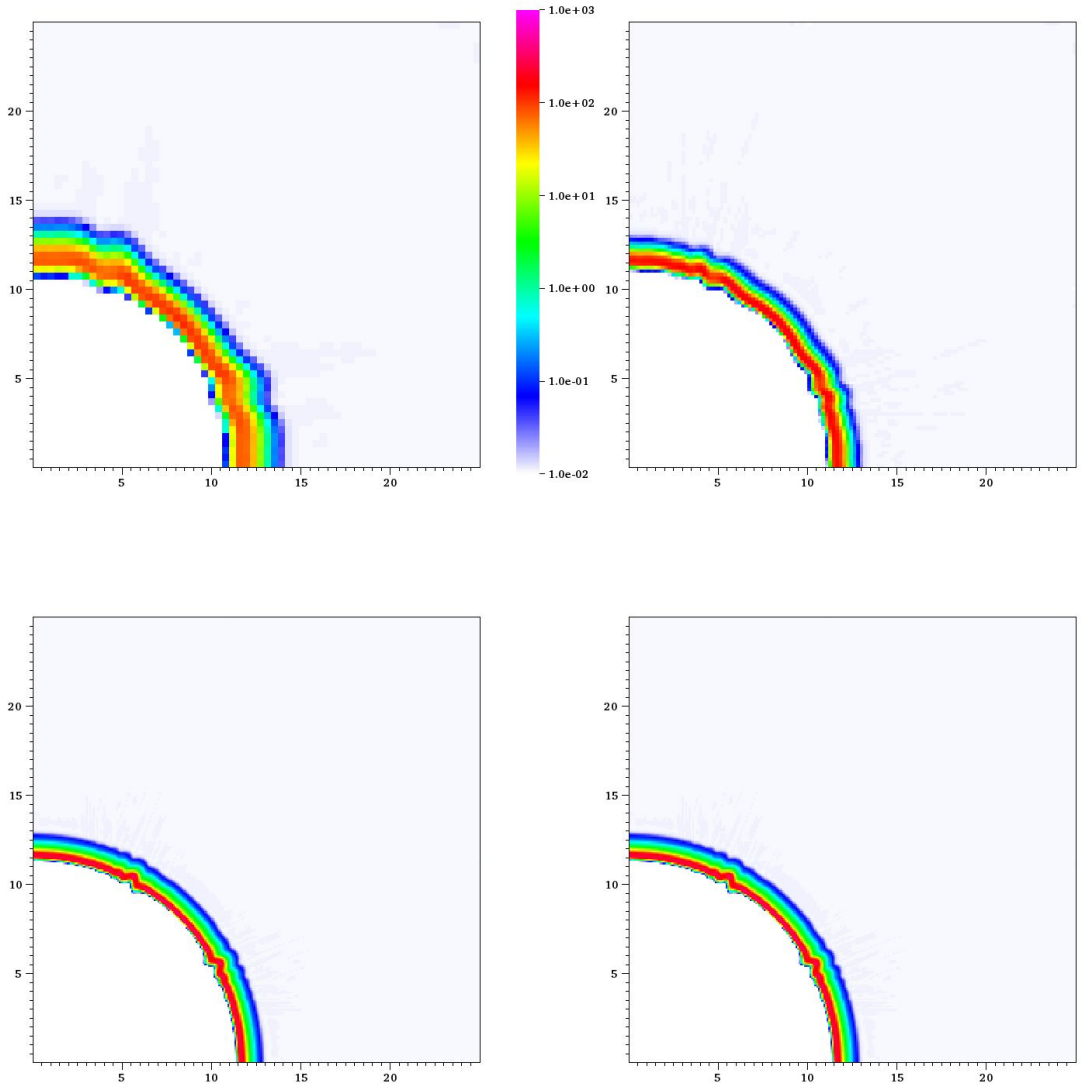

Fig. 35.— Snapshots of the density at $t = 1.2t_0$, for the fiducial spherical shell problem, with cloud mass $M_{\rm cl,0} = 10^4\ M_\odot$. We show (reading from left to right and top to bottom) simulations with $N = 64, 128, 256$ and 512 respectively. In each case, the snapshots show 2D slices through the x-y plane of the shells. The color scale for the gas density n_H (top) is in units of cm^{-3}.

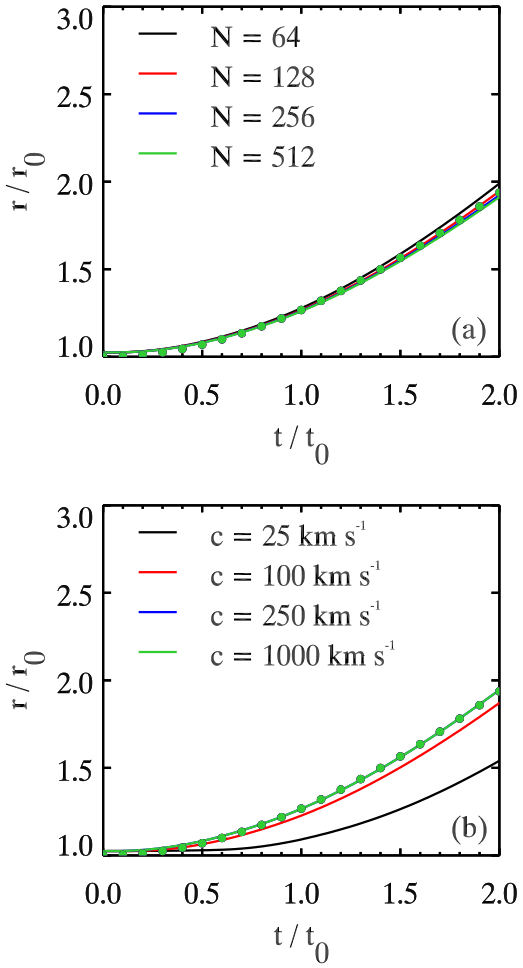

Fig. 36.— Mass-weighted shell radius as a function of time for (a) varying resolution N and (b) reduced speed of light $\hat{c}$, in the spherical shell problem. In each case, we use $M_{\rm cl,0} = 10^4\ M_\odot$, $r_0 = 10$ pc, $\Psi = 2000$ erg s^{-1} g^{-1}, $\kappa = 1000$ cm^2 g^{-1}, and $\varepsilon = 0.5$. The key shows (a) the resolution in cells and (b) $\hat{c}$ in kms^{-1}. The dotted curve in each panel shows the analytic solution for comparison.

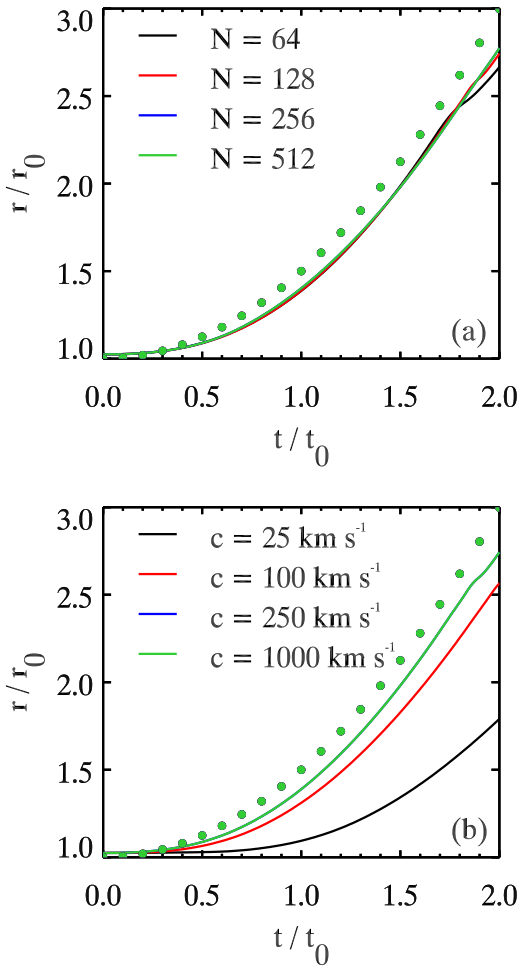

Fig. 37.— Same as Figure 36, except for a cloud of mass $M_{\rm cl,0} = 3 \times 10^5\ M_\odot$.

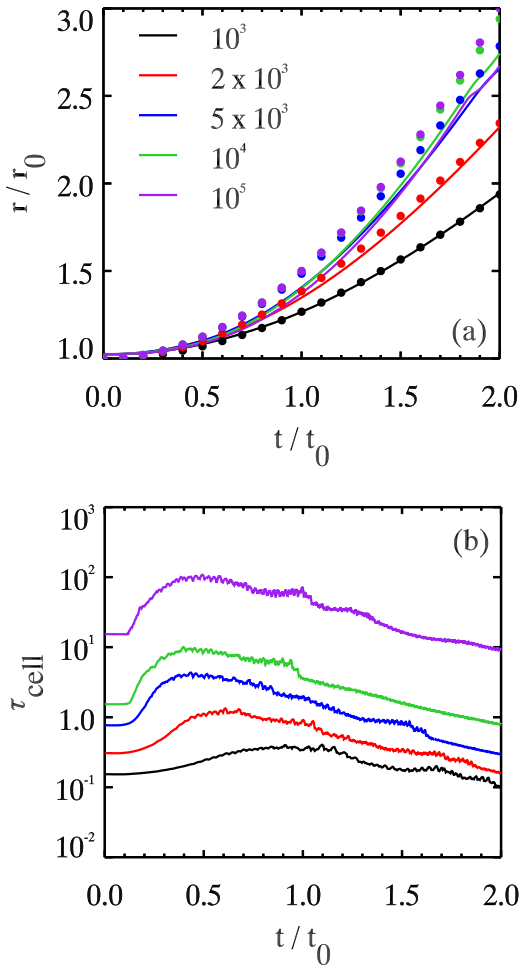

Fig. 38.— (a) Mass-weighted shell radius, and (b) maximum cell optical depth, for the spherical shell test at with varying opacity, κ. The key shows the opacity in g cm^{-2}. Dotted curves in the upper panel show the analytic expansion solution.

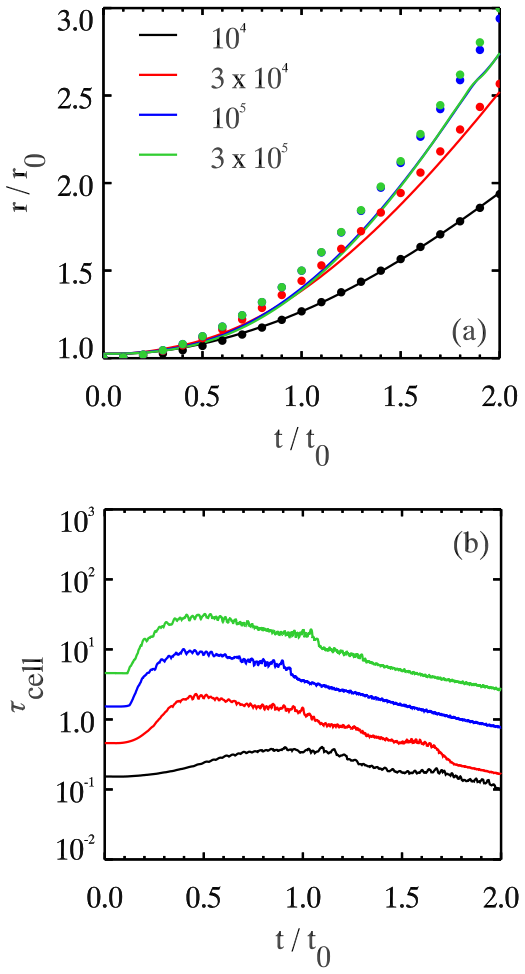

Fig. 39.— Same as Figure 38, but for varying cloud mass (in units $M_\odot$, as shown in the key).